Université de Lille

Ecole doctorale des Sciences de l'ingénierie et des systèmes

Thèse

Pour obtenir le grade de Docteur de l'Université de Lille

Spécialité : Génie Electrique

Présenté et soutenue publiquement par

GODART Gabriel

Soutenance le 16 juin 2026

Inversion-Based Control of Power System for Proton Synchrotron Accelerator

Commande par inversion du système de puissance pour l'accélérateur de particule Proton Synchrotron

Membres du Jury:

Pr. Philippe BARRADE	Haute Ecole d'Ingénierie – Sion HES-SO Valais-Wallis, Suisse	Rapporteur
Pr. Olivier BETHOUX	Sorbonne Université, France	Rapporteur
Ing. Fulvio BOATTINI	CERN, Suisse	Co-encadrant de la thèse
Pr. Loïc BOULON	Université du Québec à Trois-Rivières, Canada	Examinateur
Pr. Alain BOUSCAYROL	Université de Lille, France	Directeur de la thèse
Dr. Philippe DELARUE	Université de Lille, France	Co-encadrant de la thèse
Pr. Betty LEMAIRE-SEMAIL	Université de Lille, France	Examinatrice
Dr. Sandrine MOREAU	Université de Poitiers, France	Examinatrice
Pr. Paul-Etienne VIDAL	Université de Tarbes, France	Président du Jury

Thèse en collaboration avec le CERN (Organisation Européenne Pour la Recherche Nucléaire)

Acknowledgement

I would like to express my sincere gratitude to my PhD director, Prof. Alain Bouscayrol and my PhD co-supervisor Fulvio Boattini, for their guidance, support, and expertise throughout this research. Their supervision, particularly in EMR, RST control and C++ programming, was essential to the completion of this work.

I am also grateful to my co-supervisor, Philippe Delarue for his valuable input and availability. I especially appreciate his help with equations and system modelling, which significantly strengthened this thesis and helped me get unstuck at key moments.

I would like to thank my colleagues Manuel, Aramis and Marco for the collaborative environment they helped create. Their support through programming, hardware work and simulations made the research process both productive and enjoyable.

I also acknowledge the L2EP laboratory and CERN for providing the resources and facilities necessary to carry out this work.

I am also grateful to David, Alessio and Nagore for the many bikes rides we shared, which helped me stay focused and motivated throughout my doctoral studies.

Abstract

Particle accelerators rely on high-performance power converters to generate precise magnetic fields for beam control. In synchrotron machines such as the Proton Synchrotron at CERN. These converters must deliver high-dynamic magnetic field profiles with extreme accuracy while managing large amounts of energy. The POwer converter for Proton Synchrotron (POPS) is a pulsed power supply system designed to meet these requirements by combining capacitive energy storage with multi-stage power conversion. Its control is particularly challenging due to strong coupling between subsystems, stringent precision constraints, and the need to ensure a stable operation under varying conditions.

This PhD investigates the application of inversion-based control derived from Energetic Macroscopic Representation to the POPS system. The objective is to develop a flexible control structure capable of ensuring accurate magnetic field tracking while managing internal energy flows and maintaining system balance. This flexibility is required for future extensions of POPS.

A detailed model of the POPS architecture is first developed and organized using the EMR formalism, starting from a unitary converter and extending to the complete multi-converter system. This model organization highlights energy exchanges and system causality, providing a clear framework for control design. Based on this representation, an inversion-based control structure is systematically derived.

The proposed control strategy is validated through simulation, demonstrating its ability to achieve high tracking accuracy, regulate capacitor voltages, and control internal currents. An experimental validation is carried out on a reduced-scale platform, confirming the feasibility and robustness of the approach in real-time.

The results show that inversion-based control offers a transparent and flexible alternative to the initial RST control, with strong potential for complex power electronic systems. This work contributes to the development of advanced control strategies for accelerator power converters and supports future evolution of the POPS system and next-generation accelerator infrastructures.

Résumé

Les accélérateurs de particules nécessitent des convertisseurs performants pour générer des champs magnétiques précis permettant le contrôle du faisceau de particules. Dans les synchrotrons tels que le Proton Synchrotron au CERN, ces convertisseurs doivent fournir des profils de champs magnétiques dynamiques avec une précision extrême tout en gérant de grandes quantités d'énergie. Le Proton Synchrotron utilise un convertisseur de puissance multi-étage pulsé, nommé POPS, conçu pour répondre à ces exigences. Son contrôle est particulièrement complexe en raison des couplages entre les sous-systèmes, des contraintes de précision strictes et de la nécessité d'assurer une stabilité des variables internes.

Cette thèse concerne l'application d'une commande par inversion, dérivée de la Représentation Énergétique Macroscopique (REM) du POPS. L'objectif est de développer une structure de commande flexible capable d'assurer un suivi précis du champ magnétique tout en gérant les flux d'énergie internes et en maintenant la stabilité du système. Cette flexibilité est indispensable aux extensions futures du POPS.

Un modèle détaillé du POPS est d'abord développé et organisé à l'aide du formalisme REM, en partant d'un convertisseur unitaire et en l'étendant à l'ensemble du système multi-convertisseurs. Cette approche de modélisation met en évidence les échanges d'énergie et la causalité du système, offrant une base solide pour la conception de la commande. À partir de cette représentation, une commande par inversion en est systématiquement déduite.

La stratégie de commande proposée est validée par simulation, démontrant sa capacité à atteindre une grande précision de suivi de référence (de l'ordre de la centaine de ppm, partie par million), à réguler les tensions des condensateurs et à contrôler les courants internes. Une validation expérimentale est réalisée sur une plateforme à échelle réduite, confirmant la faisabilité et la robustesse de l'approche et son implémentation en temps réel.

Les résultats montrent que la commande par inversion constitue une alternative interprétable et flexible comparé à la commande initiale RST, avec un potentiel pour les systèmes d'électronique de puissance complexes. Ce travail contribue au développement de stratégies de commande avancées pour les convertisseurs de puissance des accélérateurs de particules et contribue aux futures évolutions du POPS ainsi que les accélérateurs de nouvelle génération.

Table of contents:

General Introduction 1

I. Context and Objective 4

I.1. Background and motivations 4

I.1.a. Particle accelerators 4

I.1.b. Challenges of control of these power converters 8

I.1.c. Future of CERN 10

I.2. PhD positioning 12

I.2.a. POPS control 12

I.2.b. Inversion-based control and EMR 15

I.2.c. Inversion-based control at CERN 16

I.3. Research framework and objectives 18

I.3.a. Objectives of the PhD 18

I.3.b. Tools and methods 19

I.3.c. Contribution of the PhD 20

II. Inversion-based control of a unitary converter 21

II.1. From unitary converter to the complete system 21

II.2. EMR of the unitary converter 23

II.2.a. Grid and AFE 23

II.2.b. Capacitor storage and capacitor divider 24

II.2.c. NPC converter 26

II.2.d. Interleaved inductances 29

II.2.e. Capacitive filter 32

II.2.f. Electromagnet 34

II.2.g. EMR of unitary converter 34

II.3. Inversion-based control of the unitary converter 35

II.3.a. Control of the electromagnet 36

II.3.b. Control of the capacitive filters 36

II.3.c. Control of the inductive filter and the circulating currents 36
II.3.d. Control of the voltage balance 37
II.3.e. Inversion of the six-legged converter 39
II.3.f. Inversion of the converter 39
II.3.g. Inversion of the storage capacitor 40
II.4. Control performances in simulation 43
II.4.a. Control performances in average value 43
II.4.b. Control performances in discrete value 47
II.4.c. Conclusion of the unitary system results 51
III. Inversion-based control of POPS 52
III.1. EMR of POPS 52
III.1.a. Capacitor storage, floating and capacitor divider 52
III.1.b. NPC converter 56
III.1.c. Interleaved inductances. 56
III.1.d. Capacitive filters 59
III.1.e. A and B series connection 59
III.1.f. Electromagnet 59
III.1.g. EMR of POPS 60
III.2. Inversion-based control of POPS 61
III.2.a. Control of the electromagnets 61
III.2.b. Control of the series connection between the 2 sets 62
III.2.c. Control of the capacitive filters 62
III.2.d. Control of the inductive filters and the circulating currents 62
III.2.e. Control of the converter 62
III.3. Energy management strategy of POPS 64
III.3.a. EMS in nominal mode 64
III.3.b. EMS in fault mode 69
III.4. Control performances in simulation 71
III.4.a. Control performances in average value 71

III.4.b. Control performances in discrete value 76
III.4.c. Conclusion of POPS results 81
IV. Experimental implementation of the inversion-based control 82
IV.1. Experimentation on mini-POPS-B 82
IV.1.a. Description of mini-POPS-B 82
IV.1.b. Initial RST Control 88
IV.1.c. Hybrid control 89
IV.1.d. Results of the inversion-based control 94
IV.2. Experimentation on mini-POPS 98
IV.2.a. Description of mini-POPS 98
IV.2.b. Mini-POPS hybrid control 100
IV.2.c. Inversion-based control results 105
IV.2.d. Conclusion of the experimental results 109
Conclusion 110
Annexes 114
References 135

General Introduction

Modern particle accelerators are among the most demanding electrical systems ever built. Although their scientific objectives are defined by particle physics, their performance ultimately depends on the ability of electrical and control engineers to generate, regulate, and coordinate large amounts of power with extreme precision. In synchrotron accelerators in particular, the quality of the particle beam is directly linked to the accuracy and reproducibility of the magnetic fields that guide and focus the beam. These magnetic fields are produced by large electromagnets supplied by high-power, tightly regulated power converters, making power electronics and control a central pillar of accelerator operations.

At CERN, the world's leading laboratory for particle physics, this challenge is amplified by the scale and complexity of the accelerator. Thousands of power converters operate simultaneously, often following synchronized and repetitive cycles, while interacting with a shared electrical infrastructure. The required current waveforms are highly dynamic and must be tracked with relative accuracy that can reach a few tens of parts per million. Any deviation can result in beam distortion, loss of performance, or even beam aborts. As a consequence, accelerator power converters occupy a unique position at the intersection of high power, high precision, and high reliability power systems.

Among these systems, the Proton Synchrotron (PS) plays a key role in CERN's accelerator chain. Operating since 1959 and continuously upgraded, the PS accelerates protons and ions and injects them into the following machines. Its magnets are powered in a pulsed regime, with repetitive current cycles synchronized with the beam acceleration. Supplying such loads directly from the electrical grid would cause unacceptable power fluctuations. To overcome this limitation, CERN developed the POwer converter for Proton Synchrotron (POPS), a large pulsed power supply that decouples the grid power from the magnet power by using local capacitive energy storage.

POPS is a complex, multi-stage power electronic system capable of delivering peak powers on the order of tens of megawatts while maintaining very high regulation accuracy. Energy is stored in capacitor banks, exchanged with the magnet during the acceleration cycle, and recovered at the end of each pulse. From a control perspective, this architecture introduces strong coupling between energy storage, conversion stages, and the magnet load. In addition to accurate magnetic field tracking, the control structure must manage the capacitor voltages, balance internal variables, and ensure safe operation under both nominal and degraded conditions.

Historically, the control of accelerator power converters at CERN has relied on well-established control techniques such as RST controllers or state feed-feedback control (Boattini 2015) (Spierer 2022). These methods have proven robust and reliable performances over decades of operations. However, the increasing complexity of converter topologies, the integration of energy storage, and the demand for

improved flexibility and fault tolerance motivate the exploration of alternative, more systematic control approaches. In this context, model-based control structures that explicitly take into account energy flows and physical causality are of particular interest.

Energetic Macroscopic Representation (EMR) is a graphical formalism to respect both, energy flows and causality. EMR provides a unified framework for organisation of models of complex systems based on the explicit representation of states variables (Bouscayrol 2000). EMR offers a systematic way to derive control structures through inversion principles. By distinguishing between static and dynamic relations and enforcing physical causality, EMR leads to control architectures that are directly linked to the energetic properties of the system. This approach has been successfully applied to a wide range of electromechanical and power electronic systems and has progressively gained acceptance at CERN. For example, the EMR-based inversion control has been already proposed for the SIRIUS modular power converter (Horrein 2020) and for the POLARIS converter family (Baziz 2025).

The inversion-based control derived from EMR is particularly well suited for power supplies such as POPS. It allows the designer to explicitly see power flows, and internal variables that requires control. Moreover, the resulting control structures are physically interpretable, which is a crucial advantage in an industrial and operational environment where transparency, validation, and long-term maintainability are essential.

The work presented in this PhD is positioned at the intersection of control structure and large-scale accelerator power electronics. Its primary objective is to investigate the feasibility and performance of an inversion-based control for the POPS system derived from EMR. The proposed approach aims to ensure ultra-precise tracking of the magnet magnetic field cycle while simultaneously managing the energy stored in the capacitor banks and maintaining internal balance constraints.

To achieve these objectives, the PhD follows a progressive approach. A detailed modelling of the POPS power converter is first developed using the EMR formalism, starting from a reduced unitary converter and extending to the complete system. Based on this representation, an inversion-based control structure is systematically derived, highlighting the role of each control loop and its associated physical objective. The performance of the proposed control structure is then evaluated through simulation under demanding operating conditions and compared with existing control solutions.

Beyond simulation, experimental validation plays a central role in this work. Reduced-power platforms, mini-POPS-B and mini-POPS, are used to implement and test the inversion-based control in realistic conditions. These experiments provide valuable insight into practical issues such as measurement noise, parameter dispersion, and real-time implementation constraints, and they allow an objective assessment of the benefits and limitations of the proposed approach.

More broadly, this PhD contributes to the ongoing evolution of control methodologies for accelerator power converters at CERN. By demonstrating how inversion-based control and EMR can be applied to a complex, industrial-scale system such as POPS, it aims to provide tools and concepts that can support future upgrades and next-generation accelerator projects. In a context where performance requirements continue to increase while reliability and efficiency remain paramount, such systematic and physically grounded control approaches are expected to play an increasingly important role.

Chapter 1 is devoted to define the technical requirement of the PhD. Chapter 2 is focused on the EMR and the inversion-based control of a unitary power converter. Chapter 3 deals with the extension to complete POPS. Chapter 4 presents the real-time implementation of the developed inversion-based control on a reduced scaled experimental platform.

I. Context and Objective

This chapter introduces the context and objectives of the PhD. It first presents the technological and scientific background of particle accelerators, with a particular focus on the electrical and control challenges associated with accelerator magnet power converters. The specific environment of the CERN accelerator complex and the evolution toward future infrastructures are then discussed. Finally, the chapter positions the research within this context by describing the POPS system, the principles of inversion-based control using Energetic Macroscopic Representation, and the objectives and methodology of the PhD work.

I.1. Background and motivations

I.1.a. Particle accelerators

Particle accelerators are complex systems in which electromagnetic fields are used to accelerate, guide, and focus charged particle beams. While their scientific purpose is rooted in particle physics, their practical realization strongly depends on large-scale power electronics, high-precision control, and energy management. From a power-engineering perspective, an accelerator can be seen as a distributed load composed of thousands of tightly regulated electromagnetic actuators operating under extreme accuracy and reliability constraints (Wiedemann 2015) (Lee 2011).

The acceleration itself is achieved through electric fields, typically generated by radiofrequency (RF) cavities, which transfer energy to charged particles. Magnetic fields are used to shape the beam trajectory and maintain stability. Dipole magnets bend the beam, quadrupole magnets focus it, and higher-order magnets correct imperfections. The strength of these magnetic fields is directly proportional to the current flowing in the magnet windings, making the performance of the accelerator inseparable from the performance of its power supply system (Evans 2018).

Particle accelerators can be divided into linear and circular machines (Figure 1). Linear accelerators (linacs) rely on a sequence of accelerating structures arranged along a straight line. From a power-electronics standpoint, linacs are characterized by RF power systems operating at high frequencies and pulsed regimes, often optimized for efficiency and peak power handling (Wangler 2008). However, their length increases rapidly with target energy, limiting their scalability for very high-energy physics.

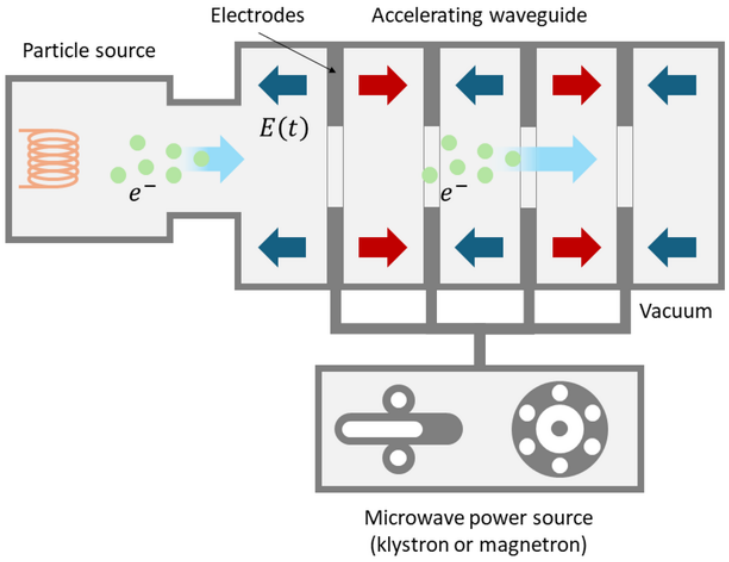


Figure 1: Schematic of a linear accelerator (Panaino 2025)

Circular accelerators (synchrotrons) reuse the same accelerating structures over many revolutions. This architecture dramatically reduces the required RF infrastructure but introduces strict constraints on magnet power supplies (Medvedko 1998). As particle energy increases, the magnetic field must be ramped synchronously to maintain a constant orbit radius. This results in repetitive current cycles with large amplitudes, fast dynamics, and extremely tight tolerances (Figure 2).

In a synchrotron, the magnet current waveform defines the beam energy and optics. Any deviation in current directly translates into orbit distortion or beam loss. As a result, accelerator magnet power converters must combine high power ratings with very high precision, often better than 10^{-6} relative accuracy over long operating periods. This requirement goes well beyond classical industrial power supplies and place accelerators among the most demanding applications of power electronics.

The main components of particle accelerators are radiofrequency (RF) cavities, dipole magnets and quadrupole magnets.

RF cavities are resonant metallic structures that sustain an oscillating electromagnetic field. When charged particles pass through a cavity, it experiences an accelerating electric field along its direction of motion.

Dipole magnets produce a uniform magnetic field across the beam aperture. When charged particles move through this magnetic field, the Lorentz force bends their trajectory, allowing them to follow a curved path inside the accelerator.

Quadrupole magnets generate a magnetic to focus the beam in one transverse direction while defocusing it in the perpendicular direction. By arranging quadrupoles in alternating sequences, net focusing is achieved in both transverse directions, keeping the beam confined.

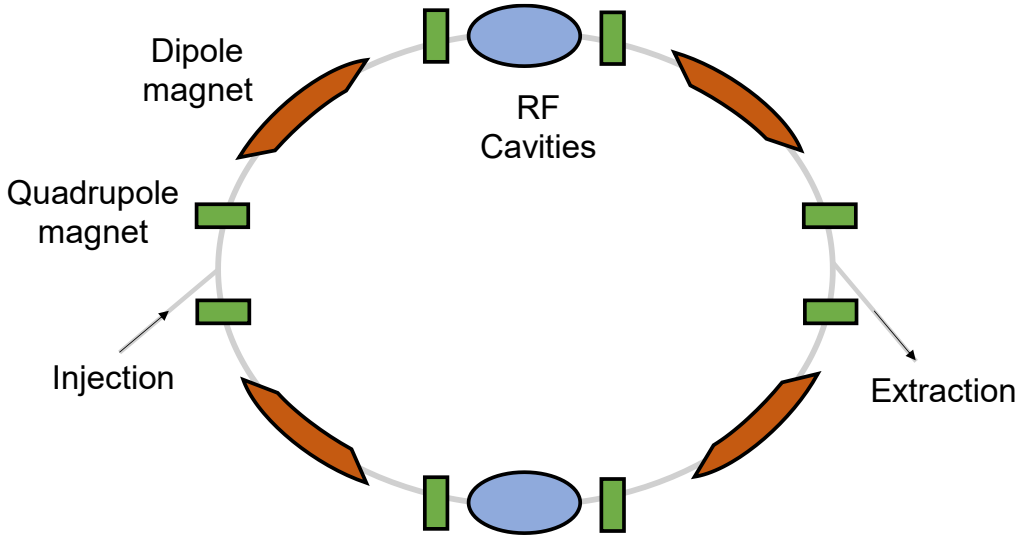


Figure 2: Simplified synchrotron showing dipoles, quadrupoles, and RF cavities

CERN's accelerator complex provides a representative example of these challenges. Rather than a single machine, CERN operates a chain of synchrotrons, each feeding the next at a higher energy level (Figure 3). At each stage, magnet power supplies must generate accurately synchronized current profiles while interacting with upstream and downstream systems. From a system perspective, this results in a large number of power converters operating simultaneously, often with correlated dynamics.

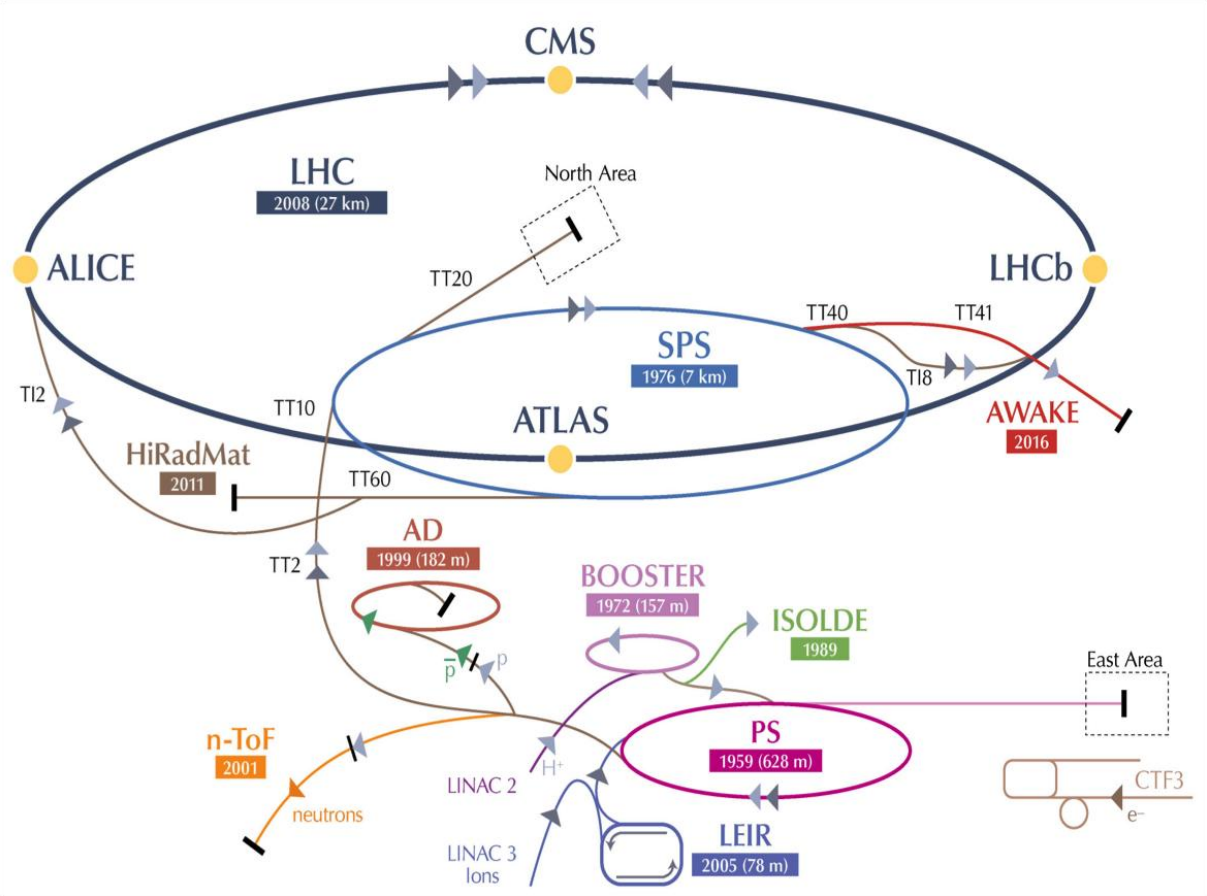


Figure 3: Particle accelerator, sensors and their junction (Gschwendtner 2016)

The Large Hadron Collider (LHC) represents the extreme end of this spectrum. Its superconducting dipole and quadrupole magnets operate at cryogenic temperatures and carry currents of several kiloamperes (Brüning 2004). Although the superconducting coils exhibit negligible resistive losses in steady state, their inductive nature dominates the electrical behaviour. Consequently, magnet powering is characterized by very low voltages, very high currents, and large stored magnetic energies. Power converters must therefore handle energy ramp-up and recovery phases safely, efficiently, and reproducibly.

Even in smaller synchrotrons such as the Proton Synchrotron (PS, see Figure 3), the electrical demands are severe. Magnet circuits are pulsed with cycle times on the order of seconds, and current tracking errors must remain within tens of parts per million (ppm). To reduce stress on the electrical grid, local energy storage elements, such as capacitor banks, are often integrated into the power system. This introduces additional complexity in power flow management and control, requiring coordinated regulation of multiple conversion stages.

From a control perspective the accelerator power converters must reject disturbances originating from the grid, load coupling between magnets, and internal nonlinearities, while guaranteeing reproducible

current waveforms. Classical control approaches, such as PID or RST regulators, have been widely used, but the increasing complexity of accelerator power systems motivates the adoption of more model-based control methods. These approaches aim to directly compensate system dynamics and improve robustness, particularly during transient operating phases.

In summary, particle accelerators can be viewed as large-scale, tightly coupled power-electronic systems whose performance is defined as much by electrical engineering as by physics. The need for high power, extreme precision, fast dynamics, and continuous operation makes accelerator applications a unique testbed for advanced power conversion and control techniques (Burnet 2015). CERN's accelerator infrastructure exemplifies these challenges and provides a reference framework for the development of next-generation power-electronic systems.

Particle accelerators are not used solely for fundamental research, they also have important applications in industry and medicine (Garnett 2015). In industry, low-energy accelerators ranging from a few hundred electron volts up to about 500 keV are employed for ion implantation in the manufacturing of semiconductor materials, microcircuits, and electronic chips (Gardner 1987).

In the medical field, accelerators play a crucial role in the treatment of cancer, particularly in radiotherapy (Silari 2011), as well as in diagnostic imaging and the sterilisation of medical equipment (Yu 2014).

I.1.b. Challenges of control of these power converters

Power converters used in particle accelerators belong to a very specific class of electrical systems, combining high power levels with extreme precision and reliability requirements. Unlike most industrial applications, where moderate regulation accuracy is sufficient, accelerator magnet power converters directly determine beam dynamics. As a result, their control represents a critical challenge that extends beyond classical power electronics and into system-level coordination, disturbance rejection, and long-term stability (Evans 2018) (Josifović 2017).

One of the primary difficulties arises from the nature of the load itself. Accelerator magnets are highly inductive elements, often connected in long series circuits. The electrical behaviour of these circuits is dominated by large inductances and, in the case of superconducting magnets, extremely low resistance. From a control standpoint, this means that even small voltage errors can lead to significant current deviations over time, while fault scenarios can involve the rapid release of large amounts of energy (Brüning 2004) (Mentink 2023).

In synchrotron accelerators, magnet currents are not constant but follow predefined, repetitive cycles synchronized with beam energy. These cycles can include fast ramps, flat tops, and controlled de-excitation phases. The control system must ensure accurate tracking of these reference waveforms over thousands of repetitions, often with relative errors below 10^{-5} and, in some cases, approaching 10^{-6} (Burnet 2015). Achieving such precision is challenging not only because of converter nonlinearities, but also due to external disturbances and parameter variations.

A major source of disturbance is the electrical grid. Large accelerator power converters are typically connected to medium- or high-voltage distribution networks and may operate simultaneously in large numbers. Grid voltage fluctuations, harmonic distortion, and transient events can all propagate through the conversion stages and affect the output current. While modern active front-end rectifiers can mitigate some of these effects, the control system must still ensure strong decoupling between grid-side perturbations and magnet current regulation (Medvedko 1998).

Another challenge lies in the multi-stage nature of accelerator power converters. A typical architecture includes an active front end, an intermediate DC link, and one or several DC/DC conversion stages feeding the magnet circuit. Each stage has its own dynamics, constraints, and control objectives. Coordinating these stages while preserving overall system stability is non-trivial, particularly when energy storage elements such as capacitors or supercapacitors are introduced to reduce grid power peaks. In such cases, control strategies must manage bidirectional power flows and ensure seamless transitions between operating modes (Coulinge 2022).

The precision requirements imposed on magnet current regulation also place strict demands on measurement systems. Current sensors must provide high resolution, low noise, and excellent long-term stability. Any offset, drift, or quantization error directly translates into a systematic error on the magnetic field. Control algorithms must therefore be designed to account for measurement imperfections, often relying on calibration procedures and compensation techniques. This further complicates controller design and validation (Lauria 2022).

Thermal effects introduce another layer of complexity. Power electronic components, magnetic elements, and sensors are subject to temperature variations that modify electrical parameters over time. In long accelerator runs, which may last for weeks or months, these slow parameter drifts can degrade control performance if not properly addressed. Controllers must therefore remain robust against changes in resistance, inductance, and semiconductor characteristics, without requiring frequent retuning (Josifović 2017).

In addition to steady-state accuracy, transient behaviour is of critical importance. During current ramps, injection and extraction phases, or fault recovery, the system must remain stable and predictable.

Overshoots, delays, or oscillations can have direct consequences on beam quality or even trigger machine protection systems. Designing controllers that combine fast dynamic response with ultra-high precision remains a central challenge in accelerator power electronics (Bordry 2020).

Reliability and availability further constrain control strategies. Accelerator facilities such as CERN operate continuously and are expected to deliver beams according to tight schedules. Power converter faults or control instabilities can lead to significant downtime. As a result, control algorithms must not only perform well under nominal conditions, but also degrade gracefully under fault scenarios. This requirement often limits the use of overly aggressive or computationally complex control schemes, favouring approaches that are transparent, verifiable, and robust.

Historically, classical control structures such as PID, state feedback, and RST regulators have been widely adopted in accelerator power converters due to their simplicity and proven reliability (King 2015). However, as converter architectures become more complex and performance requirements increase, these approaches can reach their limits. The need to explicitly account for energy storage, multi-quadrant operation, and strong coupling between subsystems motivates the exploration of more advanced, model-based control techniques (Coulinge 2022), (Scirè 2025).

Finally, the control of accelerator power converters must be considered at the system level rather than in isolation. Magnet circuits interact with each other through magnetic coupling, shared power infrastructure, and coordinated beam operation. Local control decisions can therefore have global consequences. Ensuring consistent behaviour across hundreds or thousands of converters requires standardized control architectures, synchronized timing, and carefully managed interfaces between hardware and software layers.

I.1.c. Future of CERN

The Future Circular Collider (FCC) is a long-term accelerator and research infrastructure project proposed at CERN to extend the exploration of fundamental physics beyond the capabilities of the Large Hadron Collider (LHC). It represents one of the most comprehensive studies undertaken to date for a post-LHC facility and is designed to address key questions in particle physics (Benedikt 2025).

The FCC proposal is centred on the construction of a new underground circular tunnel with a circumference of approximately 90–100 km in the Geneva region (Figure 4). This large scale is a critical design choice, as it enables higher beam energies while mitigating limitations from synchrotron radiation and magnetic field strength, particularly for hadron colliders (Benedikt 2025). The FCC is conceived as a staged facility**,** beginning with a high-luminosity electron–positron collider (FCC-ee) and followed by a high-energy proton–proton collider (FCC-hh) installed in the same tunnel (Benedikt 2025).

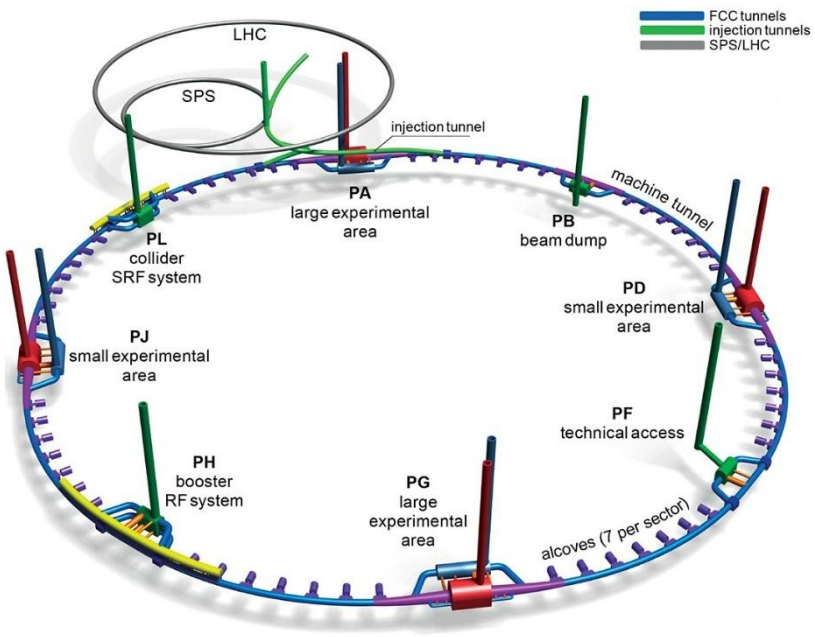


Figure 4 :layout of FCC (Cern Courrier)

A central motivation for the FCC is the need for precision measurements following the discovery of the Higgs boson at the LHC. While the LHC has confirmed the existence of the Higgs particle, many of its properties are still known with limited accuracy. FCC-ee is designed to run at different energies, allowing very precise measurements of fundamental particles and their properties (Benedikt 2025).

To orchestrate all the control, a FGC3 (Function Generator/Controller) is used. The FGC3 is an embedded control computer developed at CERN for managing power converters used in particle accelerators. It is part of a family of Function Generator/Controllers that generate control functions, regulate current and magnetic fields, and manage the state of power supplies in accelerator systems. The FGC3 platform combines a microcontroller, a digital signal processor (DSP), and an FPGA to handle precise control tasks and interfaces directly with the power converter hardware (Page 2019).

The Function Generator/Controller 4 (FGC4) represents the latest evolution of CERN's power converter control platform, designed to improve the performance limits and component obsolescence of its predecessor (FGC3) while addressing the demanding requirements of modern accelerator systems. Historically, FGC devices have been central to controlling, monitoring, and diagnosing thousands of power converters in the CERN accelerator complex. However, increasing regulation speed and integration needs have driven the development of FGC4 with a significantly enhanced hardware and software architecture (Zielinski 2025), (Cejp 2023).

I.2. PhD positioning

I.2.a. POPS control

The POPS (Power converter for Proton Synchrotron) system at CERN represents a class of static pulsed power supplies designed to drive large magnet loads in cyclic accelerators such as the Proton Synchrotron (PS). POPS is engineered to deliver and recover high-power pulses up to 60 MW peak with minimal perturbation to the electrical grid, by using capacitive energy storage and multiple power converter stages in a tightly controlled architecture (Fahrni 2007a), (Fahrni 2007b).

In pulsed accelerators, the magnet load requires current profiles with rises and falls in the order of tens of milliseconds, followed by intervals where the stored energy is returned to the supply. Directly using the grid to power these pulses is impractical due to the excessive active and reactive power fluctuations. POPS tackles this by decoupling power from grid supply with capacitor banks that store energy locally and exchange it with the electromagnet during the cycle, while grid-connected AC/DC rectifiers (Active Front Ends, or AFEs) supply only system losses (Fahrni 2007a). The different values of the POPS parameters are given in annexe-C.

The topology of POPS comprises two AC/DC Active Front Ends feeding six DC/DC converters connected to six capacitor banks. Four converters operate in “floating” mode with no direct connection to the grid, while two act as “chargers”, connected to the grid with AFEs (Figure 5). This modular and redundant structure allows system operation even with the loss of one converter or capacitor bank, maintaining performance with reduced time between each pulse (Fahrni 2007a), (Péron 2009).

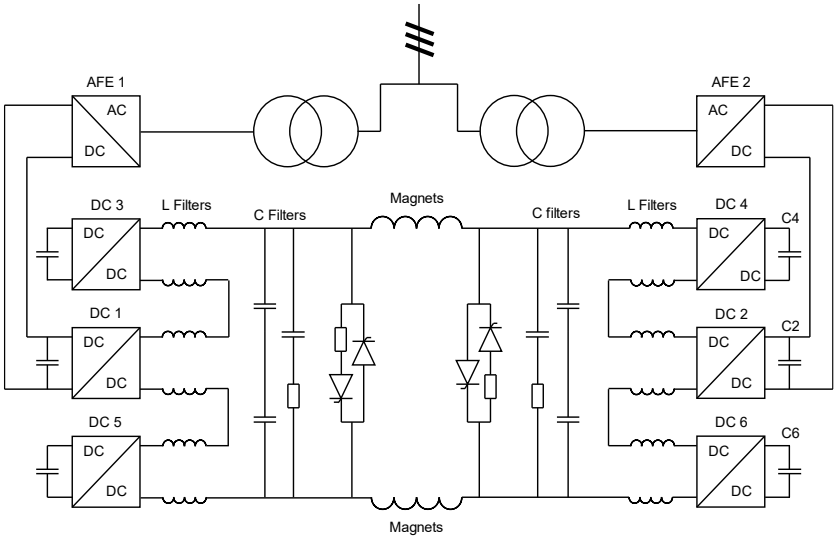


Figure 5: Schematic of POPS

The 60 MW particle accelerator is an enormous piece of scientific infrastructure. The capacitor banks alone are each the size of standard shipping containers, while the converters and power filters occupy a large electrical room (Figure 6)(annexe-D). The beam itself extends for 628 meters, stretching well over half a kilometre, making the entire installation a facility-scale machine rather than a single piece of equipment.

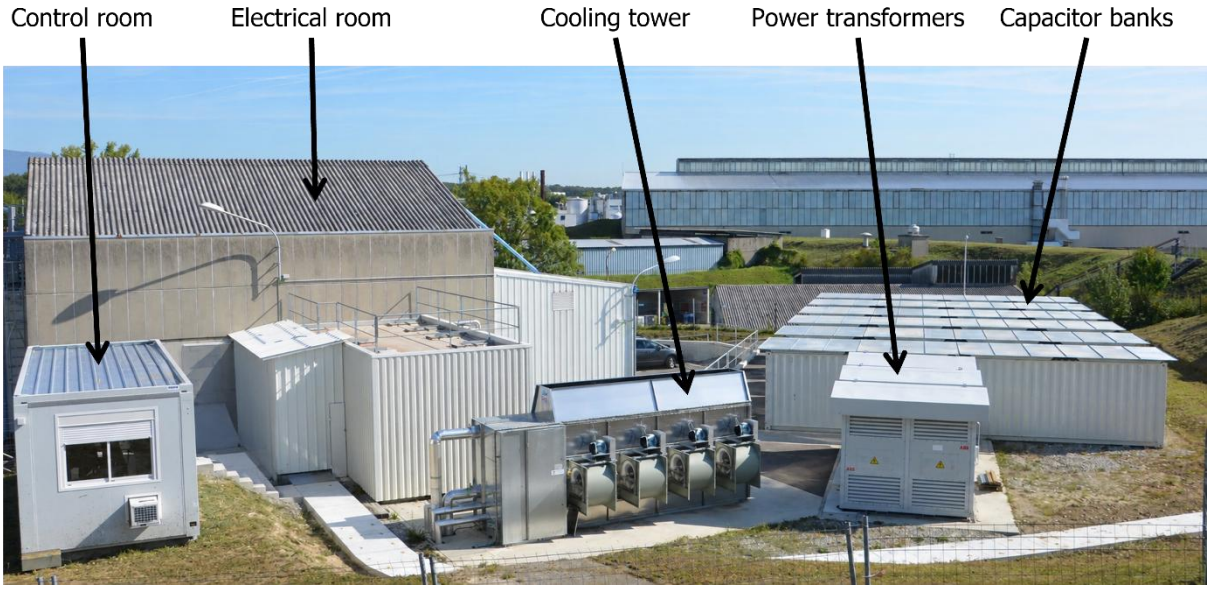


Figure 6 : Photograph of the POPS installation

From a control perspective, the primary challenges stem from a high-precision regulation requirement. The magnetic field must be controlled within defined tolerances (less than 100 ppm during injection and flat tops) because even minor deviations can destabilize particle beams. An energy exchange, during the pulse, energy flows between the capacitive storage and the magnet load. The control must orchestrate this exchange such that the stored voltages remain within allowable bounds while the references are followed precisely. And a balance management among the currents of the converter legs and the storage capacitor banks, which requires a voltage and current balance strategies, especially during transitions between charge, discharge, and idle states (Fahrni 2008).

To address these challenges, POPS implements a hierarchical digital control architecture (Figure 7). An outer loop regulates the magnetic field or current reference (Bfield/Imag), generating a total output voltage reference based on high-level accelerator timing and physics requirements (Boattini 2015).

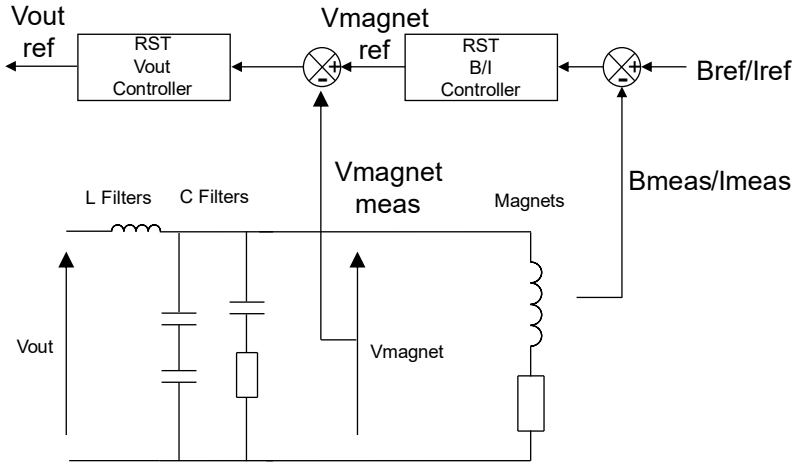


Figure 7: POPS control loops

An intermediate allocation layer distributes the total output voltage among individual DC/DC converters, accounting for voltage and current imbalance corrections. Inner loops control each converter legs, commanding switch-level actions (via PWM) to achieve the reference voltages and currents with high bandwidth and stability.

All control loops in POPS are digital and implemented using RST (polynomial) regulators, which allow robust tracking and disturbance rejection tailored to the specific dynamics of the output filters and magnet loads. System identification techniques are employed to model the combined output filter and magnet transfer functions, refining the RST parameters to achieve the necessary loop bandwidths (160 Hz for voltage tracking) and rejection performance.

The hardware control platform is based on CERN's Function Generator/Controller (FGC) computers and main controllers. The FGC synchronizes all converters to the accelerator timing system, ensuring that reference signals and measurement acquisition are phase-aligned across the whole system.

A key control feature of POPS operations includes redundancy management, allowing operation under converter or capacitor bank faults, with control strategies that reallocate the reference and modify current profiles accordingly.

These strategies ensure that POPS meets both the dynamic pulse shaping demands of the accelerator magnets and the stability and precision requirements necessary for reliable beam operation.

I.2.b. Inversion-based control and EMR

The control of complex systems involving multiple physical domains such as electrical, mechanical, thermal, or hydraulic requires methodologies that preserve physical causality while enabling systematic control organisation. Energetic Macroscopic Representation (EMR) addresses this need by providing a unified graphical formalism for modelling multi-domain systems and by enabling inversion-based control design grounded in energetic principles (Bouscayrol 2012).

EMR originates from systemic design methodologies, where systems are decomposed into interconnected subsystems according to their energetic function rather than purely mathematical descriptions. In EMR (Bouscayrol 2000), a system is represented using a limited set of canonical elements: energy sources, energy accumulation elements, energy conversion elements, and energy distribution elements. Each element is associated with effort and flow variables, ensuring a physically meaningful description of energy exchanges and enforcing integral causality throughout the system (Bouscayrol 2012).

A central contribution of EMR lies in its explicit link between modelling and control. Once the energetic model organisation of a system is established, the control organisation is deduced through a systematic inversion procedure. Static relations, typically associated with conversion elements, can be inverted directly, while dynamic relations linked to energy accumulation elements require indirect inversion through feedback controllers. This approach avoids differentiation of measured signals and preserves robustness against modelling uncertainties (Bouscayrol 2012).

The result of this ideal inversion process is called Maximal Control Structure (MCS). The MCS represents the theoretical control architecture that allows independent control of each energetic storage element while respecting physical constraints and causality. In practice, the MCS provides a reference from which a simplified or an implementable control structure can be derived without losing the energetic coherence of the original system (Bouscayrol 2012). This concept is particularly valuable for complex systems where multiple control objectives coexist across different time scales. However, any simplification leads to reduced performances. In the case of CERN application (accuracy of 100 ppm) it is not relevant.

Inversion-based control within the EMR framework differs fundamentally from classical control approaches such as state-space feedback or transfer-function-based design. Rather than starting from a mathematical model and selecting control variables a posteriori, EMR dictates control paths directly from the energetic structure of the system. This ensures that each control loop corresponds to a physically meaningful objective, such as regulating stored energy or enforcing power balance, thereby improving transparency and interpretability of the control design.

Recent works have further demonstrated the relevance of EMR and inversion-based control for modern energy systems. Applications include wind energy conversion systems (Bouscayrol 2009), fuel cell systems (Boulon 2012) (Depature 2018), Energy Storage Systems (Castaings 2016) (Nguyen 2019), hybrid vehicles (Letrouvé 2013) (Lhomme 2017) (Li 2021), electric vehicle, including thermal comfort (Desreveaux 2019) (Ramsey 2022) (Aroua 2023) (Li 2025), subways (Allègre 2010) (Mayet 2014) (O'Beriel 2025), Hardware-in-the-Loop testing (German 2024) (Tournez 2025), charging stations and batteries (Ndiaye 2024) (Fadili 2025), where strong coupling between subsystems and nonlinear behaviour complicates conventional control synthesis. These studies highlight how EMR facilitates modular design, systematic tuning, and robust performance, especially in systems operating under wide-ranging conditions.

I.2.c. Inversion-based control at CERN

The development of advanced control methodologies for power converters is a central issue at CERN, where electrical systems are required to deliver extreme dynamic performance, very high precision, and strong robustness against disturbances. In particular, the powering of accelerator magnets especially fast pulsed magnets for beam injection and extraction imposes strict constraints on both transient response and steady-state accuracy. Within this context, Energetic Macroscopic Representation has emerged at CERN as a relevant framework for the modelling and control of complex electromechanical and power electronic systems.

EMR is a graphical representation methodology based on the explicit modelling of energy exchanges between subsystems. Introduced initially for electromechanical systems, EMR has been progressively extended and adopted at CERN for power electronics and pulsed power applications. The Sirius power converter, a particle injector between PSB and POPS, has been controlled using inversion-based control (Figure 8) (Horrein 2017). Further studies have shown inversion-based control was simpler to implement than an RST control (Ortega 2020). Additional study demonstrated that compared to state-feedback, inversion based-control was more flexible and enabled more strategies (Godart 2022).

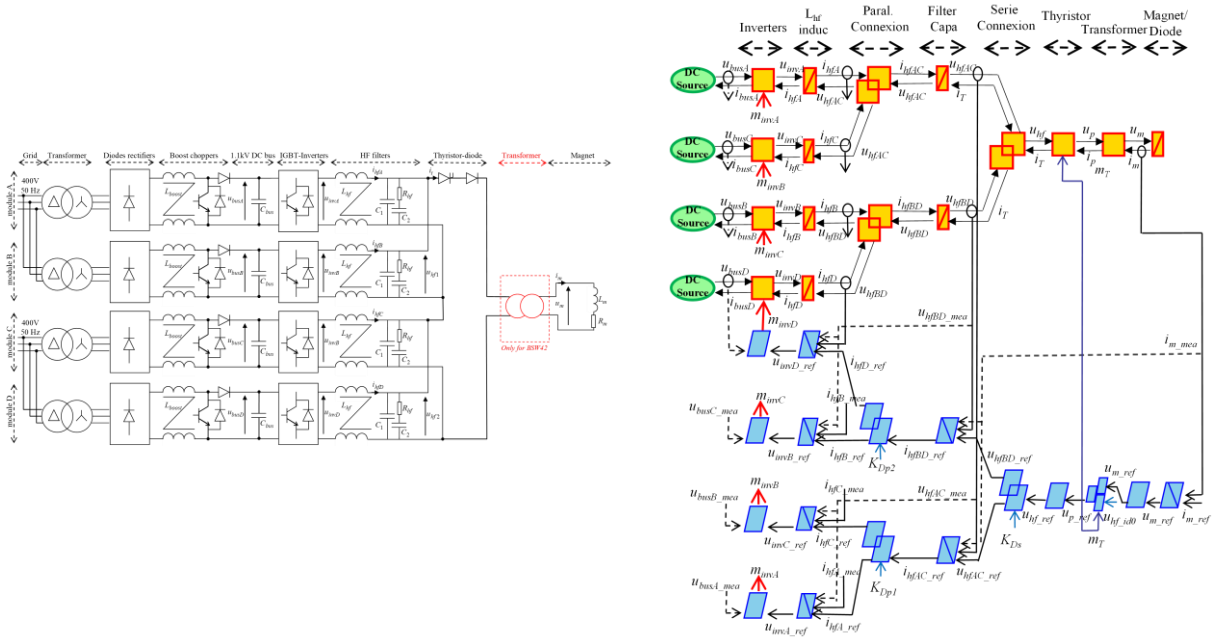


Figure 8: Electrical schematic of Sirius power converter and its EMR (Horrein 2017)

Another converter, named POLARIS (Figure 9), has been controlled using inversion-based control (Baziz 2025). Polaris is a converter intended to supply the majority of standard magnet circuits in transfer lines and experimental zones. Including quadrupole, small dipole, and corrector magnets in the North Area and transfer line of the Super Proton Synchrotron (SPS) experimental infrastructure.

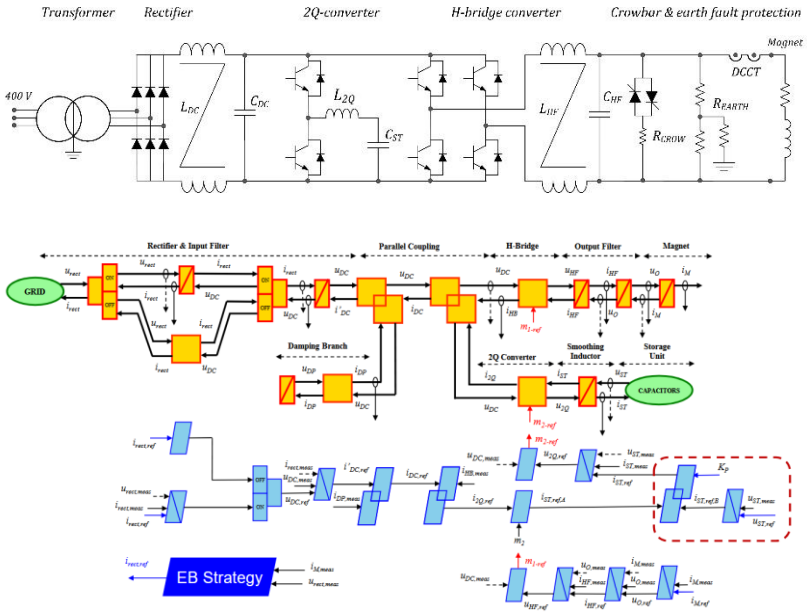


Figure 9: Electrical schematic of POLARIS and its EMR (Baziz 2025)

At CERN, EMR is extensively used in the design of power converters supplying accelerator magnets, where multiple energy domains electrical and magnetic interact. A representative example is the control of fast pulsed power converters combining capacitor discharge stages and switch-mode converters.

These systems must generate current waveforms with sub-percent accuracy, often in the range of hundreds or thousands of amperes, and with rise times of a few seconds or less. Classical control approaches, such as state-space or RST control, become difficult to scale and tune due to the strong coupling between subsystems and the presence of multiple time constants.

The EMR-based approach starts with a description of the converter and the load. Capacitors and inductors are modelled as energy accumulation elements, semiconductor bridges as conversion elements, and interconnections as distribution elements. This macroscopic view allows to identify the control path of variables and the internal constraints of the system. From this representation, the control structure is deduced by inversion rules.

One of the major advantages of EMR-based control at CERN is its transparency and flexibility. Since control loops are derived from physical principles rather than purely mathematical abstractions, the resulting controllers are easier to interpret, tune, and validate. This is crucial in an accelerator environment, where reliability and predictability are as important as performance. Moreover, EMR naturally supports hierarchical control structures, enabling a clear separation between fast inner loops and slower outer loops.

In addition, EMR facilitates the comparison and integration of different control strategies. Several CERN studies have demonstrated how EMR-based control can be benchmarked against classical RST or state-feedback controllers on the same converter topology (Horrein 2017), (Ortega 2020), highlighting trade-offs in terms of disturbance rejection, implementation complexity, and sensitivity to parameter variations. In pulsed applications, EMR-based controllers have shown excellent capability to handle large signal operation and non-linear behaviours, such as those induced by semiconductor switching and magnetic saturation, without requiring excessive linearization assumptions (Horrein 2020).

EMR-based control has become a powerful adopted methodology at CERN for the control of advanced power converters. Its energetic foundation, systematic control synthesis, and strong physical consistency make it particularly well suited for the demanding requirements of particle accelerator applications.

I.3. Research framework and objectives

I.3.a. Objectives of the PhD

The main objective of this PhD is to develop an inversion-based control for the POPS system in order to ensure operation under both normal and fault operation modes.

As a first step, an inversion-based control of a reduced version of the existing POPS system is investigated to assess its feasibility and performance. The main constraints associated with this control are the accurate tracking of the magnetic field cycle (Figure 10), with a precision of 100 ppm during the injection and acceleration phases, as well as the management of the energy stored in capacitor banks. The voltage of the charger capacitors must not go below 3100 V. For the floating capacitor banks, the voltage must not fall below 2000 V during a cycle and must return to their nominal value of 5000 V at the end of the cycle.

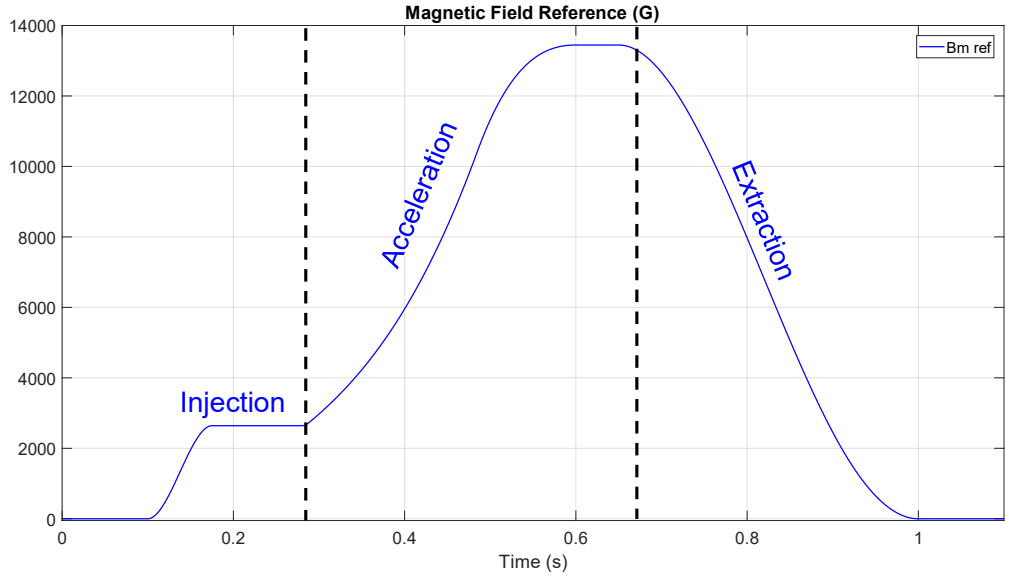


Figure 10: Example of magnetic cycle

I.3.b. Tools and methods

The development of the inversion-based control organisation relies on the use of the Energetic Macroscopic Representation formalism. This formalism enables the organization of the system model according to interaction and causality principles, thereby facilitating the systematic derivation of an appropriate control structure.

All modelling and simulation activities are carried out using the MATLAB/Simulink environment. The reference selected for the simulations corresponds to the current cycle requiring the highest current. This choice is motivated by the fact that, under these conditions, the system operates close to the saturation limits of the modulation ratios. Consequently, if the control performs satisfactorily under this worst-case scenario, it is expected to operate correctly for less demanding reference cycles as well.

In addition to numerical simulations, experimental validation is conducted using reduced-power experimental platforms, namely mini-POPS and mini-POPS-B. These platforms provide a

representative hardware environment for testing the proposed control while limiting operational risks. They are used to evaluate the behaviour of the inversion-based control under nominal operating conditions.

I.3.c. Contribution of the PhD

This PhD is expected to contribute to the development of advanced control strategies for the POPS system by proposing an inversion-based control architecture adapted to the specific constraints of high-power pulsed power supplies.

At a methodological level, the work provides a structured application of the Energetic Macroscopic Representation formalism to design an inversion-based control for the POPS system. The proposed approach has to address future steps in normal operating modes and will integrate new energy management strategies in order to comply with the operational and safety constraints of the system.

Overall, this work aims to deliver a validated control solution and associated modelling tools that can support future developments and upgrades of the POPS system, while remaining focused on the specific industrial context and requirements of the application.

In order to comply with the complexity of POPS, the work is decomposed in 2 phases. First, the EMR and the inversion-based control of an unitary converter are proposed (Chapter II). In a second phase, the EMR and inversion-based control are extended to the multi-stage complete POPS (Chapter III).

II. Inversion-based control of a unitary converter

This chapter develops the mathematical modelling of the unitary POPS. It then translates this model into the EMR formalism, providing the framework required to design and implement the inversion-based control strategy. In order to develop the inversion-based control of the POPS, a progressive approach is used. An elementary unit is considered in this Chapter. The mathematical modelling of this unit is developed and then, this model is organised using EMR. An inversion-based control of this elementary unit is derived within this framework. First simulation results are provided to check the required performances.

II.1. From unitary converter to the complete system

The unitary converter of POPS (Figure 11) consists of an Active Front End (AFE) converter connected to the grid. The AFE supplies power to a storage capacitor, which serves as a DC link. This capacitor is connected to a six-legged, three-level converter. The use of six legs makes it possible to achieve an output voltage with a ripple of 2000 Hz when the switching frequency is only 333 Hz.

Each leg of the converter is connected to a coupled inductive filter. Following the inductive stage, there is a capacitive filter composed of two branches: one containing a capacitor, while the other branch consists of a capacitor in series with a resistor. At the end the electromagnet is formed by a total of 101 magnet in series (the electromagnet, modelled by an equivalent R-L circuit). The complete system scheme is illustrated below.

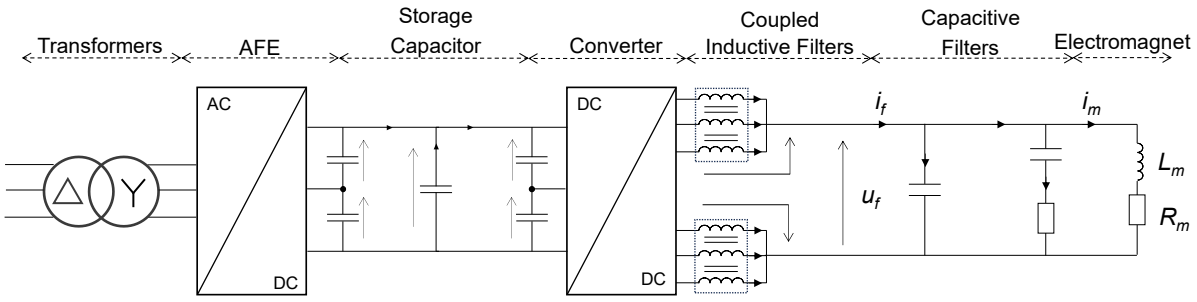


Figure 11: Electrical scheme of a unitary converter

From the unitary system to the complete POPS system, additional elements are introduced (Figure 12). Two DC-DC converters are added in series, interconnected through a coupled inductive filter (composed of 2 distinct three-phase inductances). The added converters are implemented as floating converters, meaning they are not directly connected to the grid. The capacitive filter and magnet remain unchanged. These converters and filters are duplicated and arranged symmetrically with respect to the magnet. To enable this mirrored topology, the magnet is schematically divided into 2 equal halves to allow each half of the magnet to be connected in series.

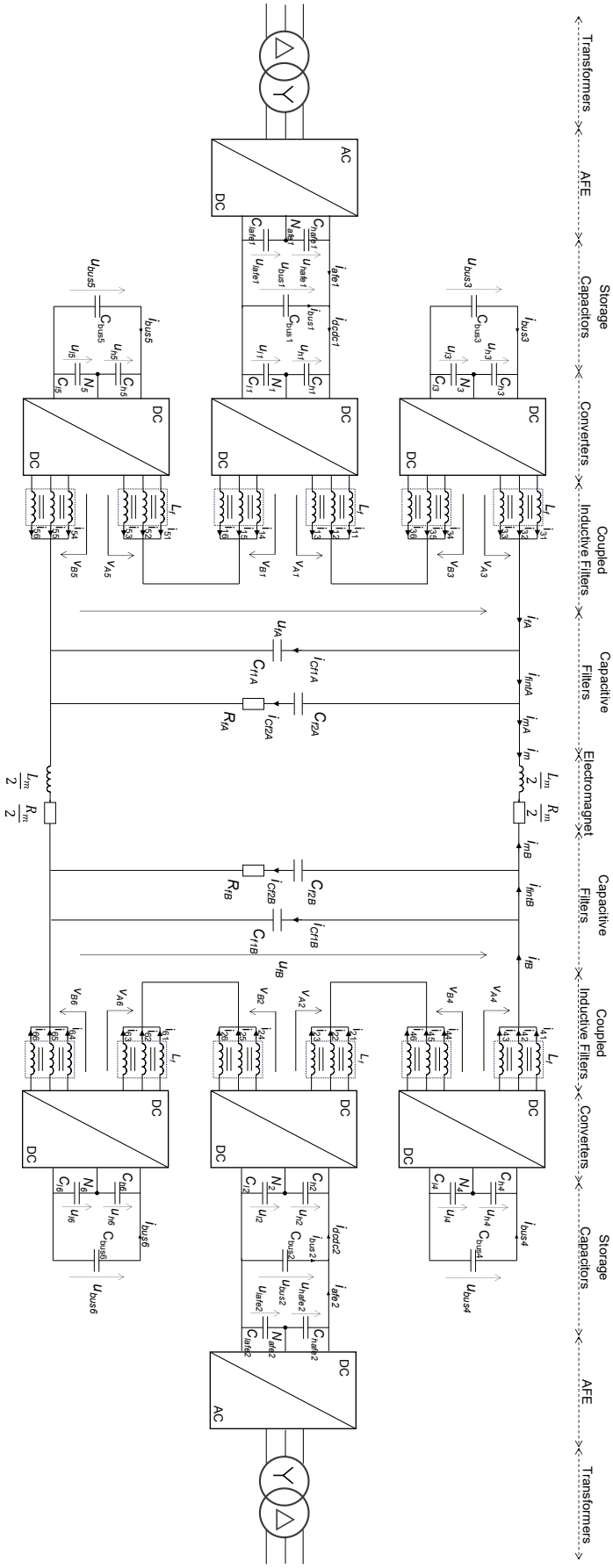


Figure 12: Electrical Scheme of the complete system

POPS is a complex converter with a total of 8 converters. Two AFEs are connected to the grid and supply energy to two charging capacitors, whose primary function is to compensate the joule losses occurring during a cycle. The remaining 4 storage capacitors, referred to as floating capacitors, supply the inductive load and recover their energy during a cycle. As these floating capacitors are not directly connected to the grid, they are pre-charged at 5000 V at the beginning of each cycle.

Each leg of a converter requires its own current-control mechanism. When the switches in a leg commutate, the current i_f no longer flows through a single path but is redistributed among 3 legs of the converter. Due to the interleaved switching, the current distribution is not uniform, so individual legs can carry either more or less current than expected, creating an imbalance that must be controlled. The capacitor voltage bridge divider needs to be balanced. This configuration allows POPS to deliver a high-accuracy, high-stability output to the magnet while maintaining a minimal stress on the grid.

II.2. EMR of the unitary converter

This section tackles the modelling of the POPS with one module using mathematical equations. Then are then organized using EMR formalism.

II.2.a. Grid and AFE

The grid and the AFE are assumed to be an equivalent controlled current source. Moreover, the losses of the AFE are not considered.

The grid and the AFE are combined to focus on the internal system dynamics such as the evolution of the capacitor charge and the magnetic field created by the magnet. In this configuration, the current delivered to the charging capacitor is regulated by the AFE control loop, which effectively decouples the load dynamics from the grid. Thus, modelling the grid–AFE combination as an ideal controlled current source is reasonable for analysing the electromagnet electrical and magnetic behaviour.

Losses in the inverters are neglected because they are typically small compared to the total power delivered to the electromagnet. Including them would add unnecessary complexity without significantly affecting the accuracy of the model.

The grid and AFE are modelled as a current source with a maximal power output of 2.5 MW. In EMR this association is depicted by a green oval pictogram (Figure 13).

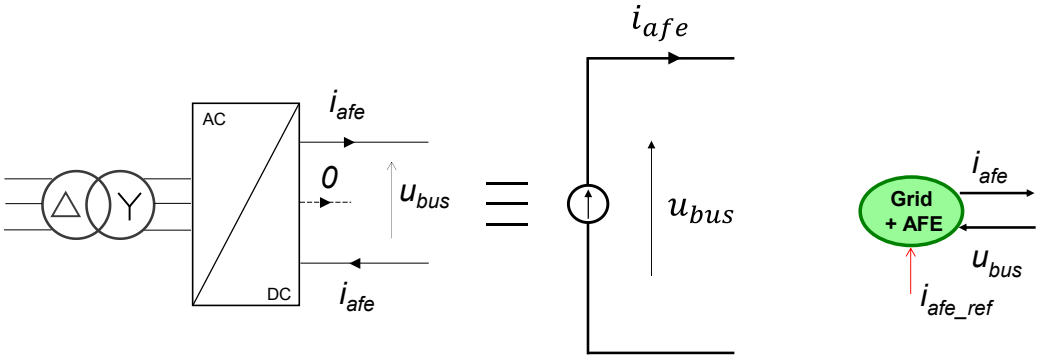


Figure 13: Grid and AFE descriptions

II.2.b. Capacitor storage and capacitor divider

To model the storage capacitor, it is necessary to define the equivalent currents delivered by the AFE voltage bridge and by the DCDC converter. As the capacitors used to make the half voltages influence the current flowing into the storage capacitor, their effect needs to be taken into account in the model.

For the 3-level converter a voltage divider is required upstream. This divider is composed of 2 capacitors in series (Figure 14). A parallel connection is added between the storage capacitor and the capacitors of the voltage divider.

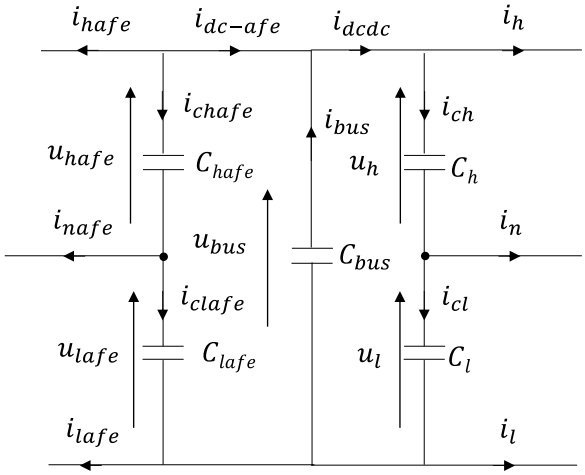


Figure 14:voltage bridge divider at the input of an AFE and DC/DC

The bus voltage is equally distributed:

$$u_{bus} = u_h + u_l = u_{hafe} + u_{lafe} \quad (1)$$

By assumption the capacitance has the same values:

$$C_{eq} = C_h = C_l = C_{hafe} = C_{lafe} \quad (2)$$

The dynamical equation of each capacitor can be derived:

$$-i_{bus} = C_{bus}\frac{du_{bus}}{dt} \quad (3)$$

$$i_{ch} = C_{eq}\frac{du_h}{dt} \tag{4}$$

$$i_{cl} = C_{eq}\frac{du_l}{dt} \tag{5}$$

$$i_{chafe} = C_{eq}\frac{du_{hafe}}{dt} \tag{6}$$

$$i_{clafe} = C_{eq}\frac{du_{lafe}}{dt} \tag{7}$$

The equivalent capacitance of each branch is defined as:

$$\begin{cases} \frac{i_{ch}-i_{cl}}{2} = \left(\frac{C_{eq}}{2}\right)\frac{d}{dt}u_{bus} \\ \frac{i_{ch_AFE}+i_{cl_AFE}}{2} = \left(\frac{C_{eq}}{2}\right)\frac{d}{dt}u_{bus} \end{cases} \tag{8}$$

Using Kirchhoff's junction rule, the currents flowing into the capacitors are defined:

$$\begin{cases} i_{ch} = i_{DCDC} - i_h \\ i_{cl} = i_{DCDC} + i_h \end{cases} \tag{9}$$

$$\begin{cases} i_{ch_AFE} = -i_{DC_AFE} - i_{hAFE} \\ i_{cl_AFE} = -i_{DC_AFE} + i_{hAFE} \end{cases} \tag{10}$$

$$i_{dcdc} = i_{bus} + i_{dc-afe} \tag{11}$$

The voltage difference is defined as:

$$\Delta u = u_h - u_l \tag{12}$$

By combining (1) with (12) leads to:

$$u_h = \frac{u_{bus}+\Delta u}{2} \tag{13}$$

$$u_l = \frac{u_{bus}-\Delta u}{2} \tag{14}$$

The control has to ensure a balance such as:

$$u_h = u_l = \frac{u_{bus}}{2} \tag{15}$$

By focusing on the DCDC part:

$$i_{DC_eq} = \frac{i_h-i_l}{2} = -i_{DCDC} - \left(\frac{i_{ch}+i_{cl}}{2}\right) \tag{16}$$

$$i_n = i_h - i_l \tag{17}$$

The equivalent capacitance of the converter voltage bridge gives:

$$i_n = C_{eq}\frac{d\Delta_u}{dt} \tag{18}$$

The equivalent storage capacitance leads to:

$$i_{dc_eq} + i_{afe_eq} = (i_{DCDC} - i_{DCDC}) - \left(\frac{i_{ch}+i_{cl}}{2}\right) - \left(\frac{i_{ch_AFE}-i_{cl_AFE}}{2}\right) = (C_{eq} + C_{bus})\frac{du_{bus}}{dt} \qquad (19)$$

With:

$$i_{AFE_eq} = \frac{i_{hAFE}-i_{lAFE}}{2} = -i_{DC_AFE} - \left(\frac{i_{ch_AFE}+i_{cl_AFE}}{2}\right) \qquad (20)$$

If the currents on the AFE side are balanced, $i_{nafe}=0$, and thus:

$$i_{hafe} = -i_{afe} \qquad (21)$$

$$i_{lafe} = i_{afe} \qquad (22)$$

The storage capacitor and the equivalent capacitance of the voltage bridge are represented as storage elements. To couple them a monodomain distribution element is used. In EMR this association is depicted by a crossed orange rectangle and 2 overlapped orange squares (Figure 15).

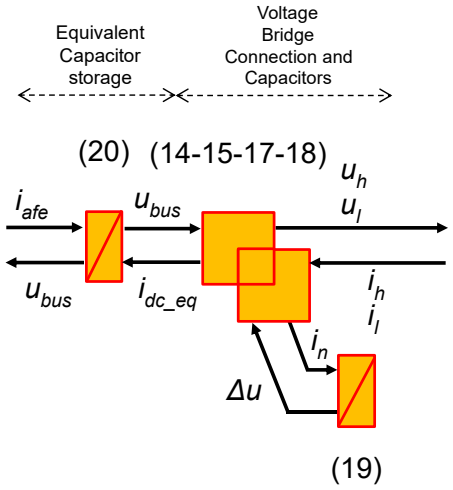


Figure 15: Charging capacitor and voltage bridge divider with EMR

II.2.c. NPC converter

The purpose of the converter is to deliver power accurately to the electromagnet. Positive and negative voltages are required to increase and decrease the current in the magnet. The polarity is also used to charge the floating capacitor by applying a negative voltage across a converter. Since the converter is a four quadrants power converter it is reversible in current (Figure 16). This occurs when, at the start and at the end of a cycle, the ripple of the current in the legs is high enough to reach negative values. The 6 legs allow the division of the current and multiply the output frequency by 6.

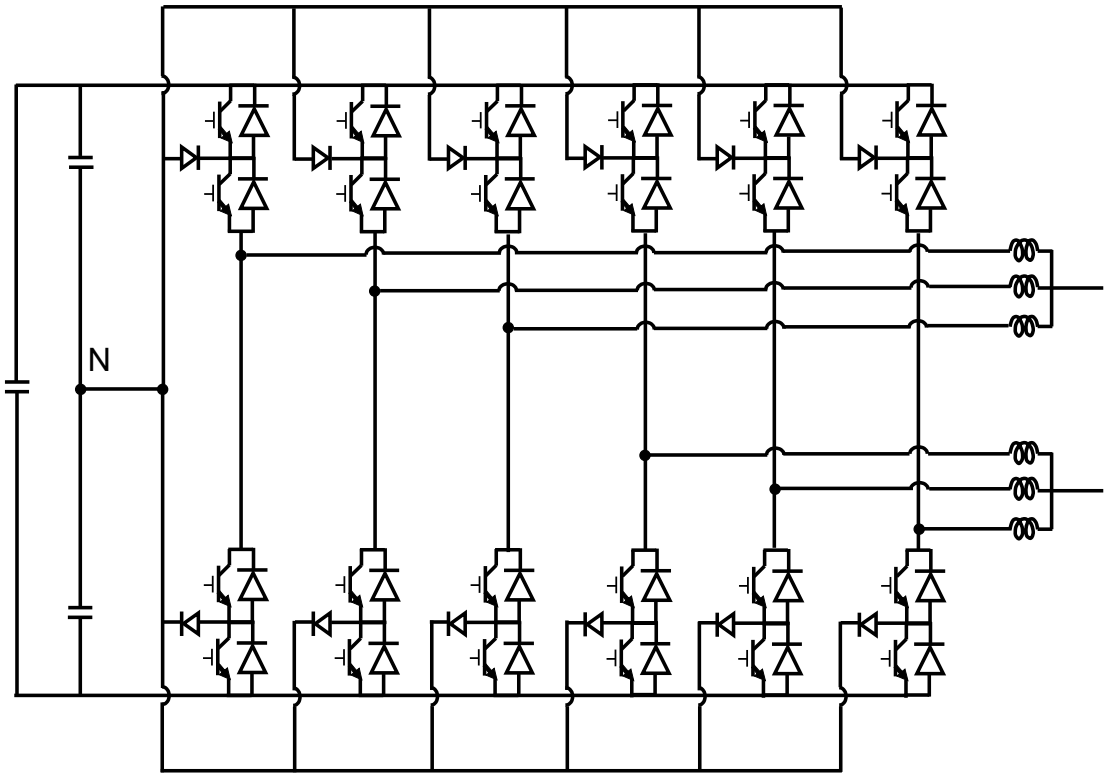


Figure 16 : DC/DC converter of POPS

The NPC converter is modelled using an equivalent circuit (Peng 2019) (Li 2020) (Figure 17). The f_{xy} functions are defined from the switching function s_{xy} (

Table 1) where x is the number of the NPC leg. The combination of the equivalent power switches is a commutation cell:

$$f_{x1} + f_{x2} + f_{x3} = 1 \qquad (23)$$

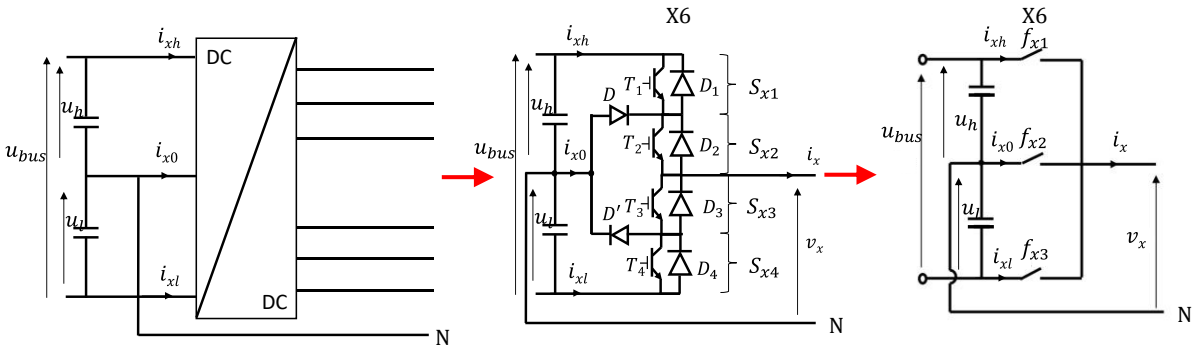


Figure 17: Equivalent electrical circuit for one leg of the DC/DC converter

The table describes the switching function obtained with the combination of switches that are ON or OFF and the output voltage and current of a leg in function of the corresponding switching functions.

Table 1: Voltage output in function of the switching function

S_{x1}	S_{x2}	S_{x3}	S_{x4}		f_{x1}	f_{x2}	f_{x3}		v_x		i_{xh}	i_{x0}	i_{xl}
1	1	0	0		1	0	0		u_h		i_x	0	0
0	1	1	0		0	1	0		0		0	i_x	0
0	0	1	1		0	0	1		$-u_l$		0	0	i_x

The modulated voltages and the modulated currents given by the NPC are:

$$\begin{cases} \begin{bmatrix} v_1 \\ v_2 \\ v_3 \\ v_4 \\ v_5 \\ v_6 \end{bmatrix} = \begin{bmatrix} f_{11} & -f_{13} \\ f_{21} & -f_{23} \\ f_{31} & -f_{33} \\ f_{41} & -f_{43} \\ f_{51} & -f_{53} \\ f_{61} & -f_{63} \end{bmatrix} \begin{bmatrix} u_h \\ u_l \end{bmatrix} \\ \begin{bmatrix} i_h \\ i_l \end{bmatrix} = \begin{bmatrix} f_{11} & f_{21} & f_{31} & f_{41} & f_{51} & f_{61} \\ f_{13} & f_{23} & f_{33} & f_{43} & f_{53} & f_{63} \end{bmatrix} \begin{bmatrix} i_1 \\ i_2 \\ i_3 \\ i_4 \\ i_5 \\ i_6 \end{bmatrix} \end{cases} \quad (24)$$

The NPC converter is represented as mono-domain element. In EMR this association is depicted by a crossed orange rectangle and 2 overlapped orange squares (Figure 18).

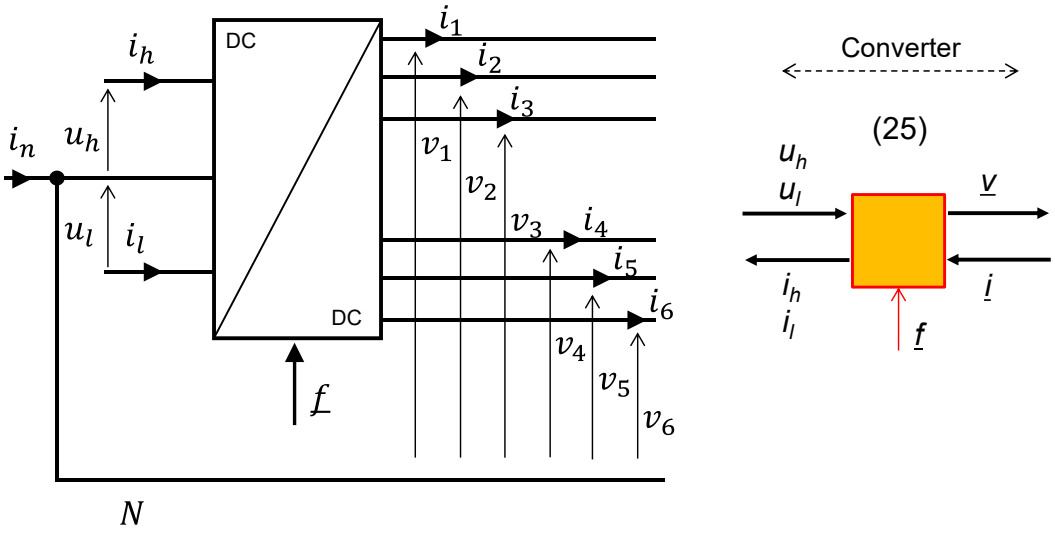


Figure 18: NPC converter equivalent scheme and EMR

II.2.d. Interleaved inductances

Using interleaved inductances reduces current ripple and helps keep the junction temperature of the power semiconductors lower, which improves their long-term reliability. Interleaving also offers advantages in terms of component size, thermal dissipation, and overall cost. To model the interleaved inductances, the neutral point N is considered (Figure 19).

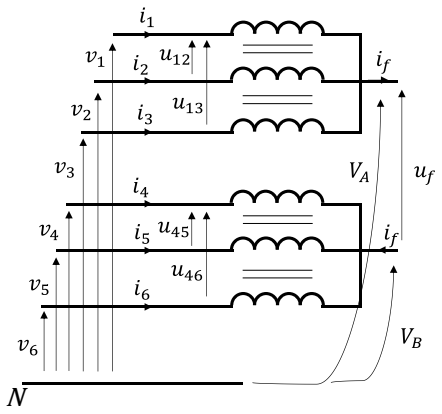


Figure 19: Interleaved inductances

The inductive filters are modelled considering the self-inductance L_x of the winding x and the mutual inductance M_{xy} between the winding x and y (Figure 20). The inductance current i_x is thus dependant on the modulated voltage v_x and the output voltages, V_A and V_B:

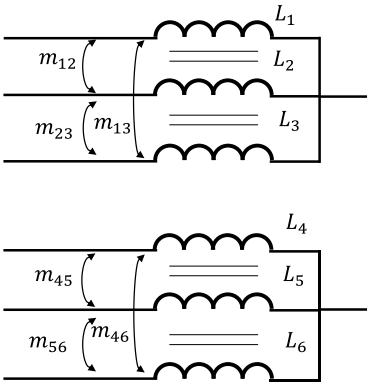


Figure 20: mutuals of the inductive filter

$$v_1 - V_A = L_1 \frac{di_1}{dt} + M_{12} \frac{di_2}{dt} + M_{13} \frac{di_3}{dt} + r\, i_1 \quad (25)$$

$$v_2 - V_A = M_{12} \frac{di_1}{dt} + L_2 \frac{di_2}{dt} + M_{23} \frac{di_3}{dt} + r\, i_2 \quad (26)$$

$$v_3 - V_A = M_{13} \frac{di_1}{dt} + M_{23} \frac{di_2}{dt} + L_3 \frac{di_3}{dt} + r\, i_3 \quad (27)$$

$$v_4 - V_B = L_4 \frac{di_4}{dt} + M_{45} \frac{di_5}{dt} + M_{46} \frac{di_6}{dt} + r\, i_4 \quad (28)$$

$$v_5 - V_B = M_{45} \frac{di_4}{dt} + L_5 \frac{di_5}{dt} + M_{56} \frac{di_6}{dt} + r\, i_5 \quad (29)$$

$$v_6 - V_B = M_{46} \frac{di_4}{dt} + M_{56} \frac{di_5}{dt} + L_6 \frac{di_6}{dt} + r\, i_6 \quad (30)$$

The total voltage u_f can be obtained:

$$V_A - V_B = u_f \quad (31)$$

Moreover, the filter current if is a combination of the currents in the inductances:

$$i_f = i_1 + i_2 + i_3 = -i_4 - i_5 - i_6 \quad (32)$$

For control design, one can consider $L_1=L_2=L_3=L_4=L_5=L_6=L$ and $M_{12}=M_{13}=M_{23}=M_{45}=M_{46}=M_{56}=M$ to be equal. A simulation has been realized to show the impact of their unbalance, and the robustness of the control. It has showed a few effects on the balancing of the currents.

$$\begin{bmatrix} v_1 \\ v_2 \\ v_3 \\ v_4 \\ v_5 \\ v_6 \end{bmatrix} - \begin{bmatrix} V_1 \\ V_2 \\ V_3 \\ V_4 \\ V_5 \\ V_6 \end{bmatrix} = \begin{bmatrix} L & M & M & 0 & 0 & 0 \\ M & L & M & 0 & 0 & 0 \\ M & M & L & 0 & 0 & 0 \\ 0 & 0 & 0 & L & M & M \\ 0 & 0 & 0 & M & L & M \\ 0 & 0 & 0 & M & M & L \end{bmatrix} \frac{d}{dt} \begin{bmatrix} i_1 \\ i_2 \\ i_3 \\ i_4 \\ i_5 \\ i_6 \end{bmatrix} + r \begin{bmatrix} i_1 \\ i_2 \\ i_3 \\ i_4 \\ i_5 \\ i_6 \end{bmatrix} \quad (33)$$

Considering the 1st 3 rows of (33) and replacing the currents with i_f using (32), a new differential equation is obtained:

$$v_1 + v_2 + v_3 - 3.V_A = (L + 2\,M)\frac{di_f}{dt} + r\,i_f \quad (34)$$

A second differential equation is obtained with the rest of the rows of (33) and using (32):

$$v_4 + v_5 + v_6 - 3.V_B = -(L + 2\,M)\frac{di_f}{dt} - r\,i_f \quad (35)$$

New equivalent voltages are defined:

$$V^+ = (v_1 + v_2 + v_3)/3 \quad (36)$$

$$V^- = (v_4 + v_5 + v_6)/3 \quad (37)$$

$$u = V^+ - V^- \quad (38)$$

V^+ and V^- are fictive voltages which are defined by adding the positive legs voltage together or by adding the negative legs voltage together of one converter.

$$v_1 + v_2 + v_3 - v_4 - v_5 - v_6 - 3u_f = 2(L + 2M)\frac{di_f}{dt} + 2ri_f \quad (39)$$

That can be rewritten using (36), (37), (38)

$$u - u_f = \frac{2}{3}(L + 2M)\frac{di_f}{dt} + \frac{2}{3}ri_f \quad (40)$$

We define the voltage across the interleaved inductance as:

$$u_{12} = v_1 - v_2 \quad (41)$$

$$u_{13} = v_1 - v_3 \quad (42)$$

$$u_{45} = v_4 - v_5 \quad (43)$$

$$u_{46} = v_4 - v_6 \quad (44)$$

We define the circulating currents in the interleaved inductance:

$$j_{12} = i_1 - i_2 \quad (45)$$

$$j_{13} = i_1 - i_3 \quad (46)$$

$$j_{45} = i_4 - i_5 \quad (47)$$

$$j_{46} = i_4 - i_6 \quad (48)$$

The control has to ensure that the circulating current has to be null in average value to ensure a correct repartition of the current i_f through the converter legs.

By regrouping the variables, the vector $\underline{j}$ is defined as:

$$\underline{j} = [j_{12}, j_{13}, j_{45}, j_{46}]^t \quad (49)$$

To model the differential inductances between each legs a low frequency R-L model is used with u the voltage across the differential inductances.

$$(L-M)\frac{d}{dt}\begin{bmatrix} j_{12} \\ j_{13} \\ j_{45} \\ j_{46} \end{bmatrix} + r\begin{bmatrix} j_{12} \\ j_{13} \\ j_{45} \\ j_{46} \end{bmatrix} = \begin{bmatrix} u_{12} \\ u_{13} \\ u_{45} \\ u_{46} \end{bmatrix} \quad (50)$$

The vector $\underline{u}$ can be defined:

$$\underline{u} = [u_{12}, u_{13}, u_{45}, u_{46}]^t \quad (51)$$

The inductance filter consists of 1 mono-domain coupling element and 2 energy accumulation elements. In EMR this association is depicted by 2 overlapped orange squares and 2 crossed orange rectangles (Figure 21).

The mono-domain element splits the $\underline{v}$ vector into 2 components, $\underline{u}$ and u. The component $\underline{u}$ correspond to the differential-mode inductance and is responsible for generating the circulating currents $\underline{j}$. The component u is used for the common-mode inductance, which represents the global inductance through which the current i_f flows.

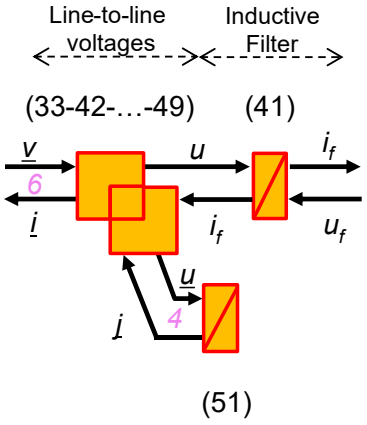


Figure 21: EMR of the interleaved inductances

II.2.e. Capacitive filter

The purpose of the capacitive filter is to filter the ripple of the voltage; 2 branches are used to have a 2nd order filter with low and high frequency filtering (Figure 22). The resistor acts as a damper.

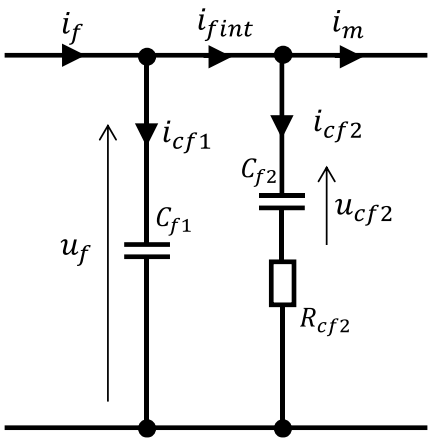


Figure 22: C/RC filter

The *C/RC* filter is composed of 2 branches in parallel, the first with a perfect capacitor C_{f1}. The second branch is composed of a capacitor C_{f2} in series with a resistor R_{Cf2}.The following equations describes the subsystem:

$$i_f - i_{fint} = C_{f1}\frac{du_f}{dt} \tag{52}$$

$$i_{fint} = i_{Cf2} + i_m \tag{53}$$

$$i_{Cf2} = C_{f2}\frac{du_{cf2}}{dt} + C_{f2}R_{cf2}\frac{d^2u_{cf2}}{dt^2} \tag{54}$$

The capacitive filter is represented with 2 accumulation elements, a mono-physical coupling element and a mono-physical converter. In EMR this association is depicted by a crossed orange rectangle and 2 overlapped orange squares and a single orange square (Figure 23).

The mono-physical coupling element and the mono-physical converter are introduced to resolve the association conflict between the 2 accumulation elements. Since both accumulation elements impose their own voltage, they cannot be directly connected.

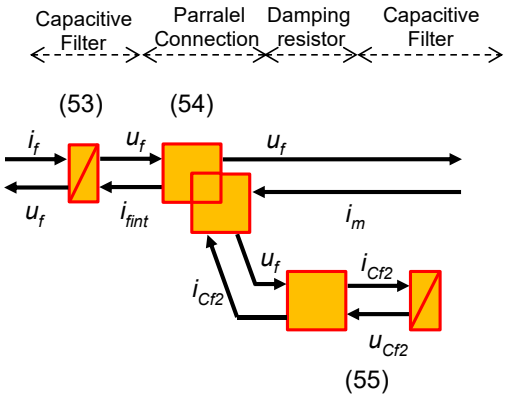


Figure 23: EMR of the C/RC filter

II.2.f. Electromagnet

The electromagnet is modelled using a 6th degree equation to match the behaviour of the saturation.

$$u_f - R_m i_m = \frac{d\phi_m}{dt} \quad (55)$$

$$i_m = \phi_m a_1 + \phi_m^2 a_2 + \phi_m^3 a_3 + \phi_m^4 a_4 + \phi_m^5 a_5 + \phi_m^6 a_6 \quad (56)$$

To obtain the magnetic flux from i_m another polynomial equation is used.

$$b_m = i_m b_1 + i_m^2 b_2 + i_m^3 b_3 + i_m^4 b_4 + i_m^5 b_5 + i_m^6 b_6 \quad (57)$$

The electromagnet is represented with an accumulation element and an estimation element. In EMR this association is depicted by a crossed orange rectangle and a purple square (Figure 24). The estimation element is required to obtain the magnetic field as the variable imposed by the electromagnet is the current.

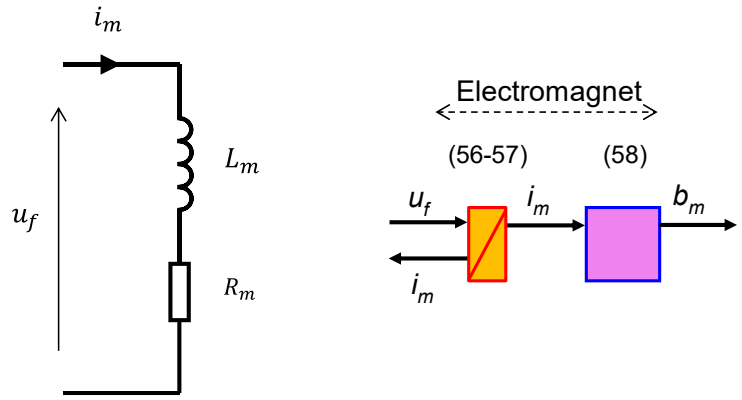


Figure 24: Electromagnet description

II.2.g. EMR of unitary converter

The EMR formalism allows the model to be organized according to the principle of interaction and causality. Moreover, by using EMR it is possible to deduce a systematic control organization based on the principle of inversion (Bouscayrol 2012). EMR is a graphical description that enables an easy interconnection of models from different subsystems. In EMR, 4 elements are required to describe the system (source element, conversion element, coupling element and energy accumulation element) (Annexe E). The grid and AFE are represented by an energy source element (green oval pictograms), the red arrow shows that the output can be controlled. This source imposes the output current i_{afe}. The behaviour of accumulation elements is described by differential equations. This concerns the charging storage capacitor (19), the voltage bridge divider (18), the filter inductance (40), the filter capacitors (52), (54) and the electromagnet (55). They are represented in EMR by accumulation elements (crossed orange rectangle). The NPC converter is a conversion element (orange square) with a modulation vector $\underline{f} = [f_{11}, f_{13}, f_{21}, f_{23}, f_{31}, f_{33}\, f_{41}, f_{43}, f_{51}, f_{53}, f_{61}, f_{63}]^t$. The tuning vector to impose the modulated voltage vector

$\underline{v}=[v_1, v_2, v_3, v_4, v_5, v_6]^t$. This vector leads to the inductance current vector $\underline{i}=[i_1, i_2, i_3, i_4, i_5, i_6]^t$ as a reaction. The decomposition of these currents in the filter and the circulation currents add a coupling element (overlapped orange squares). The equations must be rewritten in a casual way to express the output as a function of the input. For example (40) is rewritten as follows:

$$i_f = \frac{3}{2(L+2M)} \int \left(-\frac{2}{3} r i_f - u_f + V^+ - V^-\right) dt \qquad (58)$$

Using this principle, the EMR of the unitary converter is created (Figure 25).

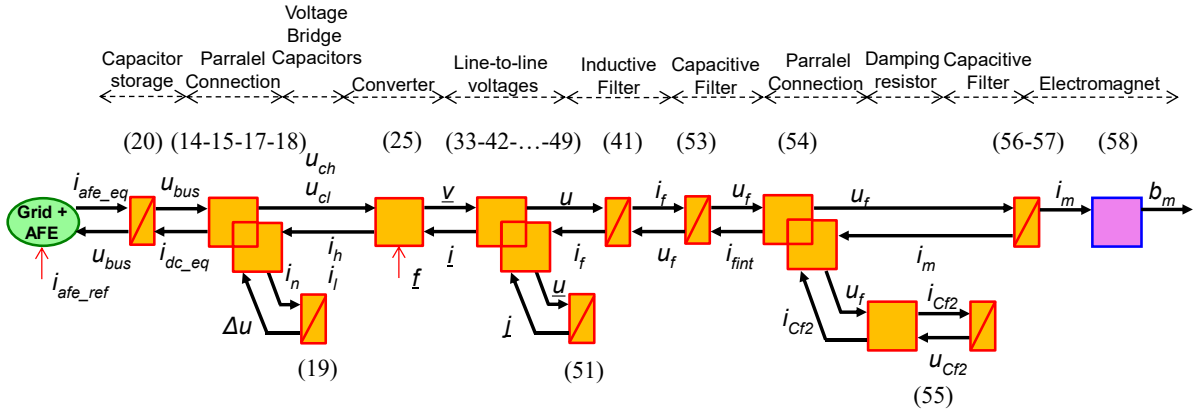


Figure 25: EMR of a unitary system

The state variables of the system are u_{bus}, Δu, $\underline{j}$, i_f, u_f and i_m.

II.3. Inversion-based control of the unitary converter

The analysis of the EMR allows the deduction of a control scheme using the inversion principle. A tuning path is first defined from the tuning vector $\underline{f}$ to the magnetic field b_m (Figure 26). A second tuning path is defined from the current reference of the AFE to supply the DC bus.

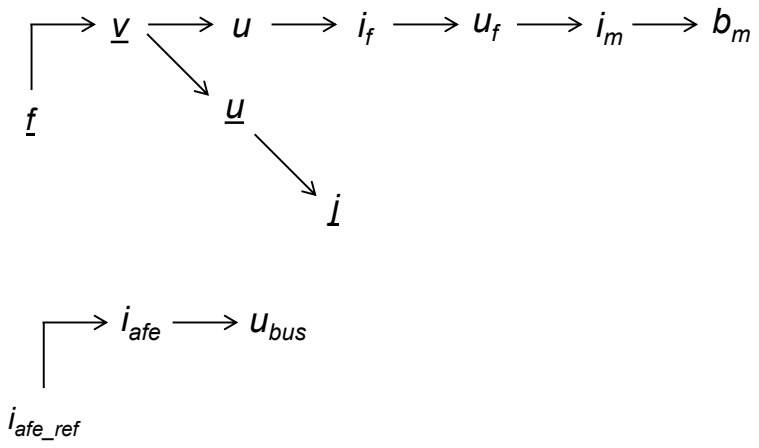


Figure 26: tuning paths of the unitary system

The only variable left to control is Δu, a strategy will be defined to control it via a degree of freedom.

The EMR elements are inverted along this tuning path. Accumulation elements are inverted using a closed-loop control, other elements are directly inverted.

II.3.a. Control of the electromagnet

The inversion of the magnet is done in 3 steps, 1st a direct inversion of the polynomial equation (57) to go from the magnetic field to the current then another inversion of (56) to go from the current to the flux. Then the inversion of (55), since it cannot be performed directly without the use of derivative relations. It is forbidden by the EMR formalism because of its non-causal aspect. Therefore, a controller (closed-loop) must be used to invert the relation between $flux_{_ref}$ and u_{f_ref}:

$$u_{f_ref} = C_1\left(b_{m_ref} - b_{m_meas}\right) \tag{59}$$

Here, $C_1(-)$ represents a controller, which can be proportional (P), proportional-integral (PI), or another type.

II.3.b. Control of the capacitive filters

The inversion of (52) requires an additional control loop for u_f and a compensation of i_{fint}, to define the reference i_{f_ref}:

$$i_{f_ref} = C_2\left(u_{f_ref} - u_{f_meas}\right) + i_{fint_meas} \tag{60}$$

The current i_{fint}, is obtained by measuring the current i_{Cf2} flowing through the capacitor C_{f2} and adding it to the current i_m.

$$i_{fint_meas} = i_{m_meas} + i_{Cf2_meas} \tag{61}$$

Here $C_2(-)$ denotes a voltage controller. The parallel capacitor C_{f2} is treated as a disturbance and is compensated by measuring the current flowing into it i_{cf2_meas}. This strategy simplifies the control structure by only requiring regulation of C_{f1}, thereby improving the performances.

II.3.c. Control of the inductive filter and the circulating currents

The inversion of (40) also requires a control loop of i_f and a compensation of u_f, to define the reference u_{ref}:

$$u_{ref} = C_3\left(i_{fref} - i_{fmeas}\right) + u_f \tag{62}$$

With $C_3(-)$ another controller. The inversions of (50) requires several control loops of j_{xy} to define the reference u_{xy_ref}:

$$\begin{bmatrix} u_{12_ref} \\ u_{13_ref} \\ u_{45_ref} \\ u_{46_ref} \end{bmatrix} = \begin{bmatrix} C_{12} & 0 & 0 & 0 \\ 0 & C_{13} & 0 & 0 \\ 0 & 0 & C_{45} & 0 \\ 0 & 0 & 0 & C_{46} \end{bmatrix} \left(\begin{bmatrix} j_{12_ref} \\ j_{13_ref} \\ j_{45_ref} \\ j_{46_ref} \end{bmatrix} - \begin{bmatrix} j_{12_meas} \\ j_{13_meas} \\ j_{45_meas} \\ j_{46_meas} \end{bmatrix} \right) \quad (63)$$

To minimise the circulating currents in the interleaved inductances, these currents must be driven to zero.

$$j_{12_ref} = 0 \quad (64)$$

$$j_{13_ref} = 0 \quad (65)$$

$$j_{45_ref} = 0 \quad (66)$$

$$j_{46_ref} = 0 \quad (67)$$

Since these currents are now decoupled from the filter current i_f, zero values can be imposed via controllers (63).

The inversion of (38) is a coupling inversion. Since 2 outputs must be deduced from a single input, a distribution input named k_{dv} must be deduced for the coupling. This input defines the sharing between the modules.

$$\begin{cases} V_{ref}^{+} = k_{dv} u_{fref} \\ V_{ref}^{-} = (k_{dv} - 1) u_{ref} \end{cases} \quad (68)$$

$with\ k_{dv} \in [0,1]$

II.3.d. Control of the voltage balance

The voltage of the capacitor bridge at the input of the DC/DC converter needs to be balanced. If not balanced, those voltages will diverge and cause an uneven voltage output or damage the components. To perform this balance, the variable k_{dv} is acted upon. As this variable has an impact on the output voltage of the positive legs and the negative legs. If the positive legs are more solicited the capacitor C_h will discharge, if the negative legs are more solicited the capacitor C_l will discharge.

The relation between i_n and k_{dv} can be found with (24) assuming the voltage is balanced.

$$u_h = u_l = \frac{u_{bus}}{2} \quad (69)$$

with (24) it can be demonstrated that the current flowing through the neutral point is:

$$i_n = (1 - |f_1|)\, i_1 + (1 - |f_2|)\, i_2 + (1 - |f_3|)\, i_3 + (1 - |f_4|)\, i_4 + (1 - |f_5|)\, i_5 + (1 - |f_6|)\, i_6 \quad (70)$$

This equation can be simplified knowing that the total sum of all the current of the legs is equal to 0.

$$i_n = -|f_1|\, i_1 - |f_2|\, i_2 - |f_3|\, i_3 - |f_4|\, i_4 - |f_5|\, i_5 - |f_6|\, i_6 \quad (71)$$

By making the assumption that the currents are balanced,

$$i_1 = i_2 = i_3 = -i_4 = -i_5 = -i_6 = i_f/3 \quad (72)$$

(71) can be factorized using (72),

$$i_n = -[(|f_1| + |f_2| + |f_3|) - (|f_4| + |f_5| + |f_6|)]\frac{i_f}{3} \quad (73)$$

Moreover, in steady state, the voltages of the legs are equal to the equivalent voltage defined earlier.

$$v_1 = v_2 = v_3 = V^+ \quad (74)$$

$$v_4 = v_5 = v_6 = V^- \quad (75)$$

So, by replacing the switching function by the voltages:

$$i_n = -\left[\left|\frac{V^+}{u_{bus}/2}\right| - \left|\frac{V^-}{u_{bus}/2}\right|\right] i_f \quad (76)$$

Using (38), V^- can be rewritten:

$$i_n = -\left(|V^+| - \left|\frac{u}{2}\right|\right)\frac{i_f}{u_{bus}/2} \quad (77)$$

The relation between equivalent voltage V^+ and V^- gives u is given in (38). When doing the inversion, a degree of freedom appears, it is named k_{dv}.

$$i_n = -\left(uk_{dv} - \frac{u}{2}\right)\frac{i_f}{u_{bus}/2} \quad (78)$$

u can be removed from the parenthesis to isolate k_{dv}

$$i_n = -\left(k_{dv} - \frac{1}{2}\right)\frac{ui_f}{u_{bus}/2} \quad (79)$$

To have $i_n = 0$, k_{dv} must be equal to 0.5.

The tuning of the imbalance between u_h and u_l is done as following:

$$i_n = C_{eq}\,\frac{d\Delta u}{dt} = -\left(k_{dv} - \frac{1}{2}\right)\frac{i_f u}{u_{bus}/2} \quad (80)$$

To control Δu at 0.5 a controller is placed on Δu impacting k_{dv}

$$k_{dv} = -\frac{u_{bus}/2}{i_f u} C_{\Delta u}\left(\Delta u_{ref} - \Delta u_{meas}\right) + \frac{1}{2} \quad (81)$$

The values u_{bus}, u and i_f are likely to change over time. However, to simplify the structure of the controller constant values are chosen. Furthermore, for our application u_{bus} and i_f are always positive. As the process (capacitor C_{eq}) is a pure integrator, a proportional controller, $C_{\Delta u}$, is selected.

The term $-\frac{u_{bus}/2}{ui_f}$ will be included in the gain of the controller. The limit the value of k_{dv} considering potential imbalances (for example 0.4 to 0.6).

II.3.e. Inversion of the six-legged converter

The leg voltage references can be computed with the equations (36), (41), (42) for the positive legs and with (37), (43), (44)for the negative legs.

$$\begin{bmatrix} v_{1ref} \\ v_{2ref} \\ v_{3ref} \\ v_{4ref} \\ v_{5ref} \\ v_{6ref} \end{bmatrix} = \begin{bmatrix} V^+ \\ V^+ \\ V^+ \\ V^- \\ V^- \\ V^- \end{bmatrix} + \begin{bmatrix} \frac{1}{3} & \frac{1}{3} & 0 & 0 \\ -\frac{2}{3} & \frac{1}{3} & 0 & 0 \\ \frac{1}{3} & -\frac{2}{3} & \frac{1}{3} & \frac{1}{3} \\ 0 & 0 & -\frac{2}{3} & \frac{1}{3} \\ 0 & 0 & \frac{1}{3} & -\frac{2}{3} \\ 0 & 0 & \frac{1}{3} & -\frac{2}{3} \end{bmatrix} \begin{bmatrix} u_{12ref} \\ u_{13ref} \\ u_{45ref} \\ u_{46ref} \end{bmatrix} \quad (82)$$

II.3.f. Inversion of the converter

The inversion of (24) is direct and lead to the reference of the modulation functions from the modulated voltage references. An effective balancing of the voltages u_l and u_h is considered hence:

$$u_h = u_l = \frac{u_{bus}}{2} \quad (83)$$

Therefore, f is defined in average values:

$$f_{1_ref} = \frac{2v_{1_ref}}{u_{bus_meas}} \quad (84)$$

$$f_{2_ref} = \frac{2v_{2_ref}}{u_{bus_meas}} \quad (85)$$

$$f_{3_ref} = \frac{2v_{3_ref}}{u_{bus_meas}} \quad (86)$$

$$f_{4_ref} = \frac{2v_{4_ref}}{u_{bus_meas}} \quad (87)$$

$$f_{5_ref} = \frac{2v_{5_ref}}{u_{bus_meas}} \quad (88)$$

$$f_{6_ref} = \frac{2v_{6_ref}}{u_{bus_meas}} \quad (89)$$

If $v_x \geq 0$ then $< f_{x1} >= \frac{2v_{x_ref}}{u_{bus_meas}}$ and $< f_{x3} >= 0$ (90)

If $v_x \leq 0$ then $< f_{x1} >= 0$ and $< f_{x3} >= \frac{2v_{x_ref}}{u_{bus_meas}}$ (91)

With x ∈ {1,2,3,4,5,6}

To go from the voltage references $\underline{v}$ to f_{xy} function, each voltage is divided by the voltage of the capacitor bridge, then to the resulting division 1 is added. The 2 references are compared to a triangular carrier signal going from 0 to 1 (Figure 27). The triangular signals are shifted by 60° for each modulated vector to ensure an output of 2000 Hz. Thus, when v_{x_ref} is above the positive triangle, f_{x1} is equal to 1, when v_{x_ref+1} is above the positive triangle, the output is equal to 0. When v_{x_ref} is under the negative triangular signal, f_{x1} is equal to 0, when v_{x_ref+1} is below the positive triangle, the output is equal to 1.

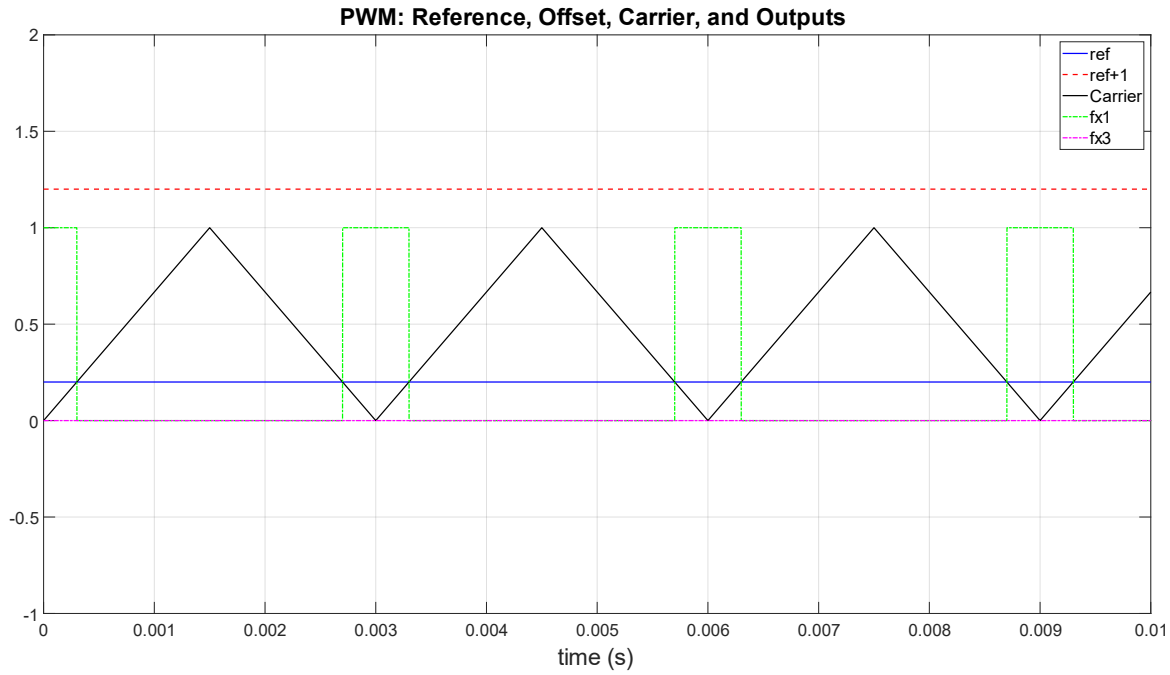


Figure 27: Creation of the PWM

II.3.g. Inversion of the storage capacitor

The control of the charging storage capacitor is managed by using two strategies. During the cycle, the AFE provides the joule losses of the magnet.

$$i_{afe_ref} = I_{m_meas}^2 R_m \quad (92)$$

At the end of the cycle to ensure the capacitor returns to its initial voltage of 5000 V, the strategy switch to a controller once the current in the magnet low enough.

$$i_{afe_ref} = C_4(u_{bus_ref} - u_{bus_meas}) \quad (93)$$

With those equations it is possible to build the inversion-based control structure (Figure 28) with blue parallelograms as control operations (crossed pictograms indicates a control loop).

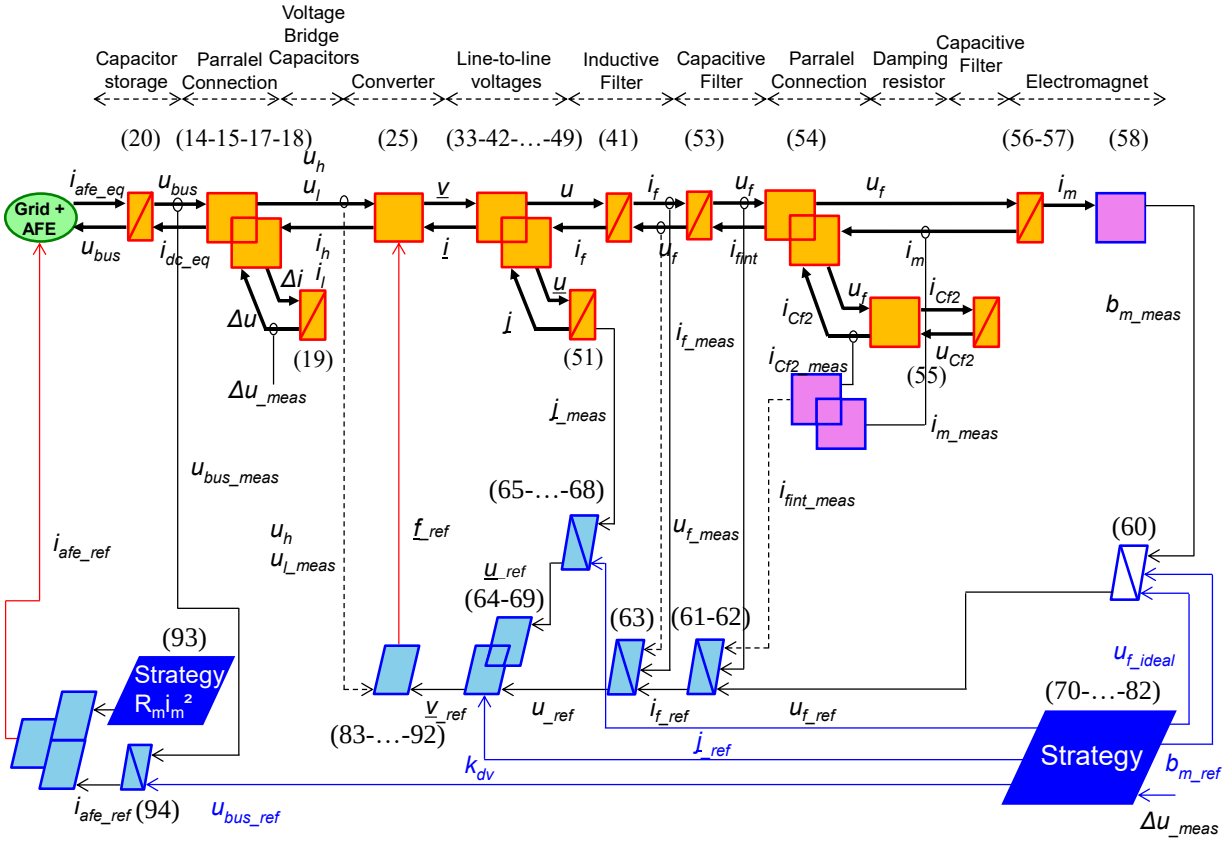


Figure 28: MCS of a unitary system

Three cascading control loops are in the system. Due to the high precision required, a flatness control is used for the magnet controller. Hence a blue and white crossed rectangle. The flatness control allows a faster response time as well as a decoupling of the loop (Lévine 2009). The principle of this flatness control is to apply the voltage which corresponds to the derivative of the reference magnetic field at the output of the magnet (59). It is possible to perform this technique since the desired reference is known beforehand, the computing of the derivative is done off-line. This work has been theorised by (Horrein 2017) and also applied in (Godart 2022).

The flatness control is performed by converting the magnetic flux density reference into the current and the flux through inversion of the polynomial equations (56) and (57):

$$\phi_{m_ideal} = b_{m_ref}c_1 + b_{m_ref}^2c_2 + b_{m_ref}^3c_3 + b_{m_ref}^4c_4 + b_{m_ref}^5c_5 + b_{m_ref}^6c_6 \quad (94)$$

$$i_{m_ideal} = b_{m_ref}d_1 + b_{m_ref}^2d_2 + b_{m_ref}^3d_3 + b_{m_ref}^4d_4 + b_{m_ref}^5d_5 + b_{m_ref}^6d_6 \quad (95)$$

By directly inverting (55) and combining it with (94) and (95), v_{m_ideal} can be obtained:

$$v_{m_ideal} = \frac{d\phi_{m_ideal}}{dt} + i_{m_ideal}R_m \quad (96)$$

Other non-linearities needs to be considered, such as the minimum-on time of the transistors and the dead times to avoid short circuits in the voltage bridge divider.

A minimum on-time is required to prevent tail current, as the IGBT cannot switch off instantly. Ensuring a minimum on-time guarantees proper operation. To model this behaviour, a minimum value is imposed on the modulation index *f*, named f_{min}, it is set to 0.01. To reduce the non-linearities this minimum value is divided by 2. If *f* is between $f_{min}/2$ and 0, the output *f'* is set to 0. If *f* is between $f_{min}/2$ and f_{min}, *f'* is equal to f_{min} (Figure 29) (Videt 2008).

This logic is mirrored for the negative values of *f*.

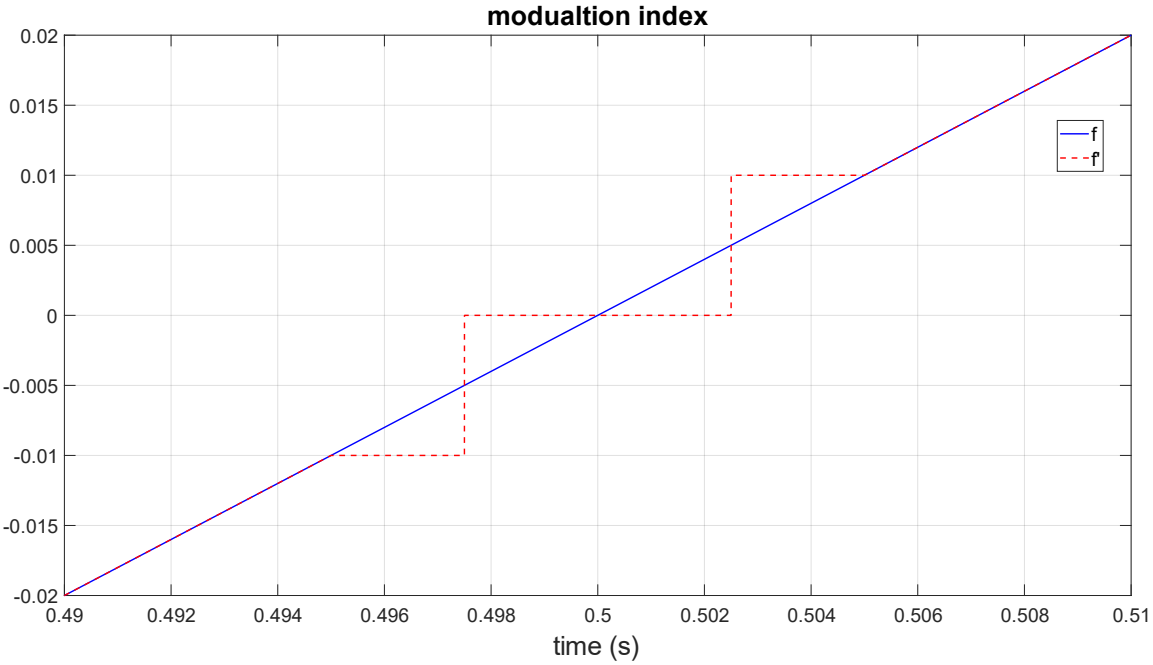


Figure 29: Evolution of the modulation index f and its processed output m' showing the minimum on-time effect.

To prevent shoot-through during switching transitions, a dead time of 20 µs is introduced between the turn-on and the turn-off of a transistor and its complementary device. This ensures that both devices are never conducting at the same time. The dead time is applied by delaying each gate signal by 20 µs, guaranteeing a safe operation. Because the dead time is a small fraction of the switching period, the output waveform and overall performance are minimally affected.

II.4. Control performances in simulation

The simulations are done with MATLAB-Simulink© using the EMR library (EMR website). A reference with a maximum peak of 2250 G is used. A step time of 1µs is chosen for the 1.1s simulation with an ode4 Runge-Kutta solver.

In the first part of the reference (Figure 30), the injection phase occurs, followed by the acceleration phase, and finally the extraction phase.

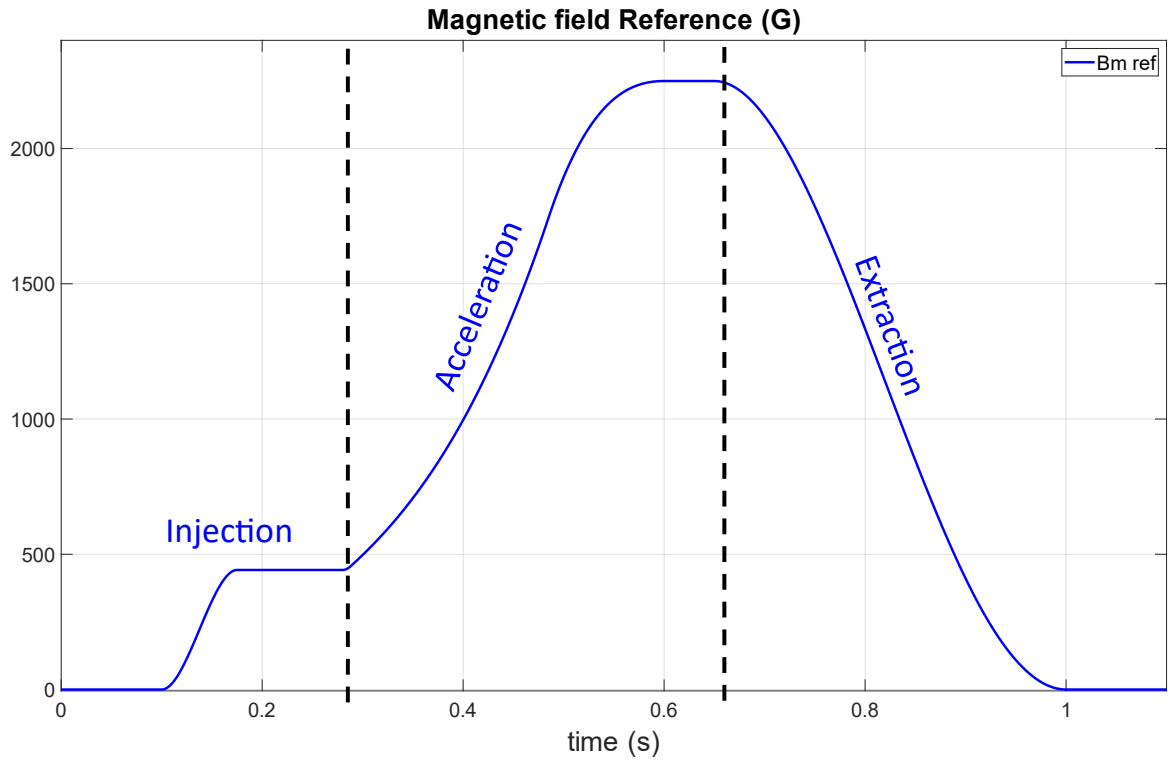


Figure 30: Magnetic field reference for a unitary converter

II.4.a. Control performances in average value

The converter is modelled in average value The sampling, the minimum ON time, the dead times and the discretization of the control are not taken into account. The indirect inversion uses analogue PI controllers with a damping factor of 1. The response time for the filter inductances is 1.5ms. The response time is 4.5ms for the filter capacitances (three times greater than the previous one to decouple both loops). And a time of 12.5ms for the magnet loop is chosen. The integrators are restarted at the start of each cycle.

The current i_f is similar to the magnetic field reference, it has bumps at the start, at the start of the ramp and in the middle the ramp, to break the voltage dynamics of u_f (Figure 31.a).

The voltage u_f at the output of the filter capacitance follows the derivative of the current reference (Figure 31.b).

The magnetic field b_m in the magnet follow the reference with a flat top of 2250 G (Figure 31.c).

The magnetic field error, defined as $(b_{m_ref} - b_{m_meas})$, almost satisfies the strict specification of maximum 100 ppm. The magnetic field is going slightly above the threshold during the high dynamic variation of the reference. This is noticeable at the beginning, the field overshoots by -1 G, then by 0.6 G at the start of the ramp, the last overshoot can be ignored since the cycle is finished, and the particle is not in the accelerator anymore. During the flat tops the magnetic field stays within the error margin (Figure 31.d). That is the main request.

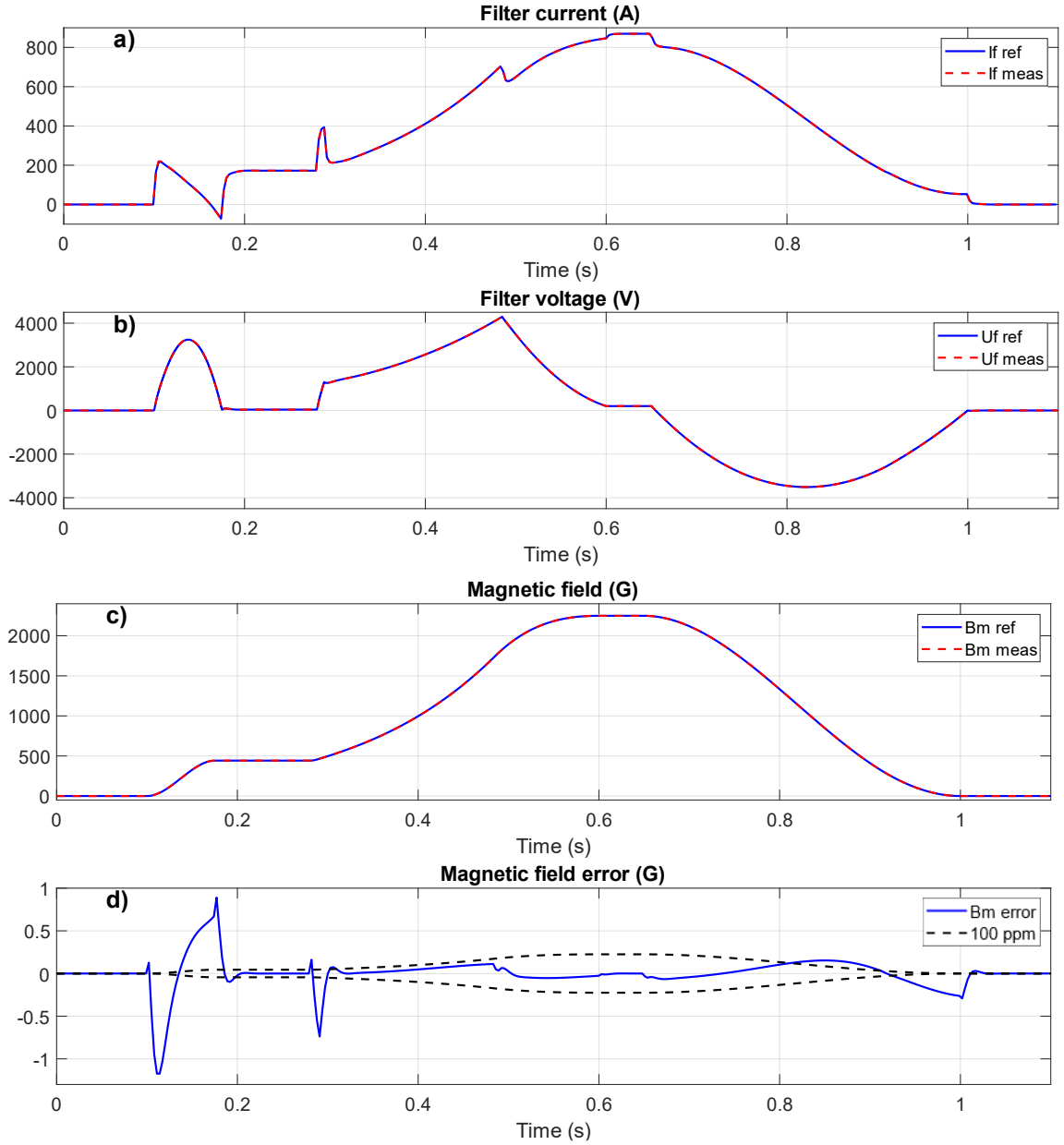


Figure 31: Simulation of the unitary system using inversion-based control a) current in the inductive filter, b) voltage of the capacitive filter, c) magnetic field, d) error of the magnetic field with limits of 100 ppm.

Since the simulation is in average value, the PWM is not present and not impacting the current i_1 to i_6 so they are the image of i_f divided by 3 (Figure 32.a). The PWM does not affect the leg currents, so they are not unbalanced therefore $\underline{j}$ is equal to 0 (Figure 32.b).

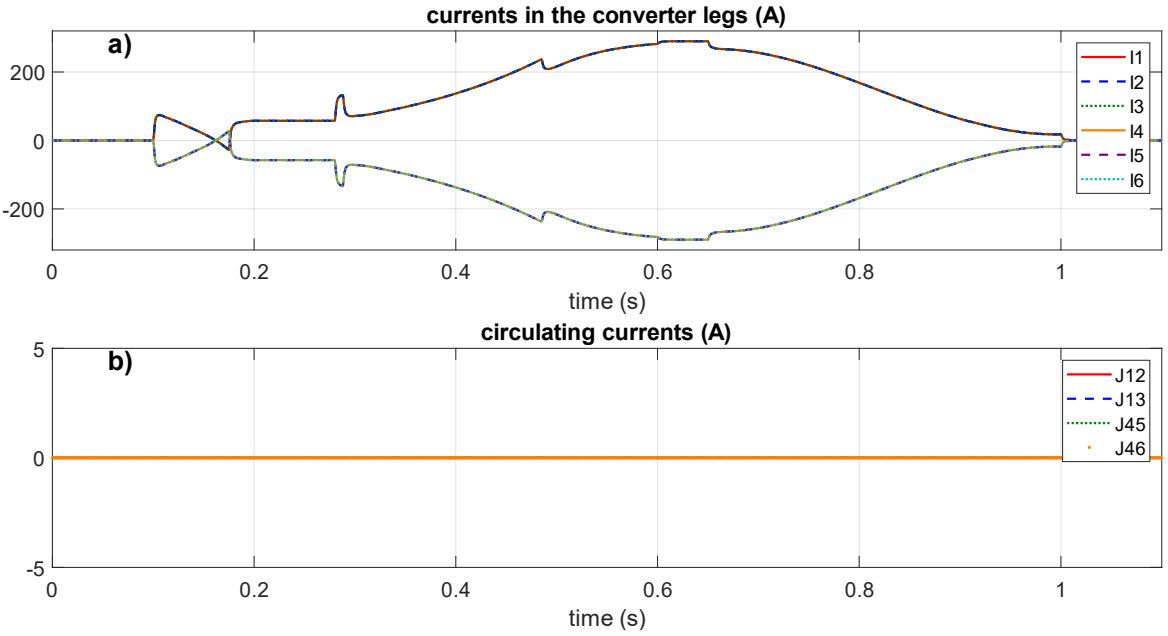


Figure 32: Simulation of inversion-based control a) current in the converter leg, b) 4 circulating currents j.

The voltage across C_h and C_l are not diverging, they stay at the same value. Their discharge is noticeable when the pulse starts, and their voltage go back to 2500V at the end of the cycle (Figure 33.a).

The voltage unbalance starts with a chosen unbalance of -1V. This unbalanced is overcome as soon as the current is flowing in the converter (Figure 33.b). No capacitor voltage imbalance appears in the average model, since the imbalance is introduced by the PWM switching, which unequally stresses the DC bus capacitors.

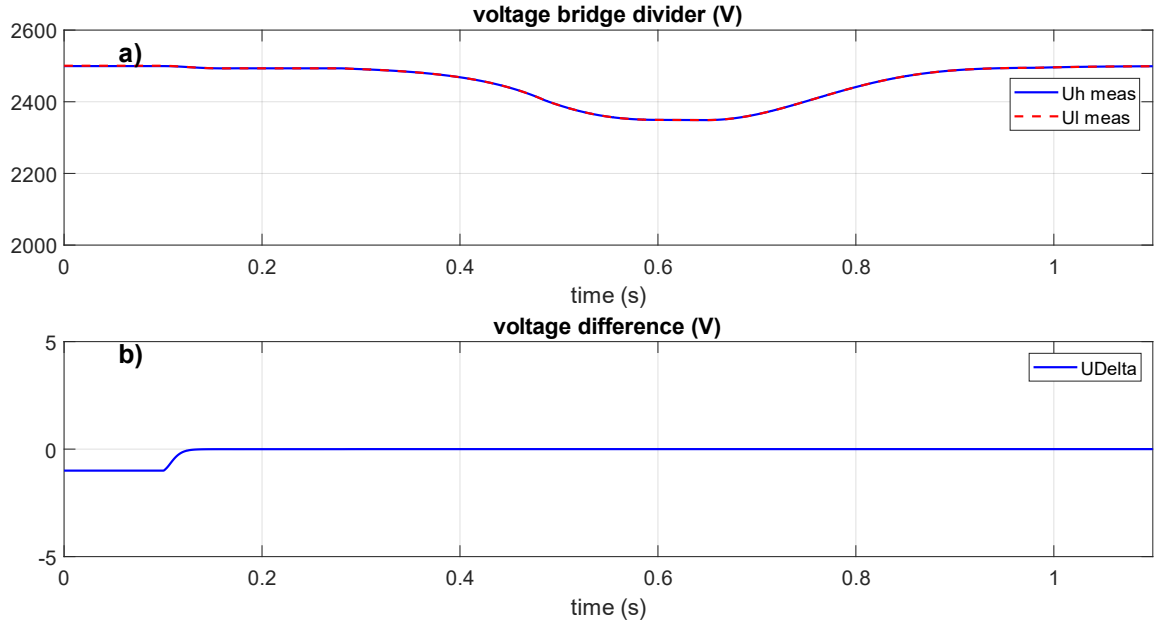


Figure 33: Simulation of inversion-based control a) voltages of the bridge divider, b) difference between u_h and u_l

The voltage u_{bus} of the charging storage capacitor changes with the current demand, when i_m ramps up, u_{bus} is discharging and when i_m is descending, u_{bus} is charging (Figure 34.a). At the end of the cycle u_{bus} is reaching 5000V and is ready for another cycle.

i_m is the current in the magnet it is like b_m, the current is too low to have a saturation effect. (Figure 34.b)

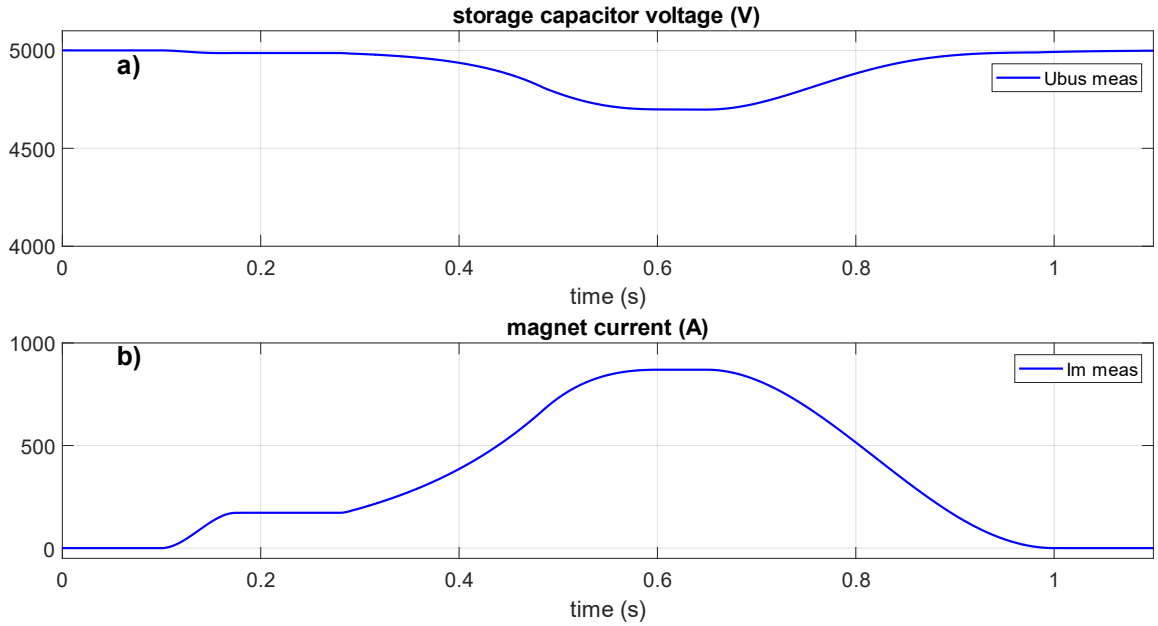


Figure 34: Simulation of inversion-based control a) u_{bus} voltage, b) current in the magnet

The simulation results in average value demonstrate that the inversion-based control applied to the unitary converter allows an accurate tracking of the magnetic field reference. The magnetic field follows

the required cycle with only small transient deviations during the most dynamic phases, while remaining within the specified ±100 ppm error during the flat-top period. Which satisfies the specification. The average value model also confirms the expected behaviour of the internal variables. The converter currents are stable, the capacitor voltages are stable and a proper energy exchange is done with the storage capacitor throughout the cycle. These results validate the effectiveness of the control strategy in simulation and provide a solid basis for further studies including switching effects and more detailed converter modelling.

II.4.b. Control performances in discrete value

When moving from the average model to the discrete model, system nonlinearities are explicitly included. These nonlinear effects come from the PWM, the 2 kHz sampling, the integrator going from the Laplace domain to the Z domain, the minimum on-time, and the dead times.

(Figure 35) shows the discrete results using inversion-based control. A 3-level PWM is used for the converter, with carrier signals of each leg shifted by 60°. The model uses discrete integrators with a sampling time of 12.5µs. The controller for the filter inductances has a response time of 2.5ms. The response time is 12.5ms for the filter capacitances, it is five times greater than the previous one for decoupling and accounts for the non-linearities inherent of the discrete model. And it is 62.5ms for the magnet controller. All integrators are initialized at the start of the cycle.

The current i_f is similar to the magnetic field reference, it has bumps at the start, middle and before the ramp, to break the voltage dynamics of u_f (Figure 35.a). A ripple of 2kHz is observed on the current due to the 3-level PWM and the shifting of each leg.

The voltage u_f at the output of the filter capacitance follows the derivative of the reference (Figure 35.b).

The magnetic field b_m in the magnet follow the reference with a flat top of 4170 G (Figure 35.c).

The magnetic field error, defined as ($b_{m_ref} - b_{m_meas}$), almost satisfies the strict specification of 100 ppm. The magnetic field is going slightly above the threshold during the high dynamic variation of the reference. This is noticeable at the beginning, the field overshoots by 1.2 G, then by -0.422 G when transitioning to the 2nd plateau and by 0.36 G before the ramp. During the flat top, the error stays within the threshold. The last overshoot can be ignored since the cycle is finished, and the particle is not in the accelerator anymore (Figure 35.d).

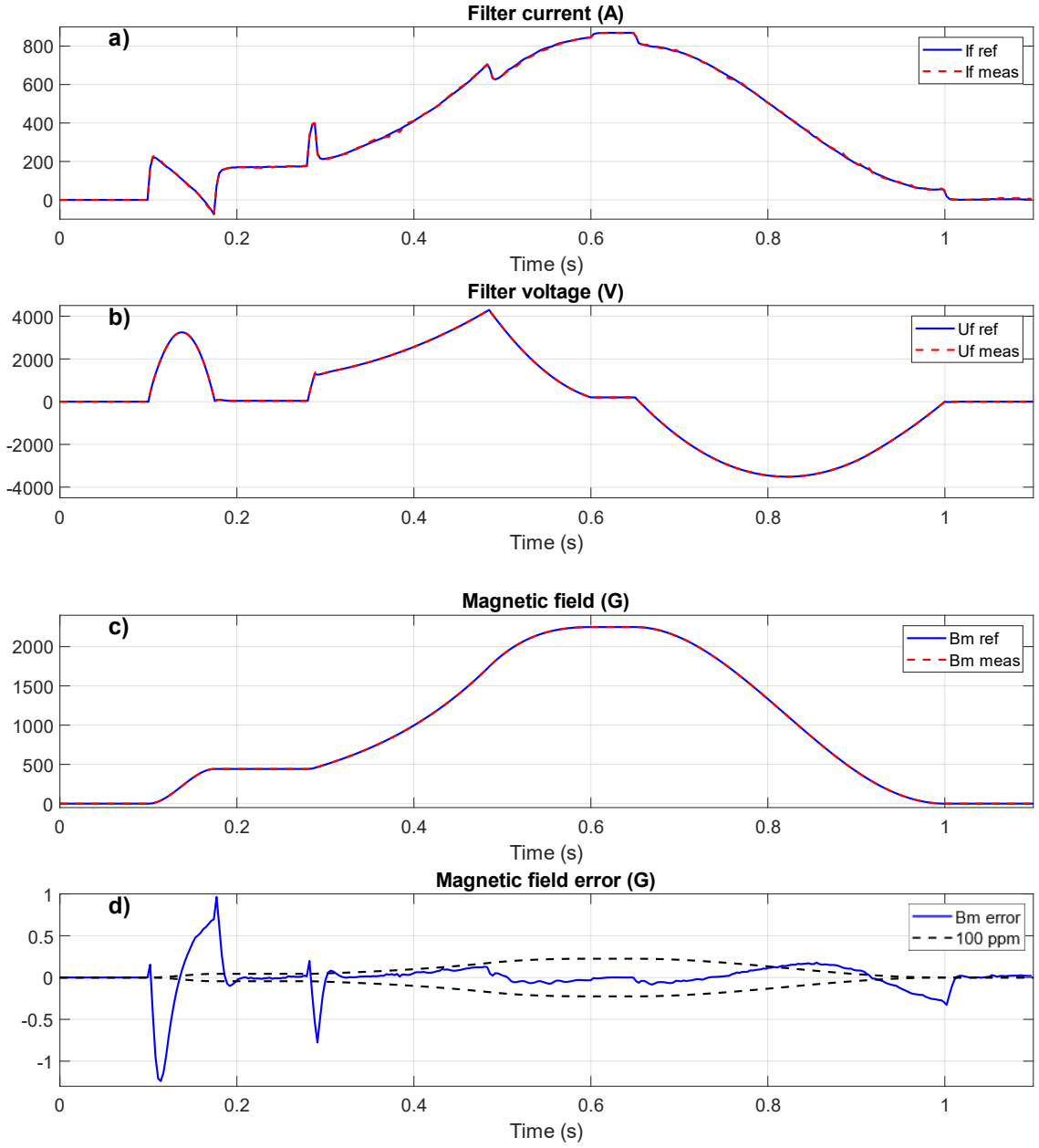


Figure 35: Discrete simulation of the unitary system using inversion-based control a) current in the inductive filter, b) voltage of the capacitive filter, c) magnetic field, d) error of the magnetic field

(Figure 36.a) shows the current i_1 to i_6. The effect of the PWM is noticeable, all currents have a ripple of 333 Hz, with a maximal amplitude of 180 A during the ramp. $\underline{j}$ are the circulating currents in the converter legs (Figure 36.b), the closer to 0 the more balanced the current. When the current is in steady state J is near 0. The main issues are during the high dynamics, there can be a difference of up to 72 A, it is due to the fact that the 1st leg is commuting and the 2nd comes after.

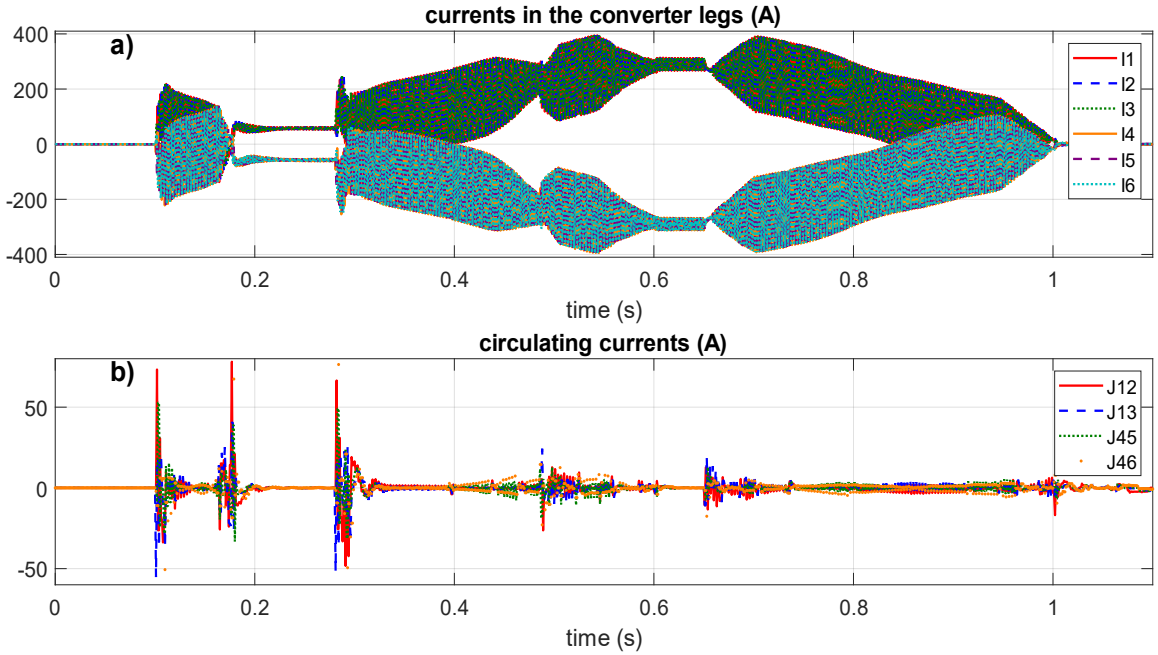


Figure 36 : Discrete simulation using inversion-based control a) current in the converter leg, b) 4 circulating currents j.

The voltages across C_h and C_l are stable and do not diverge, they remain at the same value. A discharge is noticeable when the pulse begins, after which their voltage returns to 2500 V at the end of the cycle (Figure 37.a).

The voltage imbalance starts with an initial offset of –1 V. This imbalance is corrected as soon as the current begins to flow in the converter (Figure 37.b). the maximal difference between the two voltages is 10V during the high dynamics, the voltage difference reaches 0 V at the end of a cycle.

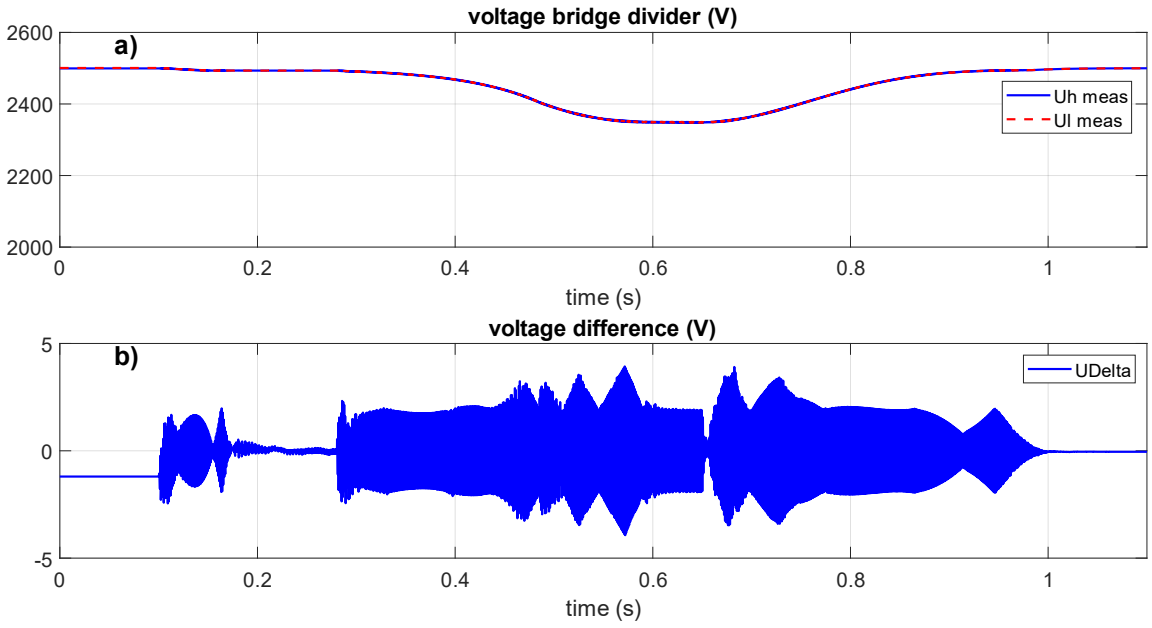


Figure 37: Discrete simulation a) voltages of the bridge divider, b) difference of voltage between u_h and u_l.

The voltage u_{bus} of the charging storage capacitor changes with the current demand, when i_m ramps up, u_{bus} is discharging and when i_m is descending, u_{bus} is charging (Figure 38.a). At the end of the cycle u_{bus} is reaching 5000 V and is ready for another cycle.

I_m is the current in the magnet it is like b_m, the current is too low to have a saturation effect. (Figure 38.b)

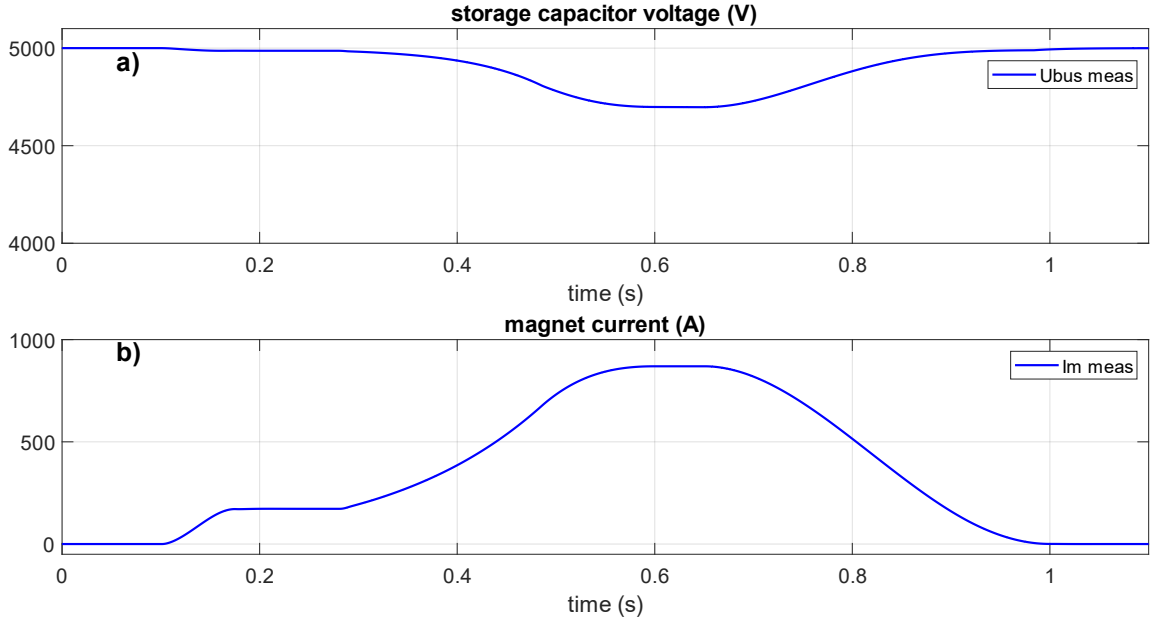


Figure 38: Discrete simulation using inversion-based control a) u_{bus} voltage, b) current in the magnet.

The discrete simulation confirms the robustness of the inversion-based control when non-linear constraints are considered. By moving from the average model to the discrete model, nonlinear effects such as PWM, sampling, minimum on-time, and dead times are included in the analysis. Despite these additional constraints, the system maintains stable and predictable behaviour throughout the cycle. The filter currents and voltages follow the expected dynamics, while the magnetic field closely tracks the reference profile, including the flat-top at 4170 G. Small overshoots appear during strong dynamic variations phases, but the magnetic field error remains within the 100 ppm specifications during the flat-top. In addition, the currents in the converter legs remain globally balanced, circulating currents stay limited and short in duration, the capacitor voltages remain stable without divergence, and the storage capacitor behaves as expected by discharging and recharging according to the magnet current demand. Overall, the results demonstrate that the proposed strategy remains effective under discrete and nonlinear operating conditions while maintaining the required performance and stability.

II.4.c. Conclusion of the unitary system results

This chapter presented the modelling and control of a unitary POPS converter using the EMR formalism. The system is progressively modelled from its electrical structure to a structured EMR, enabling the systematic design of an inversion-based control. The proposed control architecture ensures an accurate tracking of the magnetic field reference while maintaining internal stability, current sharing, and capacitor voltage balance. Simulation results in both average and discrete models demonstrate that the inversion-based control satisfies the required performance, validating the approach for further development of the complete POPS system composed of 6 unitary converters.

III. Inversion-based control of POPS

After the development of the inversion-based control of the unitary converter, an extension is proposed to the complete POPS composed of 6 unitary converters (Figure 41). However, some of these converters are not connected to the grid but to floating capacitors that increase the control complexity. Moreover, the series connection of the inductive filters adds some new constraints. The compete inversion-based control is progressively developed to face the new constraints. Finally, simulation results are provided to check the performances in terms of accuracy, energy flow and current balance.

III.1. EMR of POPS

The hypothesis made for the modelling are the same as for the unitary model. The grid and the AFEs are combined and considered as controlled current sources with a maximal power output of 2.5 MW. The losses for the inverters are ignored.

III.1.a. Capacitor storage, floating and capacitor divider

The charging storage capacitors follow the same modelling process as for the previous chapter:

$$i_{dc_eqx} + i_{afe_eqx} = \left(C_{eq} + C_{bus}\right)\frac{du_{busx}}{dt} \tag{97}$$

With the equivalent current coming from the AFE:

$$i_{afe_eqx} = \frac{-i_{hafeX}+i_{lafeX}}{2} \qquad with\ X\ \in \{1,2\} \tag{98}$$

With the equivalent capacitance of the converter voltage bridge:

$$i_{nx} = C_{eq}\frac{d\Delta_{ux}}{dt} \tag{99}$$

The storage capacitor and the equivalent capacitance of the voltage bridge are represented as storage elements. To couple them a monodomain coupling element is used. In EMR this association is depicted by a crossed orange rectangle (Figure 39).

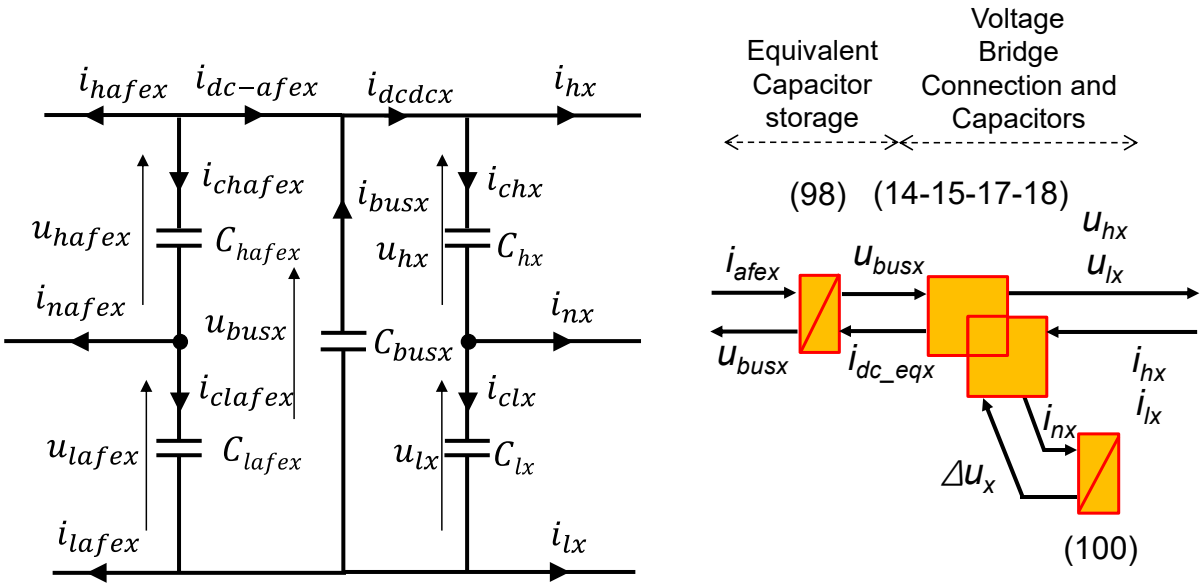


Figure 39: Charging capacitor and voltage bridge divider with EMR

To model the floating storage capacitor (Figure 40), equivalent currents coming from the converter needs to be defined, as the capacitors of the bridge have an impact on the storage capacitor.

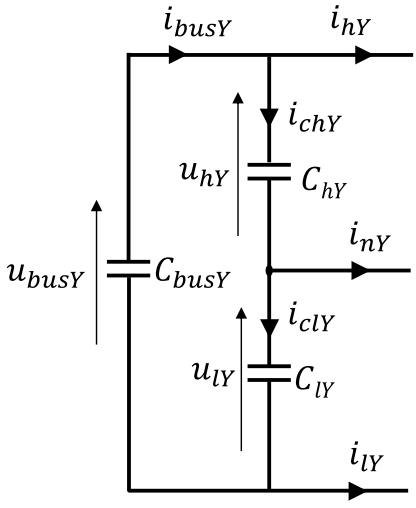


Figure 40: Electrical schematic of a floating capacitor and its voltage bridge divider at the input of a DC/DC

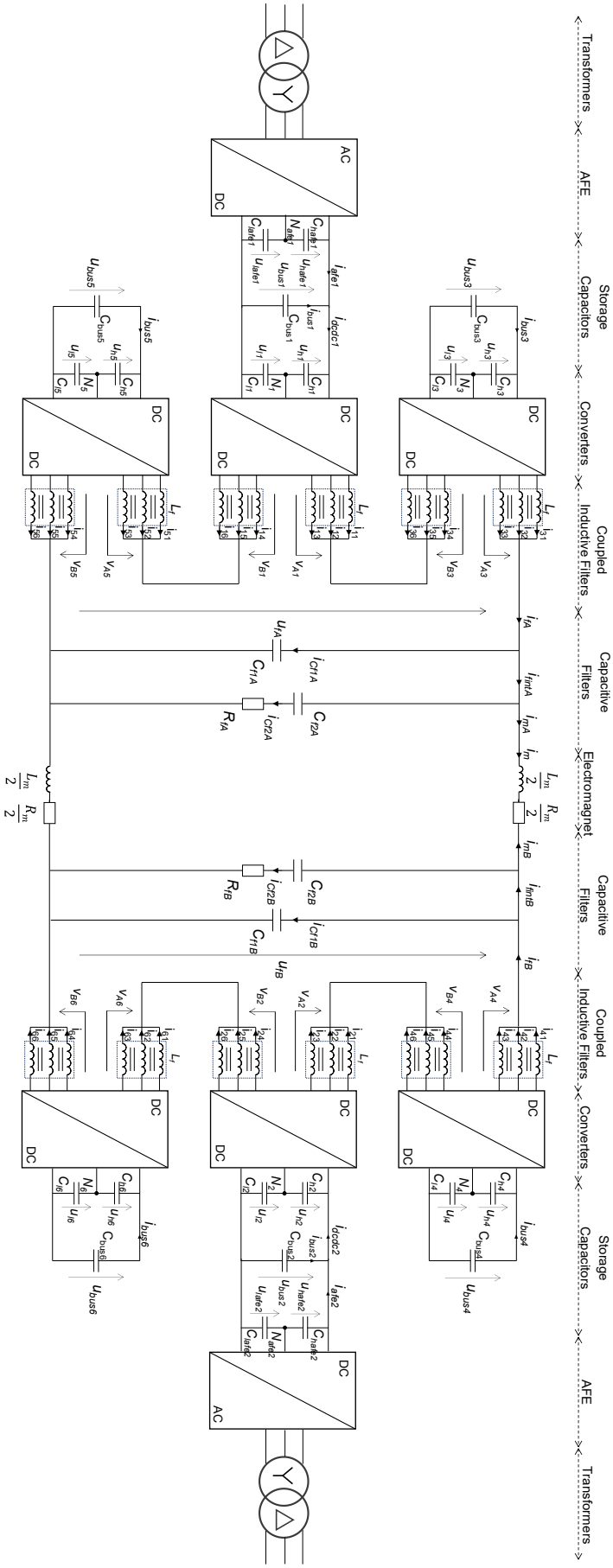


Figure 41: Electrical scheme of POPS

The modelling of these parallel connections with the floating storage capacitor gives as follows.

The bus voltage is equally distributed:

$$u_{busY} = u_{hY} + u_{lY} \tag{100}$$

By assumption the voltage bridge capacitance has the same values:

$$C_{eq} = C_{hY} = C_{lY} \tag{101}$$

The dynamical equation of each capacitor can be derived:

$$-i_{busY} = C_{busY} \frac{du_{busY}}{dt} \tag{102}$$

$$i_{chY} = C_{eq} \frac{du_{hY}}{dt} \tag{103}$$

$$i_{clY} = C_{eq} \frac{du_{lY}}{dt} \tag{104}$$

Using Kirchhoff's law, the currents flowing into the bridge capacitors are defined:

$$i_{chY} = i_{busY} - i_{hY} \tag{105}$$

$$i_{clY} = i_{busY} + i_{lY} \tag{106}$$

The voltage difference is defined as:

$$\Delta u_Y = u_{hY} - u_{lY} \tag{107}$$

By combining (100) with (107) leads to:

$$u_{hY} = \frac{u_{busY} + \Delta u_Y}{2} \tag{108}$$

$$u_{lY} = \frac{u_{busY} - \Delta u_Y}{2} \tag{109}$$

The control has to ensure a balance such as:

$$u_{hy} = u_{ly} = \frac{u_{busy}}{2} \tag{110}$$

$$i_{dc_eqY} = \frac{i_{hY} - i_{lY}}{2} \tag{111}$$

$$i_{nY} = i_{hY} - i_{lY} \tag{112}$$

The equivalent capacitance of the converter voltage bridge gives:

$$i_{nY} = C_{eq} \frac{d\Delta u_Y}{dt} \tag{113}$$

The equivalent storage capacitance leads to:

$$i_{dc_eqY} = \left(\frac{C_{eq}}{2} + C_{busY}\right) \frac{du_{busY}}{dt} \qquad with\ Y \in \{3,4,5,6\} \tag{114}$$

The floating capacitor and the equivalent capacitance of the voltage bridge are represented as storage elements. To couple them a monodomain distribution element is used. In EMR this association is depicted by 2 overlapped orange squares (Figure 42).

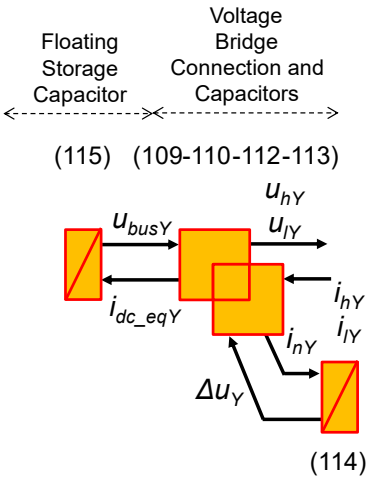


Figure 42: EMR of a floating capacitor

III.1.b. NPC converter

The NPC converter is modelled in the same way as for the previous chapter.

III.1.c. Interleaved inductances.

The use of interleaved inductances reduces current ripple and helps limiting the junction temperature of the power semiconductors, which improves their long-term reliability. Interleaving also offers advantages in terms of component size, thermal dissipation, and overall cost.

As the 3 DC/DC converters are connected in series, the common inductance is higher than a single converter (Figure 43). To model the interleaved inductances, the neutral points (N_1, N_2, N_3, N_4, N_5, N_6) of each converter are considered.

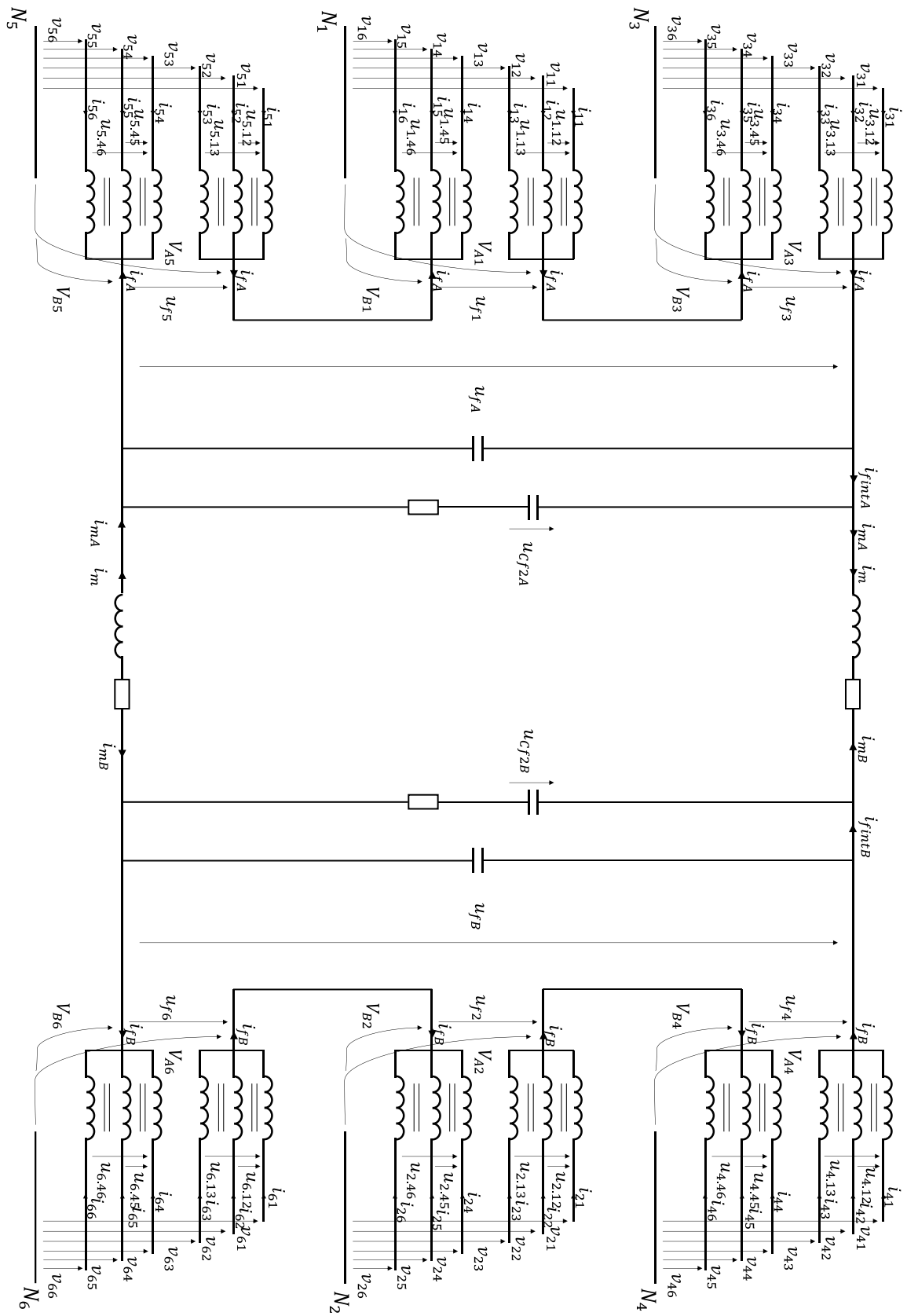


Figure 43: The inductive filter and mutuals inductances of POPS

The inductive filters are modelled by combining the self-inductance L and the mutual inductance M. The inductance current i_{Zx} is thus dependant on the modulated voltage v_{Zx} and the output voltages, V_{AZ} and V_{BZ}:

$$\begin{bmatrix} v_{Z1} \\ v_{Z2} \\ v_{Z3} \\ v_{Z4} \\ v_{Z5} \\ v_{Z6} \end{bmatrix} - \begin{bmatrix} V_{AZ} \\ V_{AZ} \\ V_{AZ} \\ V_{BZ} \\ V_{BZ} \\ V_{BZ} \end{bmatrix} \begin{bmatrix} L & M & M & 0 & 0 & 0 \\ M & L & M & 0 & 0 & 0 \\ M & M & L & 0 & 0 & 0 \\ 0 & 0 & 0 & L & M & M \\ 0 & 0 & 0 & M & L & M \\ 0 & 0 & 0 & M & M & L \end{bmatrix} \frac{d}{dt} \begin{bmatrix} i_{Z1} \\ i_{Z2} \\ i_{Z3} \\ i_{Z4} \\ i_{Z5} \\ i_{Z6} \end{bmatrix} + r \begin{bmatrix} i_{Z1} \\ i_{Z2} \\ i_{Z3} \\ i_{Z4} \\ i_{Z5} \\ i_{Z6} \end{bmatrix} \quad with\ Z \in \{1,2,3,4,5,6\} \tag{115}$$

The output voltage of a single converter can be written as:

$$u_{fZ} = V_{AZ} - V_{BZ} \tag{116}$$

The total output voltage of 3 series converter of the 2 sets gives:

$$u_{fA} = u_{f1} + u_{f3} + u_{f5} \tag{117}$$

$$u_{fB} = u_{f2} + u_{f4} + u_{f6} \tag{118}$$

Moreover, the filter current i_{fA} and i_{fB} are a combination of the currents in the inductances:

$$\begin{aligned} i_{fA} &= i_{11} + i_{12} + i_{13} = -i_{14} - i_{15} - i_{16} = i_{31} + i_{32} + i_{33} = -i_{34} - i_{35} - i_{36} \\ &= i_{51} + i_{52} + i_{53} = -i_{54} - i_{55} - i_{56} \end{aligned} \tag{119}$$

$$\begin{aligned} i_{fB} &= i_{21} + i_{22} + i_{23} = -i_{24} - i_{25} - i_{26} = i_{41} + i_{42} + i_{43} = -i_{44} - i_{45} - i_{46} \\ &= i_{61} + i_{62} + i_{63} = -i_{64} - i_{65} - i_{66} \end{aligned} \tag{120}$$

For simplification, one can consider $L_{Z1}=L_{Z2}=L_{Z3}=L_{Z4}=L_{Z5}=L_{Z6}=L$ and $M_{Z.12}=M_{Z.13}=M_{Z.23}=M_{Z.45}=M_{Z.46}=M_{Z.56}=M$. Considering the 1st 3 rows of (115) and replacing the current with if_X using (119), a new differential equation is obtained:

$$v_{Z1} + v_{Z2} + v_{Z3} - 3V_{AZ} = (L + 2\,M)\frac{di_{fZ}}{dt} + r\,i_{fZ} \tag{121}$$

A second differential equation is obtained with the rest of the rows of (115) and using (119):

$$v_{Z4} + v_{Z5} + v_{Z6} - 3V_{BZ} = -(L + 2\,M)\frac{di_{fZ}}{dt} - r\,i_{fZ} \tag{122}$$

V_Z^+ and V_Z^- are fictive voltages which are made by adding the positive legs voltage together or by adding the negative legs voltage together of one converter.

$$V_Z^+ = (v_{Z1} + v_{Z2} + v_{Z3})/3 \tag{123}$$

$$V_Z^- = (v_{Z4} + v_{Z5} + v_{Z6})/3 \tag{124}$$

$$u_z = V_Z^+ - V_Z^- \tag{125}$$

It is possible to sum those fictive voltages between modules:

$$V_A^+ = V_1^+ + V_3^+ + V_5^+ \quad (126)$$

$$V_A^- = V_1^- + V_3^- + V_5^- \quad (127)$$

$$V_B^+ = V_2^+ + V_4^+ + V_6^+ \quad (128)$$

$$V_B^- = V_2^- + V_4^- + V_6^- \quad (129)$$

$$u_A = V_A^+ - V_A^- \quad (130)$$

$$u_B = V_B^+ - V_B^- \quad (131)$$

The sum of those voltages corresponds to a series connection between the 3 modules.

By subtracting (121) by (122) for a set of 3 converters and using (119), (117),(126), (127) and (130) the total common mode inductance can be written:

$$u_A - u_{fA} = 6\frac{(L+2\,M)}{3}\frac{di_{fA}}{dt} + \frac{6\,r}{3}i_{fA} \quad (132)$$

$$u_B - u_{fB} = 6\frac{(L+2\,M)}{3}\frac{di_{fB}}{dt} + \frac{6\,r}{3}i_{fB} \quad (133)$$

As the circulating currents in the interleaved inductance are independent of the common mode the same equations of the previous model can be conserved here.

Putting the converters in series connection allows to have a higher voltage across the magnet.

III.1.d. Capacitive filters

The capacitive filters are modelled in the same way as for the previous chapter.

III.1.e. A and B series connection

A series connection is connecting the 2 sets of modules to the electromagnet. the series connection between the 2 sets of modules gives:

$$u_m = u_{fA} - u_{fB} \quad (134)$$

And the current:

$$i_m = i_{mA} = -i_{mB} \quad (135)$$

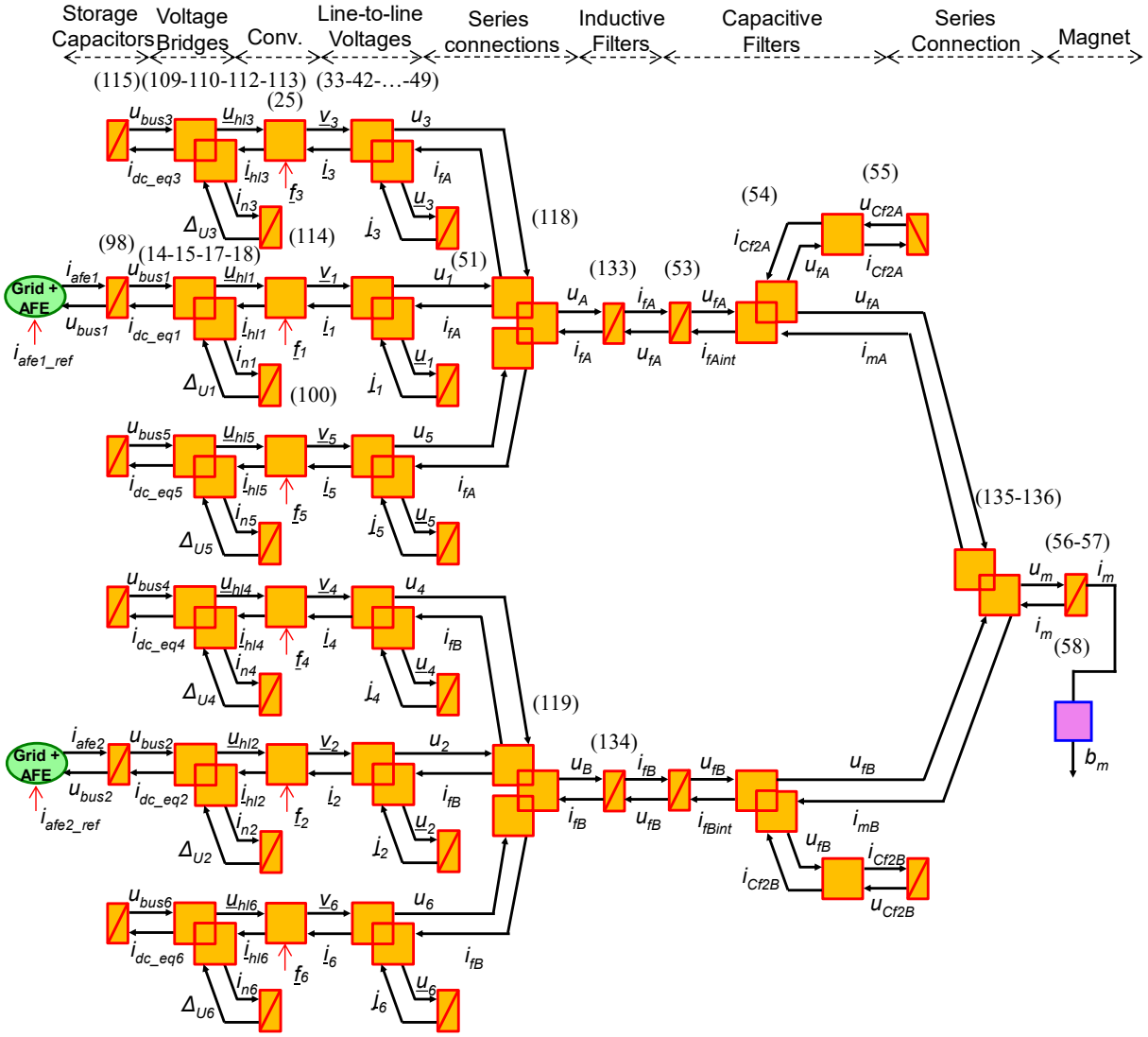
III.1.f. Electromagnet

The model of the magnet and its saturation take the same model as for the previous chapter.

III.1.g. EMR of POPS

The EMR formalism allows the model to be organized according to the principle of interaction and causality (

Figure *44*). Moreover, by using EMR it is possible to deduce a systematic control organization based



on the principle of inversion (Bouscayrol 2012).

Figure 44: EMR of POPS

The 43 state variables of the system are:

- the 6 storage capacitor voltages,

- the 3 inductor currents including the one of the magnets,

- the 4 capacitor filter voltages,

- the 6 voltages balance of the bridge ΔV,

- the 24 circulating currents in the interleaved coils.

III.2. Inversion-based control of POPS

The analysis of the EMR allows the deduction of a control scheme using the inversion principle. A tuning path is first defined from the tuning vectors $\underline{f}$ to the magnetic field b_m (Figure 45). Two additional tuning paths are defined from the current references of the AFEs to supply the 2 charging DC buses.

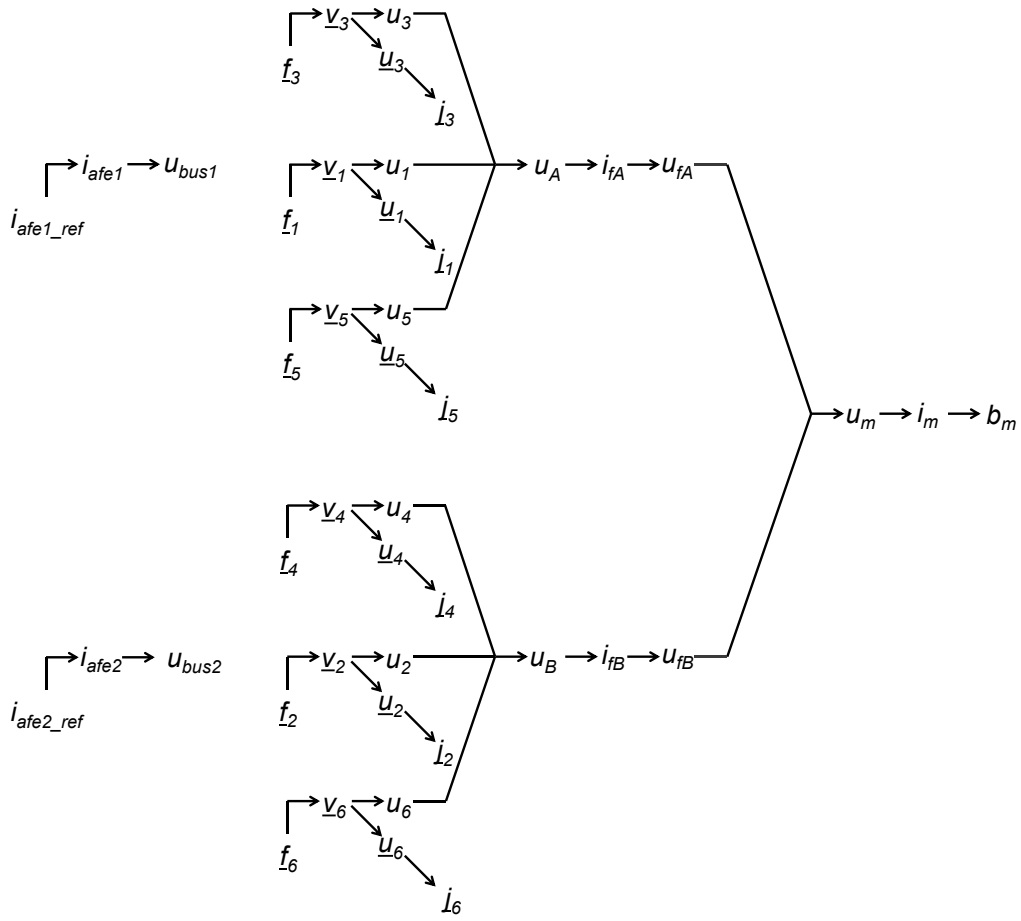


Figure 45: Tuning paths of POPS

The variables left to control are Δu_1, Δu_2, Δu_3, Δu_4, Δu_5, Δu_6. The same strategy as the proposed one in Chapter II is applied to control them via distribution inputs.

The circulation currents named $\underline{j}$ are set to 0.

The EMR elements are inverted along this tuning path. Accumulation elements are inverted using a closed-loop control, other elements are directly inverted.

III.2.a. Control of the electromagnets

The magnet uses the same control as for the previous chapter (cf. explained in (59)).

III.2.b. Control of the series connection between the 2 sets

The inversion of the 2 sets gives:

$$\begin{cases} u_{fA_ref} = u_{m_ref} k_{duAB} \\ u_{fB_ref} = -u_{m_ref}(1 - k_{duAB}) \end{cases} \qquad k_{duAB} \in [0,1] \tag{136}$$

k_{duAB} is a variable used to divide the voltage between the two sets of modules. In the nominal case, it is set to 0.5 so that the power is shared evenly.

III.2.c. Control of the capacitive filters

The capacitive filters use the same control as the previous chapter (cf. (60) and (61)).

III.2.d. Control of the inductive filters and the circulating currents

The inversion of the common mode inductance gives:

$$u_{refz} = C_3\left(i_{frefz} - i_{fmeasz}\right) + u_{fz_meas} \qquad with\ Z \in \{A, B\} \tag{137}$$

The voltage is then split between the 3 modules:

$$\begin{cases} u_{1_ref} = u_{_ref} k_{dv12} \\ u_{2_ref} = u_{_ref} k_{dv34} \\ u_{3_ref} = u_{_ref}(1 - k_{dv12} - k_{dv34}) \end{cases} \qquad with\ k_{dv12}\ and\ k_{dv34} \in \{-1; 1\} \tag{138}$$

The inversion of the series connection between the 3 converters introduces 2 degrees of freedom named k_{dv12} and k_{dv34}. Their value is defined in the next section.

The differential mode inductances, the current balance and the voltage balance is done in the same way as for the previous chapter. The circulating currents $\underline{j}$ are set to 0 to balance the leg currents.

III.2.e. Control of the converter

The converters are modelled the same way as the previous chapter.

With those equations it is possible to build the inversion-based control structure (Figure 46) with blue parallelograms as control operations (crossed pictograms indicates a control loop).

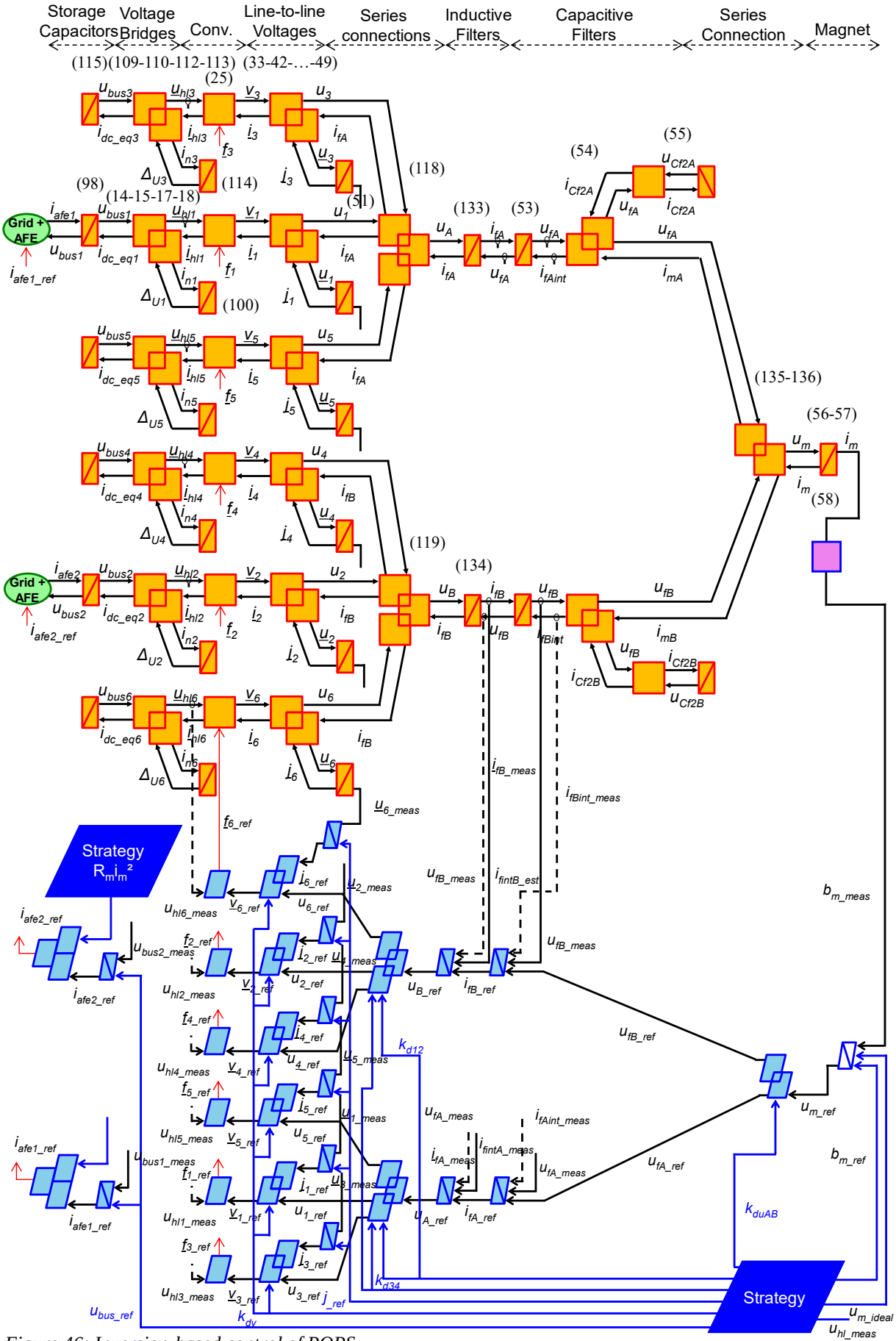


Figure 46: Inversion-based control of POPS

III.3. Energy management strategy of POPS

An energy management strategy (EMS) needs to be implemented to ensure that, at the end of a cycle, the floating capacitors are back to 5000 V. The EMS also need to consider when one of the converters, floating or charger, has a fault. The architecture and the modularity of the POPS allow it to work with a total of 5 modules minimum.

III.3.a. EMS in nominal mode

The Figure 47 presents a simplified description of POPS composed of 6 converters (4 floating converters and 2 charger converters). In this scheme, the inductive filters, capacitive filters are intentionally omitted. These elements are not included because they do not use energy during steady-state operation. The simplified model only represents the main components involved in the flow of energy during a cycle, the magnet and the storage capacitors.

The idea of the EMS is for the floating capacitors to deliver only the inductive voltage of the magnet and for the charger capacitors to supply the resistive losses of the switching losses of the floating converters.

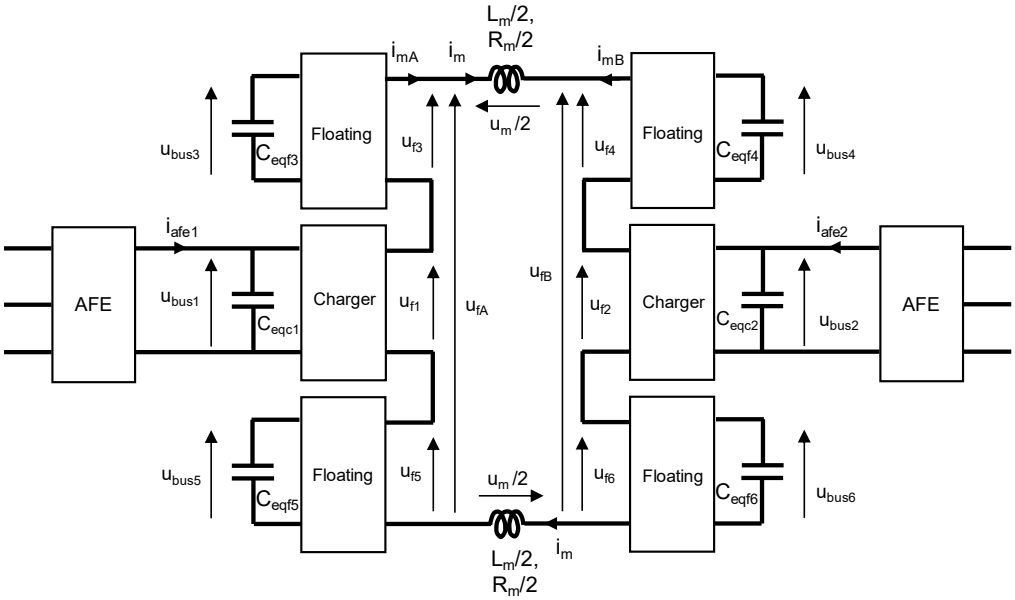


Figure 47 : Simplified scheme of POPS for EMS

The equivalent charging capacitance is the sum of the main storage capacitance and the voltage-bridge capacitance:

$$C_{eqc} = C_{bus} + C_{eq} \tag{139}$$

The equivalent floating capacitance is the sum of the main storage capacitance and the voltage-bridge capacitance:

$$C_{eqf} = C_{bus} + \frac{C_{eq}}{2} \quad (140)$$

The maximal and lowest voltages of the charger and floating capacitor are defined as:

$u_{bus-maxc}$ the maximal permissible voltage across all charger storage capacitors.

$u_{bus-maxf}$ the maximal permissible voltage across all floating storage capacitors.

$u_{bus-minc}$ the minimal permissible voltage across all storage charger capacitors.

$u_{bus-minf}$ the minimal permissible voltage across all storage floating capacitors.

The maximal available energy in one of the charger capacitors is:

$$E_c = \frac{1}{2} C_{eqc} u_{bus-maxc}^2 - \frac{1}{2} C_{eqc} u_{bus-minc}^2 \quad (141)$$

The maximal available energy in one of the floating capacitors is:

$$E_f = \frac{1}{2} C_{eqf} u_{bus-maxf}^2 - \frac{1}{2} C_{eqf} u_{bus-minf}^2 \quad (142)$$

The variable k_f is defined as the ratio of the energy available in the floating and the total energy:

$$k_f = \frac{E_f}{E_f + E_c} \quad (143)$$

The voltage u_m across the magnet can be written as:

$$u_m = 4v_f + 2v_c = R_m i_m + L_m \frac{di_m}{dt} \quad (144)$$

This equation is true if all the output voltage of the floating converter are equal and if the output voltage of the charger converter is equal:

$$u_{f3} = u_{f5} = -u_{f4} = -u_{f6} = v_f \quad (145)$$

And

$$u_{f1} = -u_{f2} = v_c \quad (146)$$

The voltage across the magnet can be split in 2, first into the resistive part:

$$v_r = R_m i_m \quad (147)$$

and into the inductive part:

$v_l = L_m \frac{di_m}{dt}$ where $u_m = v_r + v_l$

The voltage a floating converter needs to apply is:

$$v_f = \frac{k_f v_l}{4} \tag{148}$$

The voltage a charger needs to apply is:

$$v_c = \frac{(1-k_f)v_l+v_r}{4} \tag{149}$$

Thus, the energy of the inductive part of the magnet will be supplied by the floating capacitors. The energy of the resistive part and the losses of the converters will be provided by the AFEs through the chargers.

By combining (144) with (148) and (149):

$$u_m = 4v_f + 2v_c = 4\left[\frac{(k_f v_l)}{4}\right] + 2\left[\frac{(1-k_f)v_l+v_r}{2}\right] = k_f v_l + \left(1-k_f\right)v_l + v_r = v_l + v_r \tag{150}$$

Since

$$v_l = u_m - v_r$$

The voltage that needs to be delivered by each charger converter is:

$$v_{c_ref} = \frac{[(1-k_f)(u_{m_ref}-v_r)+v_r]}{2} \tag{151}$$

The voltage that needs to be delivered by each floating converter is:

$$v_{f_ref} = k_f \frac{(u_{m_ref}-v_r)}{4} \tag{152}$$

The AFEs supply the energy required by the resistive part of the magnet, it is therefore necessary to have:

$$i_{afe1} = \frac{R_m i_m^2}{(2u_{bus1})} \tag{153}$$

$$i_{afe2} = \frac{R_m i_m^2}{(2u_{bus2})} \tag{154}$$

Ultimately, the AFEs are controlled in power. Therefore:

$$P_{afe1_ref} = \frac{R_m i_m^2}{2} \tag{155}$$

$$P_{afe2_ref} = \frac{R_m i_m^2}{4} \tag{156}$$

Figure 48 shows the EMR and the inversion-based of the previous scheme. The control of the current i_m will be obtained from the control of u_m, so u_{fA} and u_{fB} so from u_1, u_3, u_5 and u_2, u_4, u_6. The inversion of the coupling elements creates degrees of freedom that are determined by the strategy established previously.

$$u_m = u_{fA} - u_{fB} \tag{157}$$

where:

$$\begin{cases} u_{fA_ref} = k_{fuAB} u_{m_ref} \\ u_{fB_ref} = -(1 - k_{fuAB}) u_{m_ref} \\ u_{m_ref} = u_{fA_ref} - u_{fB_{ref}} \end{cases} \tag{158}$$

k_{fuAB} correspond to a degree of freedom from the double coupling element. To make the 2 sides A and B operate in a symmetrical manner, the default value of k_{fuAB} is 0.5.

Using Kirchhoff voltage law, u_{fa} and u_{fb} can be written as:

$$u_{fA} = u_{f1} + u_{f3} + u_{f5} \tag{159}$$
$$u_{fB} = u_{f2} + u_{f4} + u_{f6} \tag{160}$$

Considering the previous strategy and the desire to make the floating elements operate identically, the reference values of the individual components are determined accordingly.

$$u_{1_ref} = (1 - k_f)\left(u_{fA_ref}\frac{v_r}{2}\right) + \frac{v_r}{2} \tag{161}$$
$$u_{3_ref} = u_{5_ref} = k_f \frac{(u_{fA_ref} - \frac{v_r}{2})}{2} \tag{162}$$
$$u_{2_ref} = -[(1 - k_f)\left(u_{fB_{ref}}\frac{v_r}{2}\right) + \frac{v_r}{2}] \tag{163}$$
$$u_{4_ref} = u_{6_ref} = -k_f \frac{(u_{fB_ref} - \frac{v_r}{2})}{2} \tag{164}$$

With the parameters k_f and v_r which are distribution input coming from the coupling elements linking the voltages of the converters. The other implicit choice is the equivalent distribution of the floating voltage $u_{f3_ref} = u_{f5_ref}$ and $u_{f4_ref} = u_{f6_ref}$

The value v_r is obtained from the measurement of the current and from the known value of the resistance R_m.

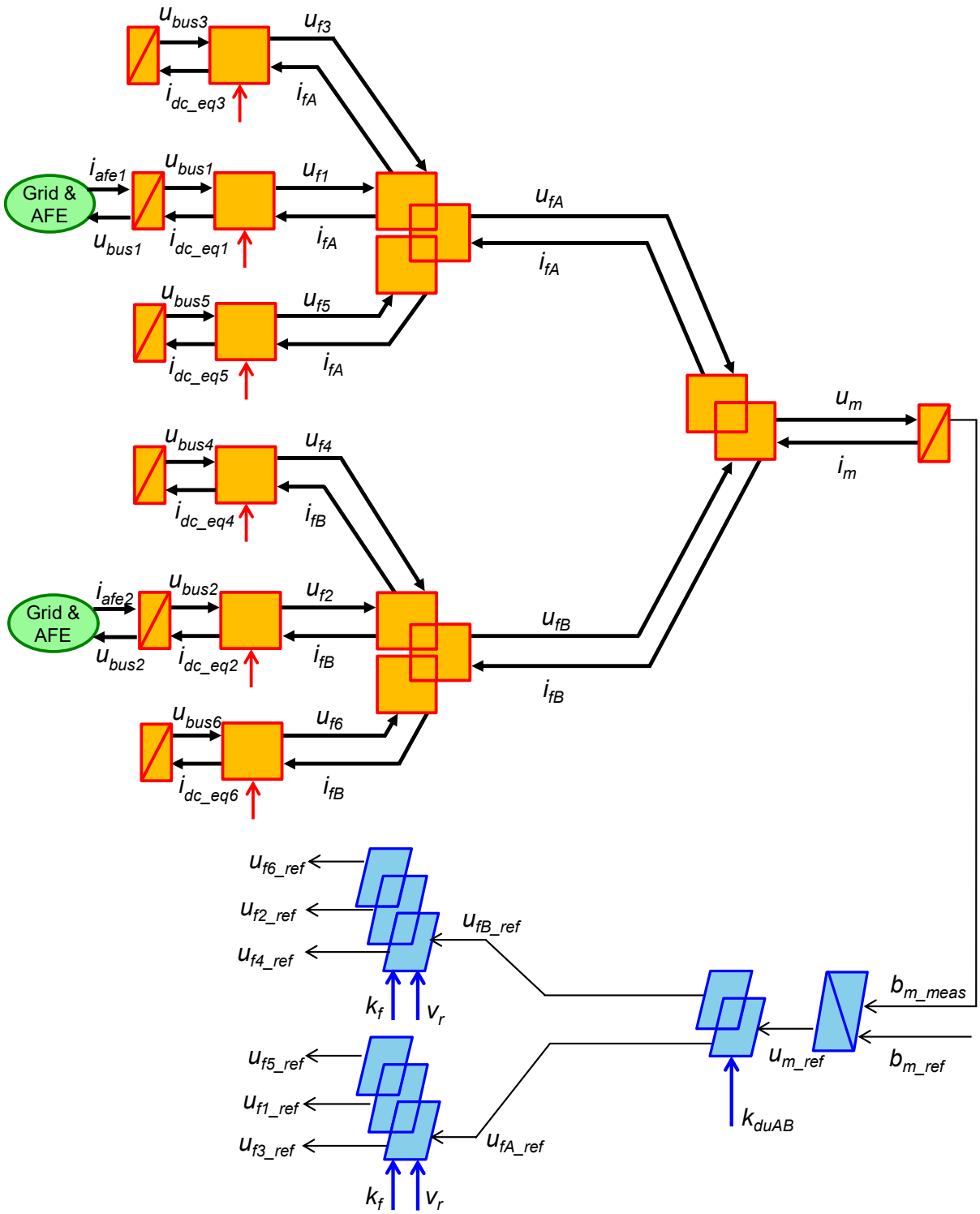


Figure 48: Simplified EMR and inversion-based for EMS

III.3.b. EMS in fault mode

When working in fault mode, one of the 6 converter is off. The faulty converter is bypassed by a power switch at its output.

The following general case is considered:

N_{CA} : Number of charger side A
N_{CB} : Number of charger side B
N_{FA} : Number of floating side A
N_{FB} : Number of floating side B

The computation of the required voltage is done in annexe F, the input required are:

-u_{AFi_ref} the voltage reference to send to the floating of the odd side.

-u_{BFj_ref} the voltage reference to send to the floating of the even side.

-u_{ACk_ref} the voltage reference to send to the charger of the odd side.

-u_{BCl_ref} the voltage reference to send to the charger of the even side.

with $i \in [0, N_{FA}]$
with $j \in [0, N_{FB}]$
with $k \in [0, N_{CA}]$
with $l \in [0, N_{CB}]$

$k_{AUF}, k_{AVR}, k_{BUF}, k_{BVR}, FL, FLV$ and CHU are coefficients used to simplify the computations. They are determined in functions of the number of available converters and k_f (see Annexe F).

The total voltage required for the odd side is:

$$u_{fA_ref} = k_{AUF} u_{m_ref} + k_{AVR} v_r \quad (165)$$

The total voltage required for the even side is:

$$u_{fB_ref} = k_{BUF} u_{m_ref} + k_{BVR} v_r \quad (166)$$

The voltage for N floating converter on the odd side is:

$$u_{AFi_ref} = \frac{[u_{fA_ref} - (k_{AUF} + k_{AVR}) v_r] FL}{k_{AUF}} \quad (167)$$

And the voltage for N floating converter on the even side is:

$$u_{BFj_ref} = \frac{[-u_{fB_ref} + (k_{BUF} + k_{BVR}) v_r] FL}{k_{BUF}} \quad (168)$$

The voltage for the charger converter on the odd side:

$$u_{ACk_ref} = \frac{[CHU u_{fA_ref} + (k_{AUF}.FLV - k_{AVR}.CHU) v_r]}{k_{AUF}} \quad (169)$$

The voltage for the charger converter on the even side:

$$u_{BCl_ref} = \frac{(-CHU)u_{fB_ref}+(-k_{BUF}.FLV+k_{BVR}.CHU)v_r]FL}{k_{BUF}} \quad (170)$$

Figure 49 shows the implementation of the general strategy into the inversion-based control.

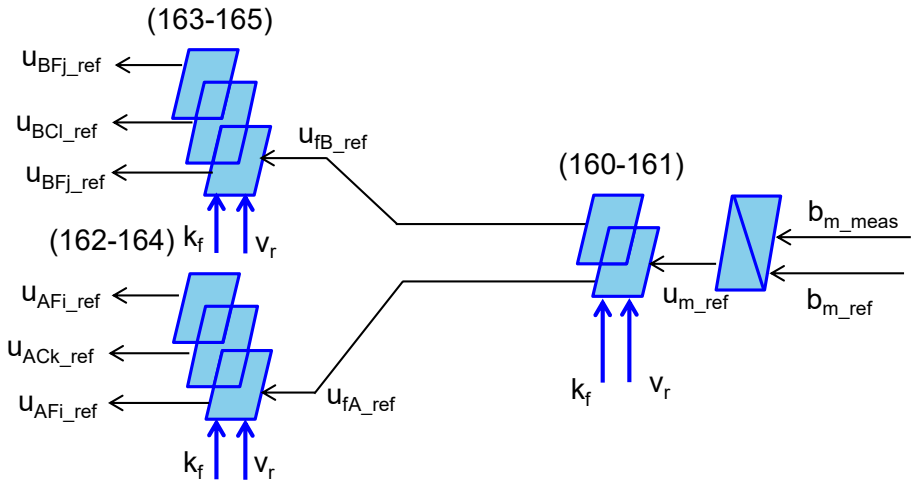


Figure 49: Implementation of the general EMS

III.4. Control performances in simulation

The simulation is done with MATLAB-Simulink© using the EMR library (EMR website). A reference with a maximal peak of 13500 G is used (Figure 50). A step time of 1 µs is chosen for the 1.1 s simulation with an ode4 Runge-Kutta solver.

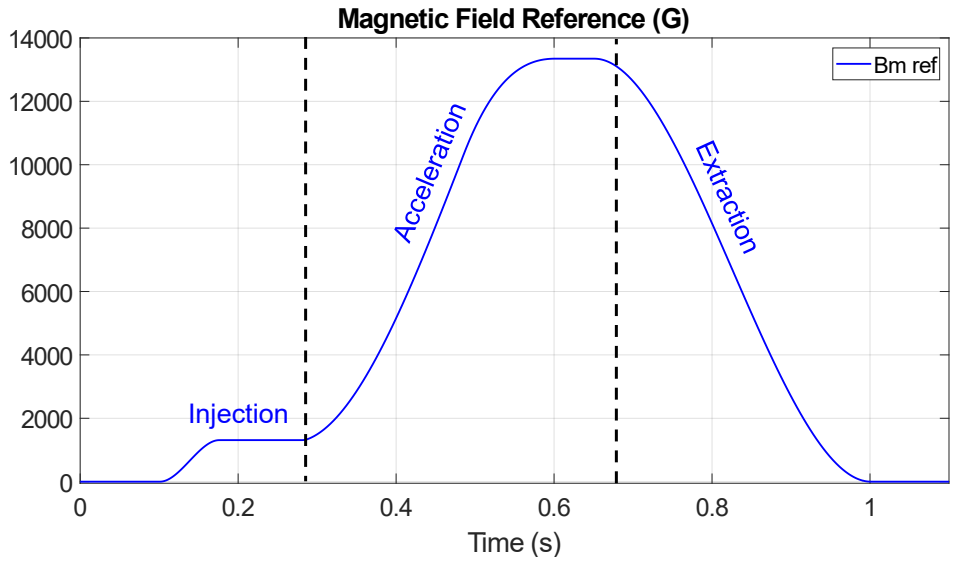


Figure 50: Magnetic field reference of POPS

III.4.a. Control performances in average value

The converter is modelled in average value The sampling, the minimal ON time, the dead times and the discretization of the controllers are not taken into account. The indirect inversion uses analogue PI controllers with a damping factor of 1. The response time for the filter inductances is 2.5 ms. The response time is 7.5 ms for the filter capacitances (three times greater than the previous one to decoupled both loops). And a time of 22.5 ms for the magnet loop is chosen. The integrators are reset at the start of the cycle.

The current i_{fA} is similar to the magnetic field reference, it has bumps at the start, at the start of the ramp and in the middle the ramp, to break the voltage dynamics of u_f (Figure 51.a). i_{fB} is the current going in the even side of the converter. The voltage u_f is the voltage across the magnet, follows the derivative of the magnetic reference (Figure 51.b). The magnetic field b_m in the magnet follow the reference (Figure 51.c). The magnetic field error, almost satisfies the strict specification of maximum 100 ppm. The magnetic field is going slightly above the threshold during the high dynamic variation of the reference. This is noticeable at the beginning, the field overshoots by $\mp$1.7 G. There is another overshoot of 0.5 G and -1 G at the start of the 2nd ramp. The last overshoot can be ignored since the cycle is finished, and the particle is not in the accelerator anymore. During the flat tops the magnetic field stays within the error margin (Figure 51.d).

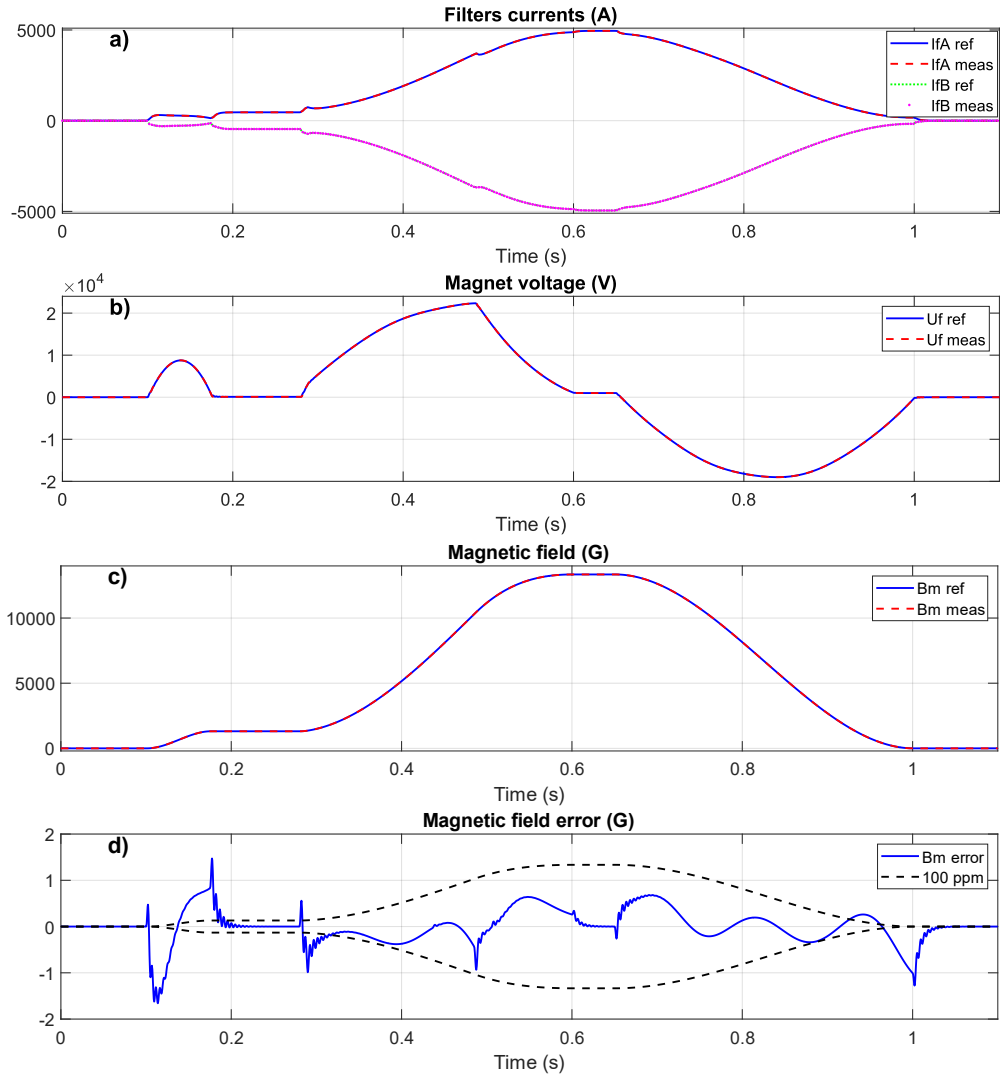


Figure 51: Simulation of POPS using inversion-based control a) currents in the inductive filters, b) voltage across the magnet, c) magnetic field, c) error of the magnetic field with an error of 100 ppm.

As the simulation is run in average value, the PWM is not present and not impacting the current i_{11} to i_{16} so they are the image of i_{fA} divided by 3 (Figure 52). In average value the circulating currents j are equal to 0 (Figure 52.b).

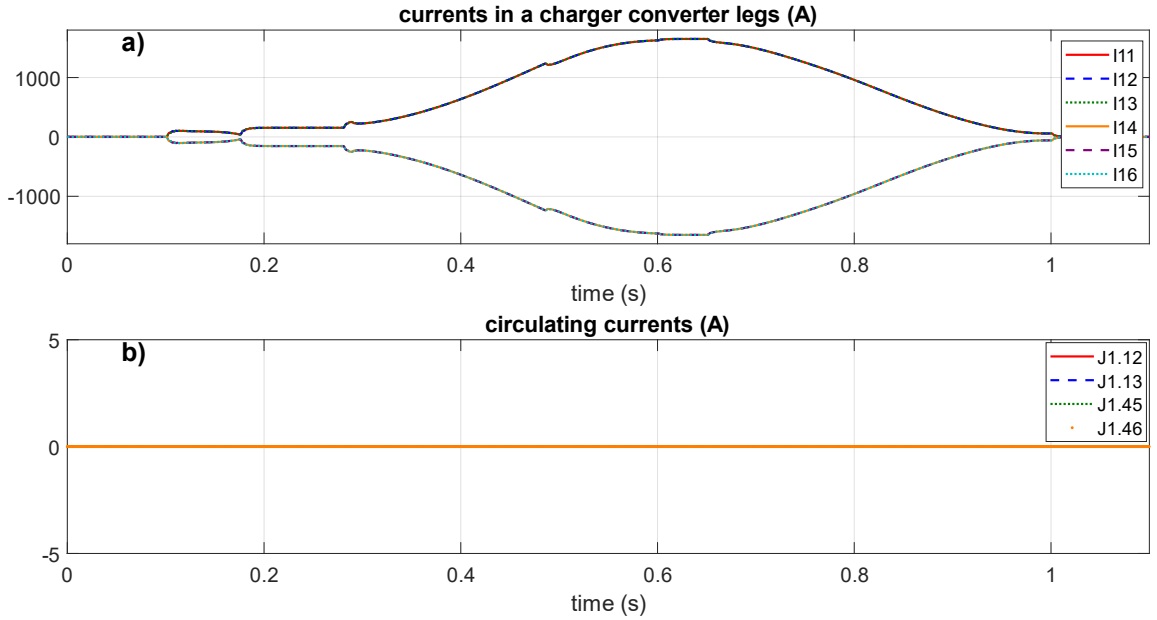


Figure 52: Simulation of inversion-based control a) current in a charger converter leg, b) 4 circulating currents j

Only one of the 4 floating is shown in average value, the results are the same for the other floating converters (Annexe-G). The currents i_{31} to i_{36} are the image of i_{fA} divided by 3 (Figure 53.a). No non-linearities affect the leg currents, so they are balanced and therefore j is equal to 0 (Figure 53.b).

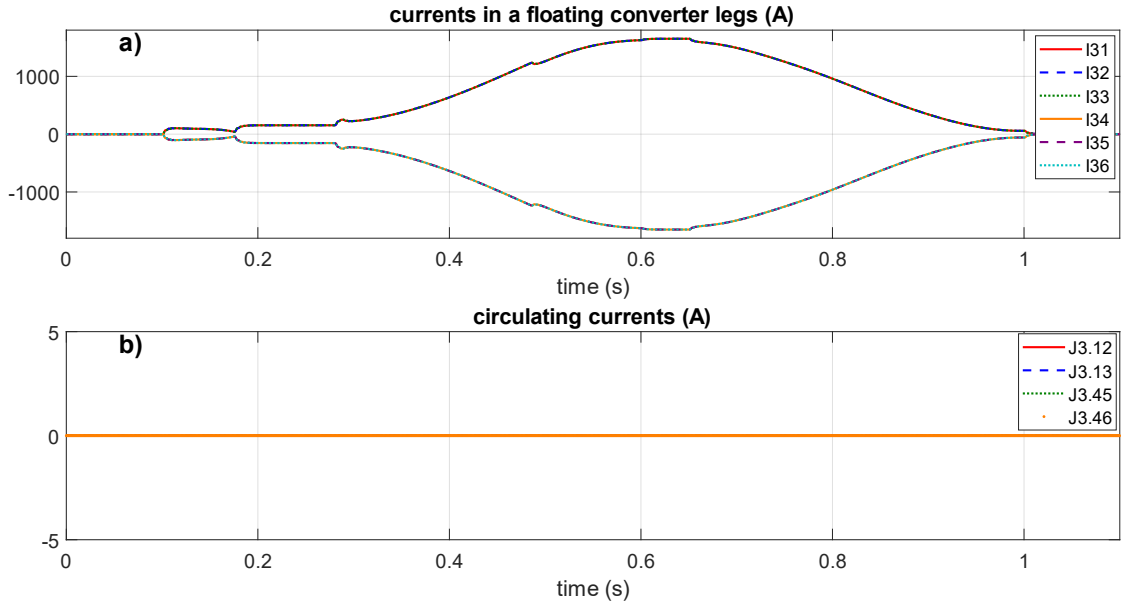


Figure 53: Simulation of inversion-based control a) current in a floating converter leg, b) 4 circulating currents j

During a cycle the voltage across C_{h1} and C_{l1} of the charger are not diverging, they stay at the same value. The discharge is noticeable when the pulse starts, and their voltage go back to 2500V at the end of the cycle (Figure 54.a). The voltage unbalance starts with a chosen unbalance of -1V. This unbalanced is overcome as soon as the current is flowing in the converter (Figure 54.b). No capacitor voltage

unbalance appears in the average model, since the unbalance is introduced by the PWM switching, which unequally stresses the DC bus capacitors.

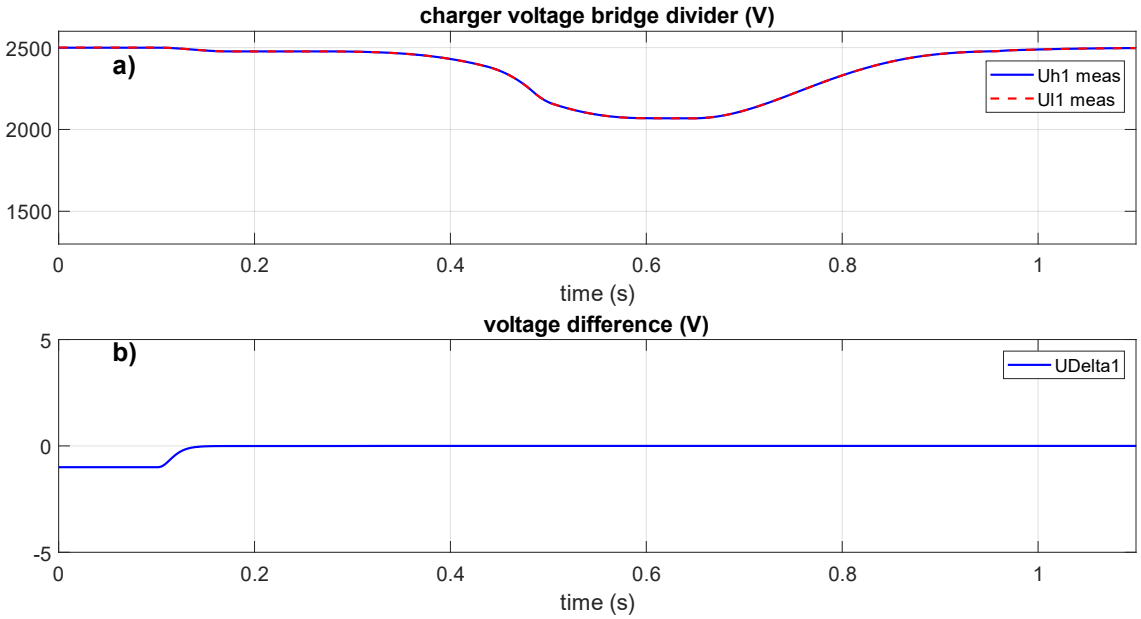


Figure 54: Simulation using inversion-based control a) voltages of a charger bridge divider, b) difference of the voltage between uh1 and ul1

The voltage across C_{h3} and C_{l3} of the floating capacitor are not diverging, they stay at the same value. The discharge is noticeable when the pulse starts, and their voltage go back to 2500V at the end of the cycle (Figure 55.a). The voltage unbalance starts with a chosen unbalance of -1V. This unbalanced is overcome as soon as the current is flowing in the converter (Figure 55.b). The imbalance is corrected later as the floating starts commutating at the start of the 2nd ramp. No capacitor voltage imbalance appears in the average model, since the imbalance is introduced by the PWM switching, which unequally stresses the DC bus capacitors. The other storage capacitors are shown in Annexe-G.

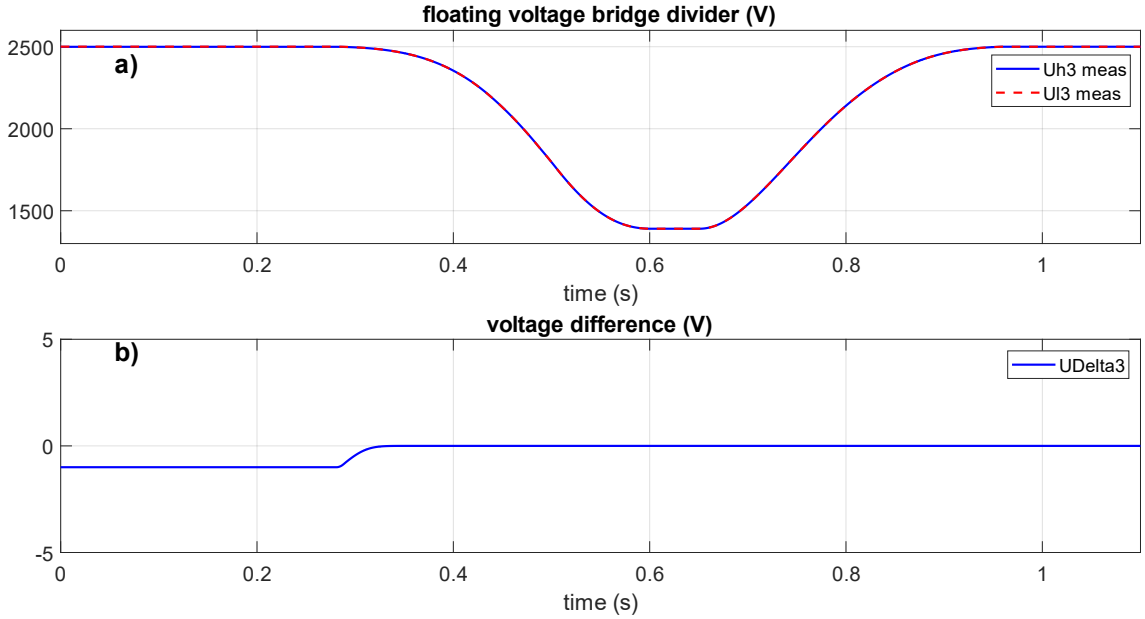


Figure 55: Simulation of inversion-based control a) voltages of a floating bridge divider, b) difference of the voltage between uh3 and ul3

u_{bus1} is the voltage of a charging storage capacitor, it changes with the current demand, when i_m ramps up it discharges, when i_m is descending the capacitor is charging (Figure 56.a). The voltage of the floating capacitor u_{bus3} discharge during the acceleration and return to its initial voltage of 5000V at the end of the cycle to ensure the next. Only 1 type of each capacitor is shown since they have the same behaviour, the remaining 4 are presented in Annexe-H. i_m is the current in the magnet it is similar to b_m, the current is slightly saturating during the flat top (Figure 56.b).

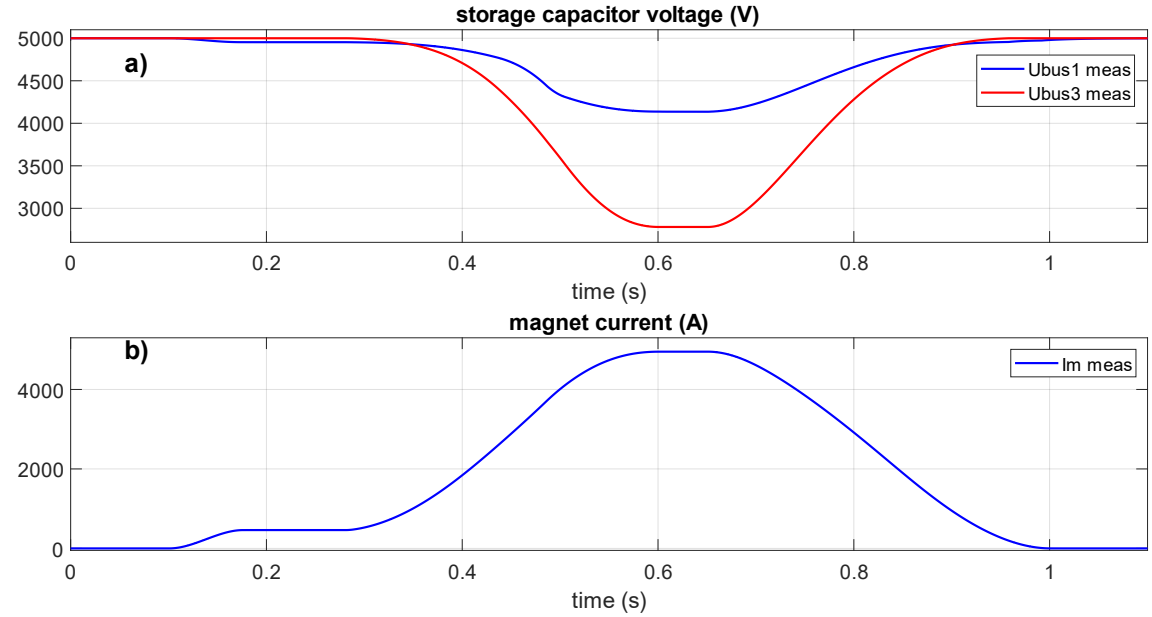


Figure 56: Simulation of inversion-based control a) voltages of the storing capacitors charging and floating, b) current in the magnet

The simulation results demonstrate that the inversion-based control strategy allows the magnetic field in the magnet to closely follow the reference with a flat top of 13 500 G. The magnetic field error remains within the required 100 ppm specification during steady operation, with only small overshoots observed during rapid reference variations. In the average model, the converter currents remain balanced and no circulating currents appear, while capacitor voltages stay stable throughout the cycle. These results confirm the effectiveness of the control strategy under the average-value simulation assumptions.

III.4.b. Control performances in discrete value

The discrete results using the inversion-based control are obtained by considering a 3-level PWM for each converter. The converters are shifted between them by 45°, 90° and 135° to reduce the current ripple. The model uses discrete integrators with a sampling time of 500 µs. The controller for the filter inductances has a response time of 2.5 ms. The response time is 7.5 ms for the filter capacitances, it is 5 times greater than the previous one for decoupling and accounts for the non-linearities inherent of the discrete model. And it is 22.5 ms for the magnet controller. The integrators are reset at the start of the cycle.

The current i_{fA} is similar to the magnetic field reference, it has bumps at the start, at the start of the ramp and in the middle the ramp, to break the voltage dynamics of u_f (Figure 57.a). i_{fB} is the current going in the even side of the converter. The voltage u_f at the output of the filter capacitance follows the derivative of the reference (Figure 57.b). The magnetic field b_m in the magnet follow the reference of a trapeze with a flat top of 13500 G (Figure 57.c). The magnetic field error, defined as $(b_{m_ref} - b_{m_meas})$, almost satisfies the strict specification of 100 ppm. The magnetic field is going slightly above the threshold during the high dynamic variation of the reference. This is noticeable at the beginning, the field overshoots by -1.8 G, then by 1.5 G when transitioning to the 2nd flat top and by -1 G before the ramp. During the flat top, the error stays within the threshold. The last overshoot can be ignored since the cycle is finished, and the particle is not in the accelerator anymore (Figure 57.d).

Compared to the average results, the error shows oscillations due to non-linearities, PWM and sampling effects. However, these oscillations remain sufficiently small, due to the high inductance of the magnet and the filtering done by the inductive and capacitive filters, so that the error stays within the 100 ppm margin.

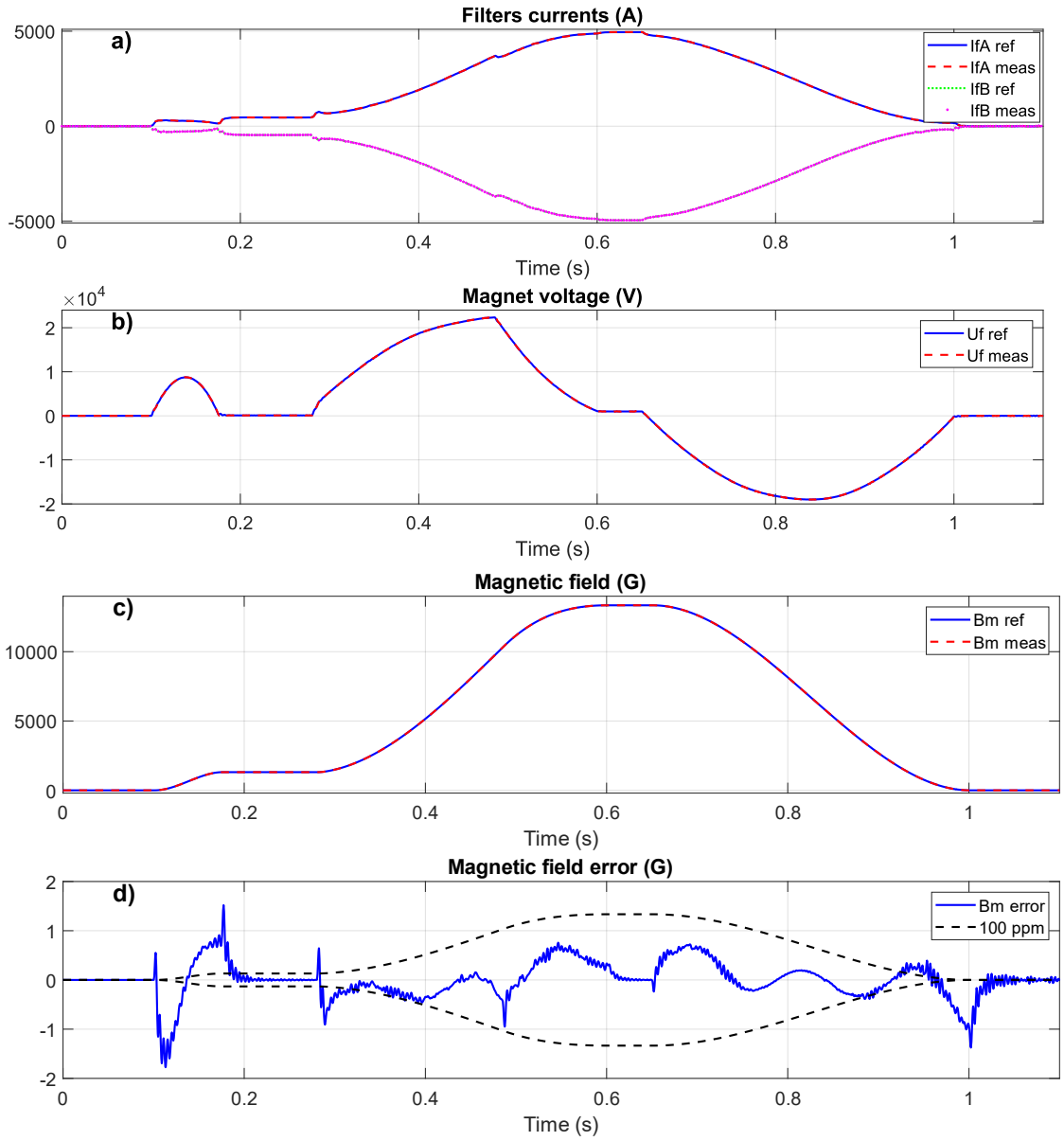


Figure 57: Discrete simulation of POPS using inversion-based control a) current in the inductive filter, b) voltage of the capacitive filter, c) magnetic field, d) error of the magnetic field.

Figure 59 shows the leg current i_{11} to i_{16} of a charger converter, they are the image of i_f divided by 3. The effect of the PWM is noticeable, all currents have a ripple of 333Hz, with a maximal amplitude of 235 A during the ramp. $\underline{j}$ are the circulating currents in the converter legs (Figure 59.b), the closer to 0 the more balanced the current. When the current is in steady state $\underline{j}$ is near 0. The main issues are during the high dynamics, there can be a difference of up to 72 A, it is due to the fact that the 1st leg is commuting before the 2nd.

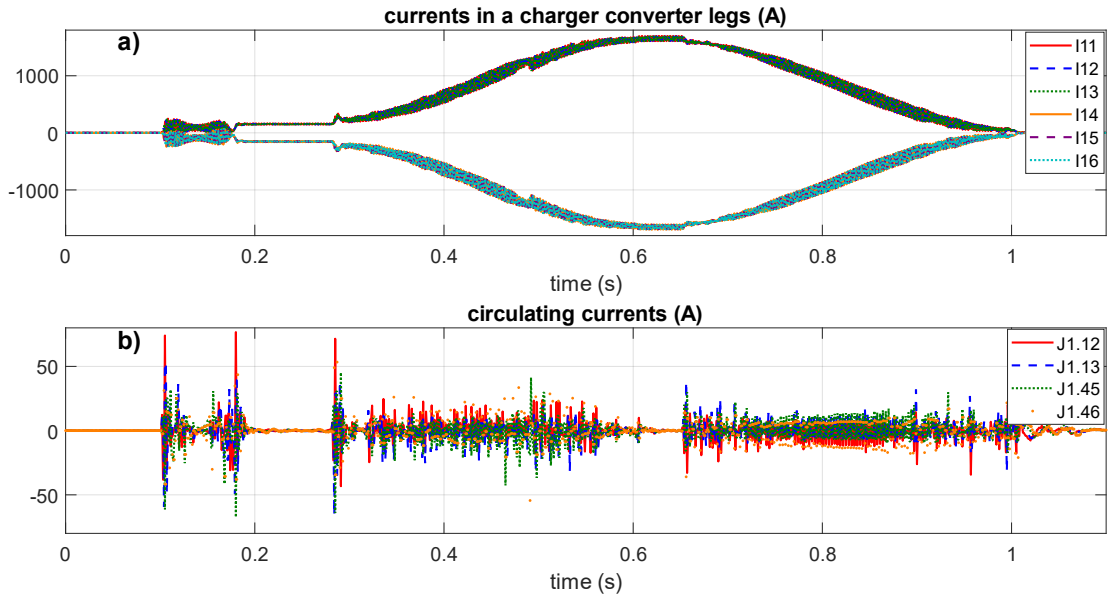


Figure 59: Discrete simulation of POPS using inversion-based control a) current in a charger converter leg, b) 4 circulating currents j

The leg currents i_{31} to i_{36} of a floating converter are the image of i_{fA} divided by 3 (Figure 58.a). The effect of the PWM is noticeable, all currents have a ripple of 333Hz, with a maximal amplitude of 250 A during the ramp. $\underline{j}$ are the circulating currents in the converter legs (Figure 58.b). The main issues are during the high dynamics, there can be a difference of up to 70 A. This result shows that, by decomposing the interleaved inductive filter into an equivalent inductance. It is possible to impose a low circulating current. It validates the approach of imposing j=0.

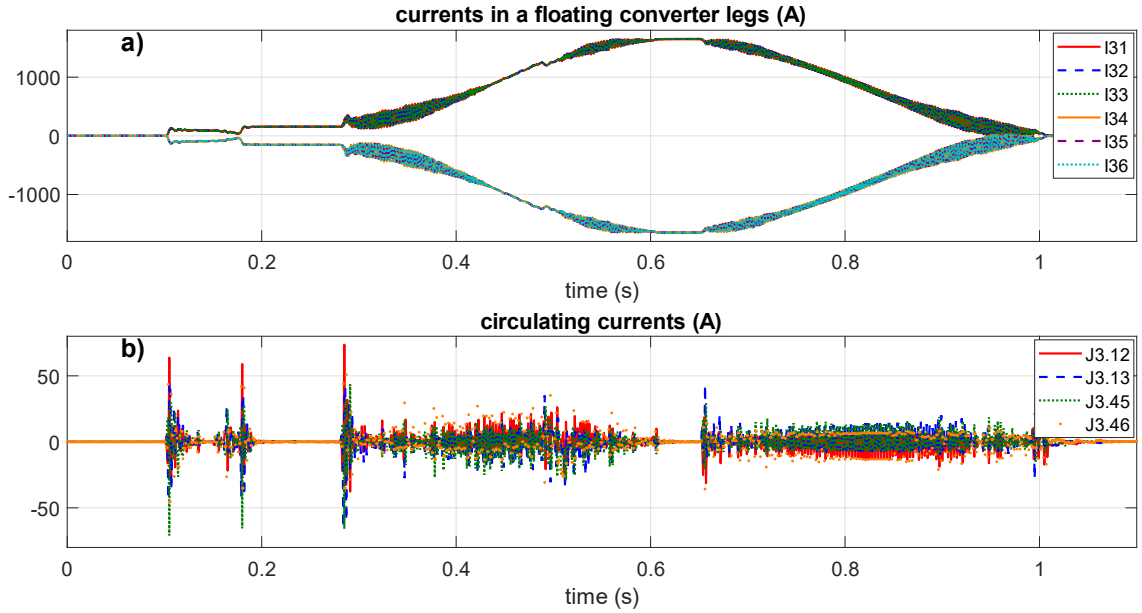


Figure 58: Discrete simulation of POPS using inversion-based control a) current in a charger converter leg, b) 4 circulating currents j

During a cycle the voltages across C_{h1} and C_{l1}, the capacitors of a charger bridge divider, are not diverging, they stay at the same value. The discharge is noticeable when the pulse starts, and their voltage go back to 2500 V at the end of the cycle (Figure 60.a). The voltage imbalance starts with an initial offset of –1 V. This imbalance is corrected as soon as the current begins to flow in the converter (Figure 60.b). The maximal difference between the two voltages is 17 V(=0.68%) during the high dynamics, the voltage difference converges towards 0V at the end of a cycle. This result shows that acting on the distribution input k_{dv}, the voltages of the bridge divider can be balanced.

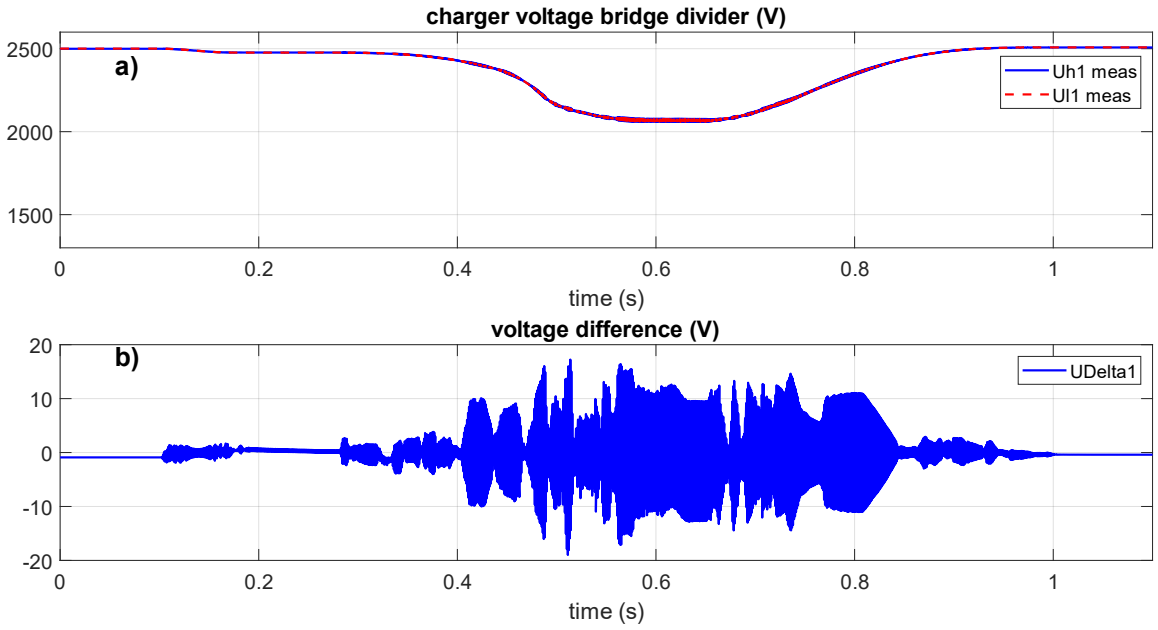


Figure 60: Discrete simulation of POPS using inversion-based control a) voltages of a charger bridge divider, b) difference of the voltage between uh1 and ul1

The voltage across the capacitor of a floating bridge divider C_{h3} and C_{l3} are not diverging. They stay at the same value. The discharge is noticeable when the pulse starts, and their voltage go back to 2500V at the end of the cycle (Figure 61.a). The voltage unbalance starts with a chosen unbalance of -1V. This unbalanced is overcome as soon as current is flowing in the converter (Figure 61.b). The imbalance is corrected later as the floating starts commutating at the start of the 2nd ramp. The maximal difference between the two voltages is 18 V(=0.72%).

The voltage of the charger capacitor u_{bus1} changes with the current demand. When i_m ramps up, it discharges, when i_m is descending, the capacitor is charging (Figure 62.a). The voltage of the floating capacitors u_{bus3} discharge during acceleration and return to its initial voltage of 5000V at the end of the cycle to ensure the next. i_m is the current in the magnet it is similar to b_m (Figure 62.b). The 4 remaining voltages are shown in the Annexe-H.

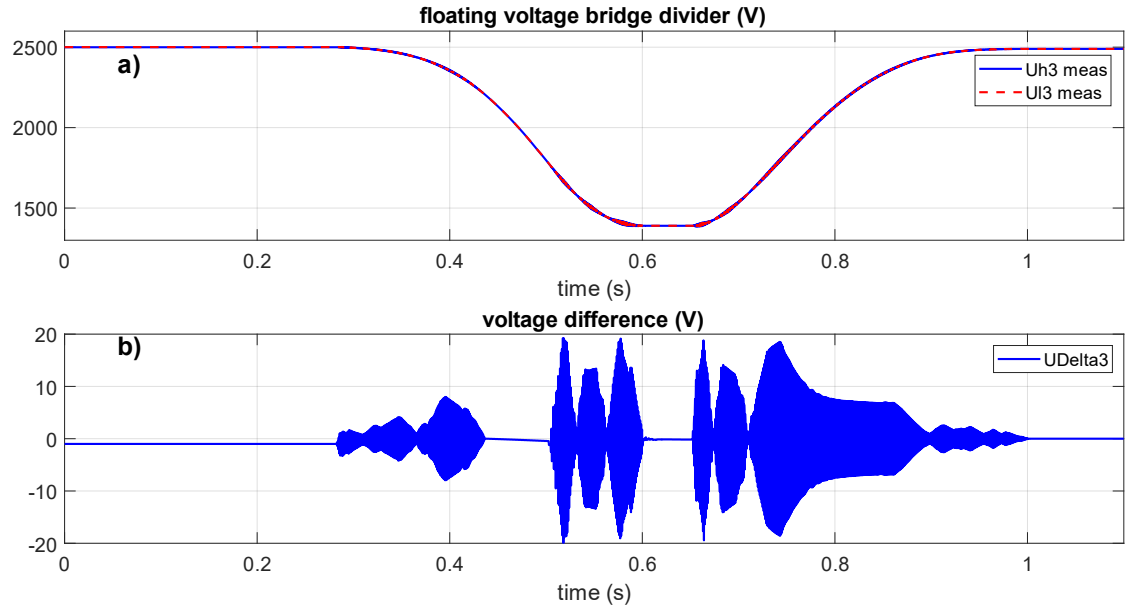


Figure 61: Discrete simulation using inversion-based control a) voltages of a floating bridge divider, b) difference of the voltage between uh3 and ul3

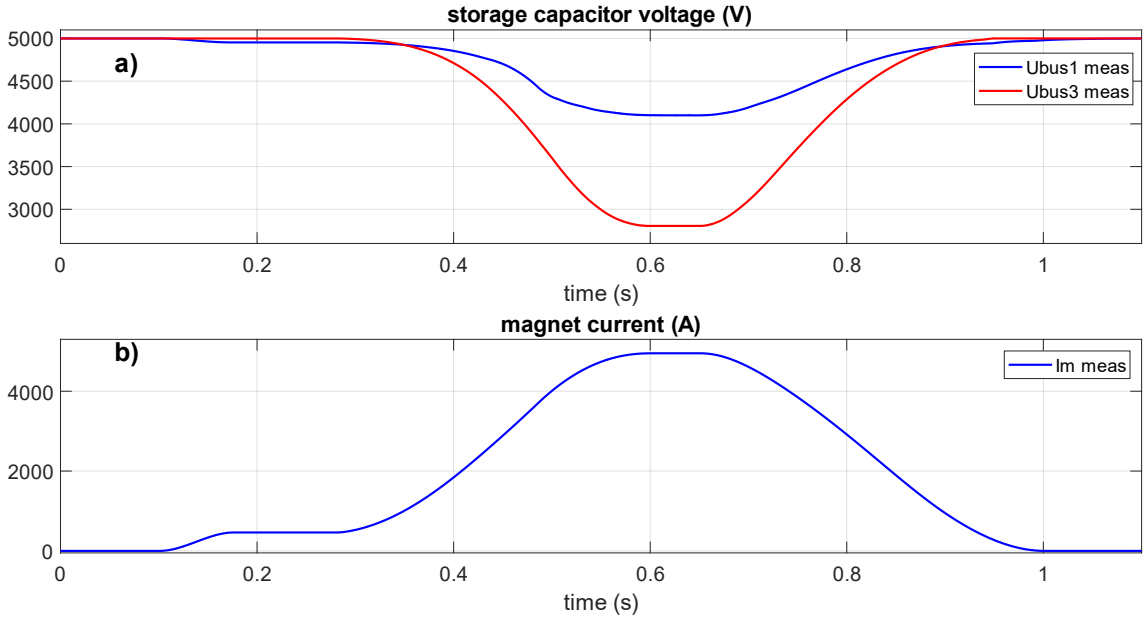


Figure 62: Discrete simulation using inversion-based control a) voltages of the storing capacitors charging and floating, b) current in the magnet

The discrete simulations confirm that the inversion-based control strategy successfully follows the magnetic field reference while maintaining system stability. Despite transient overshoots during high dynamic phases, the magnetic field error remains close to the 100 ppm specification and stays within limits during the flat-top region. Current ripples and temporary circulating current imbalances appear due to PWM and switching delays but remain short and do not trigger safety limits. Thanks to the

developed strategy, the capacitor voltages and energy storage behaviour remain well balanced throughout the cycle, ensuring reliable operation for subsequent cycles.

III.4.c. Conclusion of POPS results

This chapter presents the modelling and control of the POPS system using the EMR formalism and the inversion-based control approach. The modelling incorporates the floating capacitors, interleaved inductive filters, and the series connection of converters, enabling a complete representation of the system dynamics. The complete EMR has been easily built as an extension of the unitary system (cf. Chapter II). For future extension of POPS this property is a key point.

Based on this model, a systematic control structure and an energy management strategy is derived to ensure proper energy distribution and recovery of the capacitor voltages at the end of each cycle. The inversion-based control highlights the degrees of freedom to define by the strategy. Each degree of freedom is used to solve a constraint (e.g. voltage unbalance, circulating currents).

Simulation results in both average and discrete values demonstrates that the control strategy enables accurate tracking of the magnetic field reference while maintaining stable capacitor voltages and balanced currents with 100 ppm in steady state. Overall, the proposed control and energy management strategy architecture ensure reliable operation of the POPS.

The inversion-based control, has been validated in simulation but an experimental validation is required before an implementation on the real system.

IV. Experimental implementation of the inversion-based control

The inversion-based control of the POPS has been developed from the EMR of this power systems, in a progressive way. But before application on the full-scale real system, an experimental validation is required. After analysis of different solutions, a reduced-scale power system has been chosen for this experimental validation. This low-power experimental set-up was used in the past for the validation of the on-going RST-based control. Experimental results are provided to check the performance of the real-time implementation of the inversion-based control.

IV.1. Experimentation on mini-POPS-B

IV.1.a. Description of mini-POPS-B

Mini-POPS-B is a 1 to 100 scaled-down version of the POPS-B converter (Figure 63), developed in 2016 to assess the feasibility of the POPS-B power converter for use in the Booster particle accelerator. The peak magnet current of the real converter is 6 kA, with a DC nominal voltage of 5 kV. The scaled values are respectively 60 A and 50 V. The scaling factor of the voltages and currents leads to maintaining the same values of resistances, inductances and capacitances. The power is scaled by a factor 10000 (see Table 2 for component values).

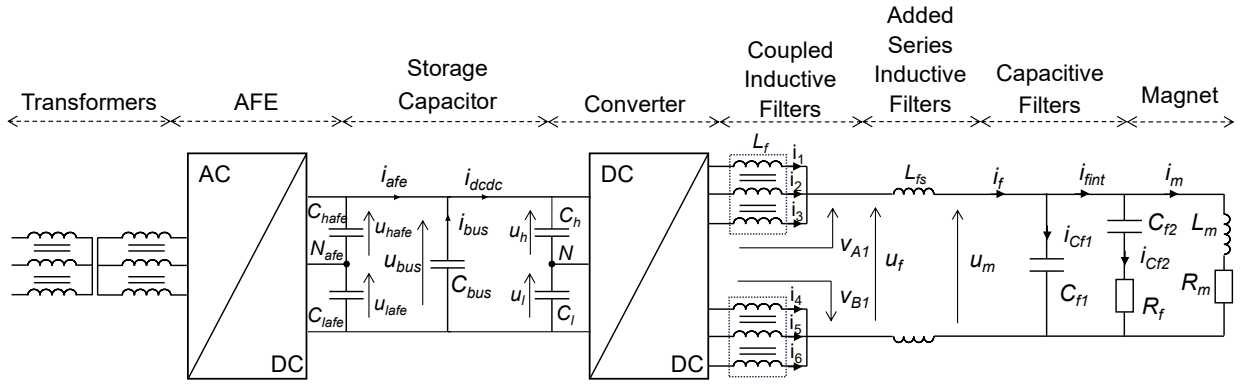


Figure 63: Layout of mini-POPS-B

Table 2: Parameters of mini-POPS-B

Parameters	Values	Unit
Electromagnet inductance	0.1	H
Electromagnet resistance	0.24	Ω
R-C filter branch capacitance	1440	μF
R-C filter branch resistance	2.2	Ω
C filter branch capacitance	160	μF
Series inductive filter inductance	2	mH

Series inductive filter resistance	10	mΩ
Coupled inductive filter differential inductance	2.8	mH
Coupled inductive filter common inductance	10	mH
Coupled inductive filter resistance	10	mΩ
Voltage bridge capacitance	9	mF
Storage capacitance	282	mF
Transformer inductance	0.4	mH

The input stage uses a three-phase transformer DY 400V/19.5V with a power rate of 500 VA (Figure 64). It is connected to the 400 V grid through a circuit breaker. In series to the transformer, a three-phase filter inductor of 0.4 mH is connected. Its goal is to increase the input inductance allowing the AFE to increase the voltage. In parallel to the input transformer, there is a synchronisation transformer, also 400V/19.5V, which is used for voltage measurement.



Figure 64: Transformers of input stage of mini-POPS-B

A DC/DC PCB (Printed Circuit Board) (Figure 65), is composed of 3 NPC legs. The switching components are MOSFETs, mounted under a heat sink together with recovery diodes and clamp diodes. MOSFETs drivers are integrated on the card and are driven by the controller through electrical pulses via a 20 pin flat cables coming from the digital outputs of the FGC3. 12 capacitors with a value of 1500 µF form the two semi-voltages with a total of 9 mF (6 in parallel). Current and voltage measurements are implemented directly on the card. They measure the currents flowing through each leg and the half-bridge divider voltage. Two output connector bars are placed at the rear of the PCB.



Figure 65: Front and back of a DC/DC PCB.

The upper connector provides all the measurements mentioned above and the ± 15 VDC auxiliary power supply required for the drivers and the measurements circuits. The lower connector is used for the power connections. It provides 3 current connections, and the DC-link connection with accessible an accessible neutral point. A total of 3 cards are used. 1 operates for the AFE and the other 2 for half of a 6-legged DC/DC converter. The 2 cards used for the DC/DC converter have their neutral point connected via the lower rear connector.

The storage capacitors (Figure 66), are is composed of 6 electrolytic capacitors of 47 mF, 65 VDC each connected in parallel, to have a total capacitance of 0.282 F. The capacitors are connected in parallel to the power cards, the AFE and the DC/DC. When the DC-link is charged to its nominal 50 V voltage, an energy of 352.5 J is stored. A resistor is connected in parallel to the capacitors through a circuit breaker to discharge the DC-link in case of a trip of the converter.



Figure 66: Storage capacitors of mini-POPS-B and discharge resistor

The output filters (Figure 67) are placed on the back of the platform. 4 three-phase inductors of 2.8 mH are used as differential mode inductors to decouples the converter legs. For the common mode inductance 4 single phase inductors of 0.5 mH are connected in series, two per module, after the parallel connection of the 3 legs. As they are all in series, the total inductance is 2 mH. The common mode inductances are added to provide more inductance. To model them, the value of L and R are added to the equivalent common mode inductance.



Figure 67: Output inductive filters of mini-POPS-B

The capacitive filter (Figure 68) consisting of 2 parallel branches is mounted on a PCB. The board includes a total of 13 capacitors, each with a capacitance of 160 μF. The first branch is formed by 4 capacitors arranged as 2 series pairs connected in parallel for a capacitance of 160 μF. The second branch consists of 9 capacitors connected in parallel, for a capacitance of 1440 μF, with a 2.2 Ω resistor connected in series with this capacitor bank. The measures of the magnet voltage and current are also performed on this board and sent to the analogue input card through a Burndy cable.



Figure 68: Capacitive filter of mini-POPS-B

The load (Figure 69) is used to simulate the accelerator magnets. It consists of an inductor with a nominal inductance of 100 mH and a nominal resistance of 0.24 Ω.

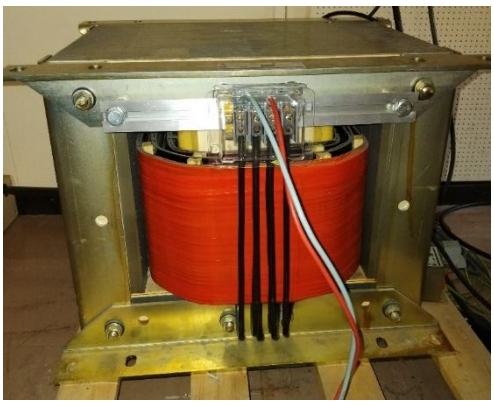


Figure 69: Magnet of mini-POPS-B

The control of mini-POPS-B is done with 2 ECU (Electronic Control Unit). A FGC3 using an RST controller for the current loop. A DSP is connected to the FGC3, receiving the voltage reference of the magnet, and controls the inner loop, the voltage regulation and the current balance. The DSP also sends the switching orders to the AFE and the DC/DCs (Figure 70).

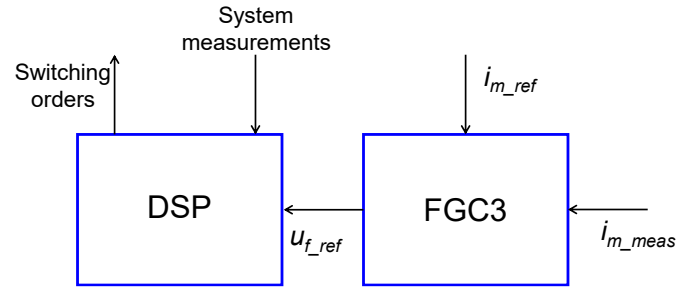


Figure 70 : Overview of mini-POPS-B ECU

For the experimentations, the control of the AFE is already implemented in the DSP. It is regulated with a PI controller.

The reference used is made of an injection phase, an acceleration phase with a current peak of 33A and an extraction phase (Figure 71). The regulation of the experimentation is done with the current and not the magnetic field.

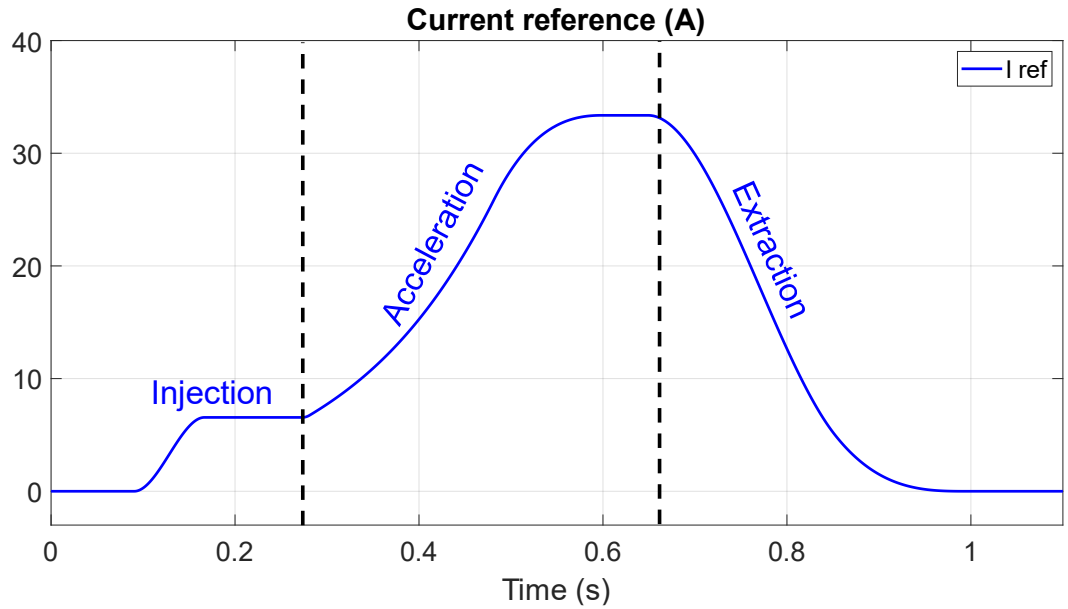


Figure 71: Current reference for mini-POPS-B

The Mini-POPS B is thus a reduced-power version of POPS. The saturation of the magnet and magnetic field measurement are supplementary differences. The ECU organisation is the same than the full-power system.

IV.1.b. Initial RST Control

The initial control of mini-POPS-B (Figure 73) is done using:

- a RST controller for the current loop, (A)

- a RST controller for the voltage loop, (B)

- a current balance for the converter legs, (C)

- a voltage regulation for the voltage bridge divider. (D)

Two heuristic strategies act on the (C) block in order to balance the currents in the interleaved inductances and voltage bridge divider.

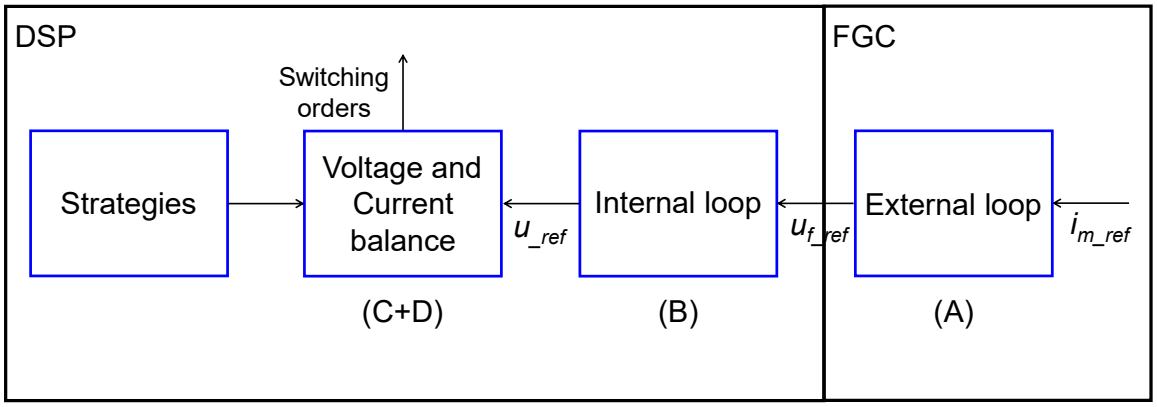


Figure 72: mini-POPS-B general control scheme

This initial RST-based control is described using EMR (Figure 73) in order to better analyse the differences between this control scheme and the inversion-based one. Compared to the new developed control (see Figure 28), the initial RST-based control has:

- no measurements of the disturbances for both control loops (instead of explicit compensations of all disturbance inputs),

- 2 control loops (instead of 7 control loops including the ones of the current balance with a regulation to 0A),

- a global strategy acting on the DC/DC control (instead of distribution of strategy at the inversion of the coupling elements).

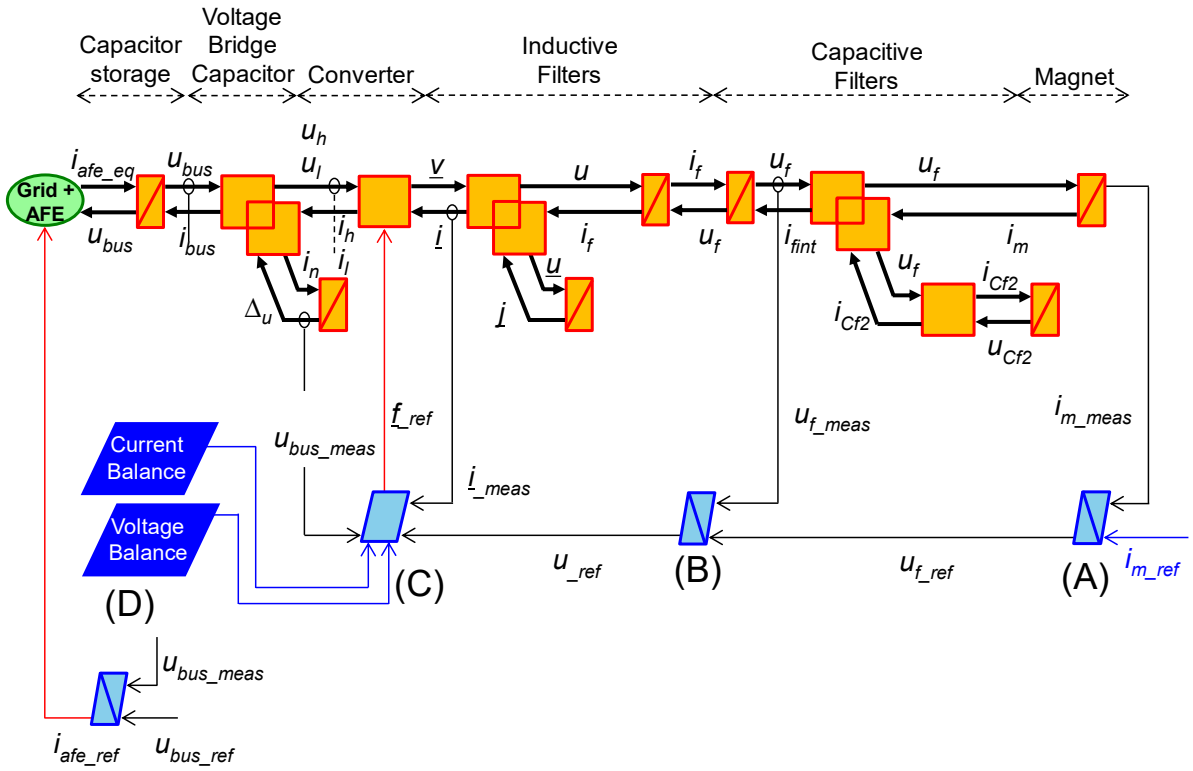


Figure 73: Initial control of mini-POPS-B

IV.1.c. Hybrid control

A first change of the initial control is proposed. The external RST loops (A and B) are kept, and the inversion-based control of the internal loop are integrated as well as the strategy. This hybrid control (Figure 74) aim to study the impact of the inversion-based control of the inner loops and the related new strategy.

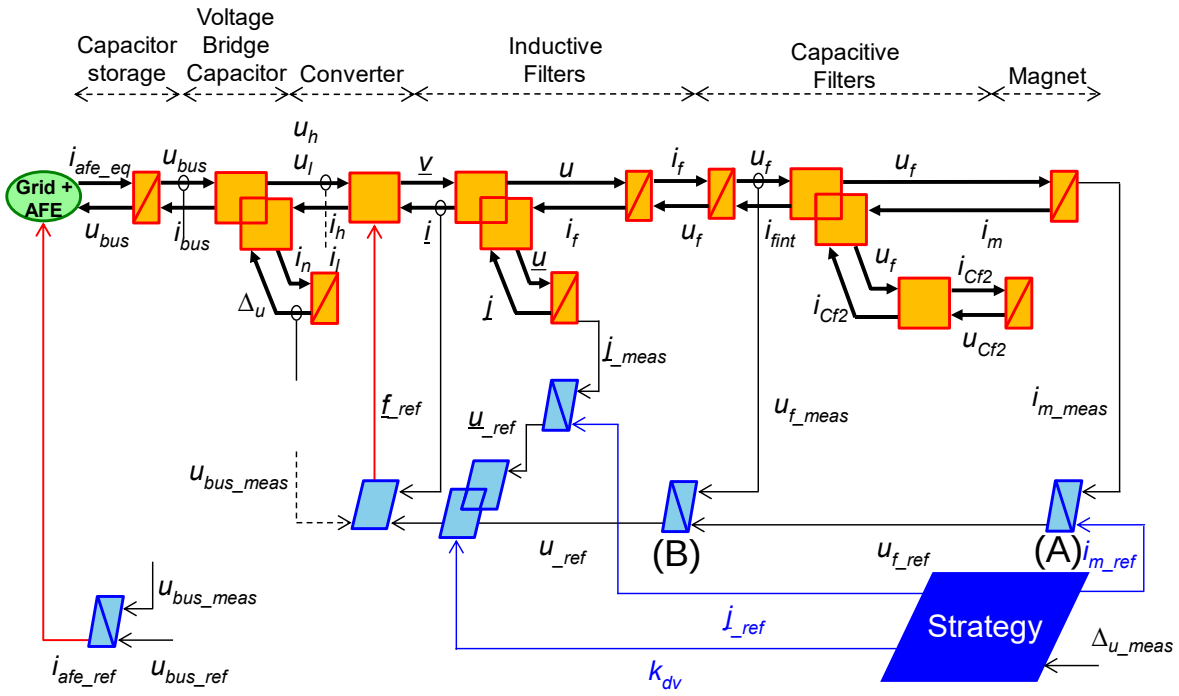


Figure 74: Hybrid RST control of mini-POPS-B

The current i_m in the magnet follow the reference with a flat top of 33A (Figure 75.a). The current error (Figure 75.b), defined as ($i_{m_ref} - i_{m_meas}$), almost satisfies the specification of maximum 100 ppm. The current measured is going slightly above the threshold during the high dynamic variation of the reference. This is noticeable at the beginning, the current overshoots twice, by 0.04 A at the start and the end of the 1st ramp, at the start of the 2nd ramp the current overshoots by 0.04 A and by -0.04 A at the start of the flat top. The last overshoot can be ignored since the cycle is finished, and the particle is not in the accelerator anymore. During the flat tops the current stays slightly above the error margin. The current measured is quite noisy and the quantification increase the measurement error. The results are obtained with the current and not the magnetic field which cannot be measured with accuracy. The differences of this reduced-scale power systems with the full-scale POPS can explain the difference of performances. As the PhD objective is not to improve the initial RST-based control, these performances are kept as reference for the other control tested on this platform.

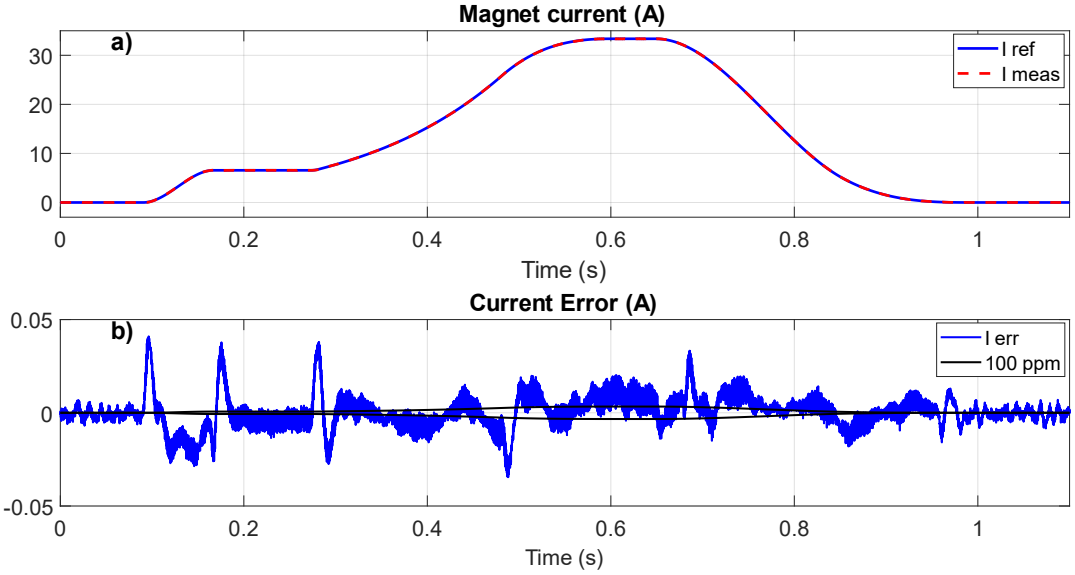


Figure 75: Experimental results of mini-POPS-B using hybrid control a) current in the magnet with its reference, b) error of the current with an error of 100ppm.

Figure 76.a shows the current i_1 to i_6. The effect of the PWM is noticeable, all currents have a ripple of 333Hz, with a maximal amplitude of 2A during the ramping. The circulating currents $\underline{j}$ (Figure 76.b), are close to 0 indicating a balanced current. When the current is in steady state, $\underline{j}$ is near 0. During the high dynamics, there can be a difference of up to 2A. These results highlight the interest of the proposed control to balance the current legs and limit the circulating current $\underline{j}$.

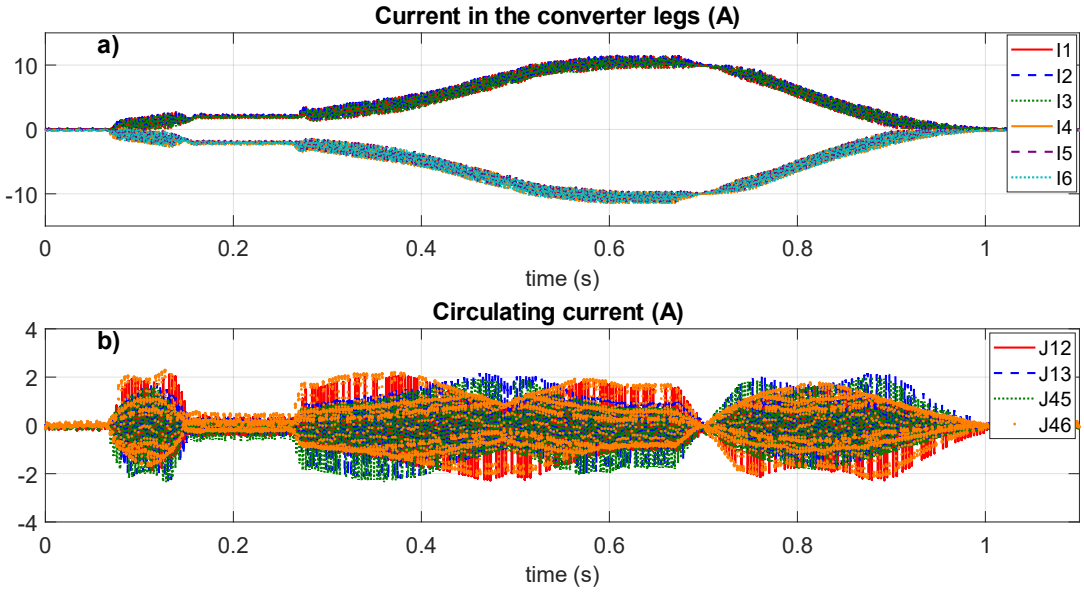


Figure 76: Experimental results using hybrid control a) current in the converter legs, b) circulating currents j

The voltages across the capacitors bridge C_h and C_l are stable and do not diverge, they remain around the same value. A discharge is noticeable when the pulse begins, after which their voltage returns to 25 V at the end of the cycle (Figure 77.a).

The voltage starts balanced. A slight imbalance appears at the start of the cycle, but stays low (Figure 77.b). The maximal difference between the two voltages is 0.7 V(=2.8%) during the high dynamics, the voltage difference reaches 0V at the end of a cycle. These results highlights the performance of the proposed strategy to keep the balance in the capacitor bridge.

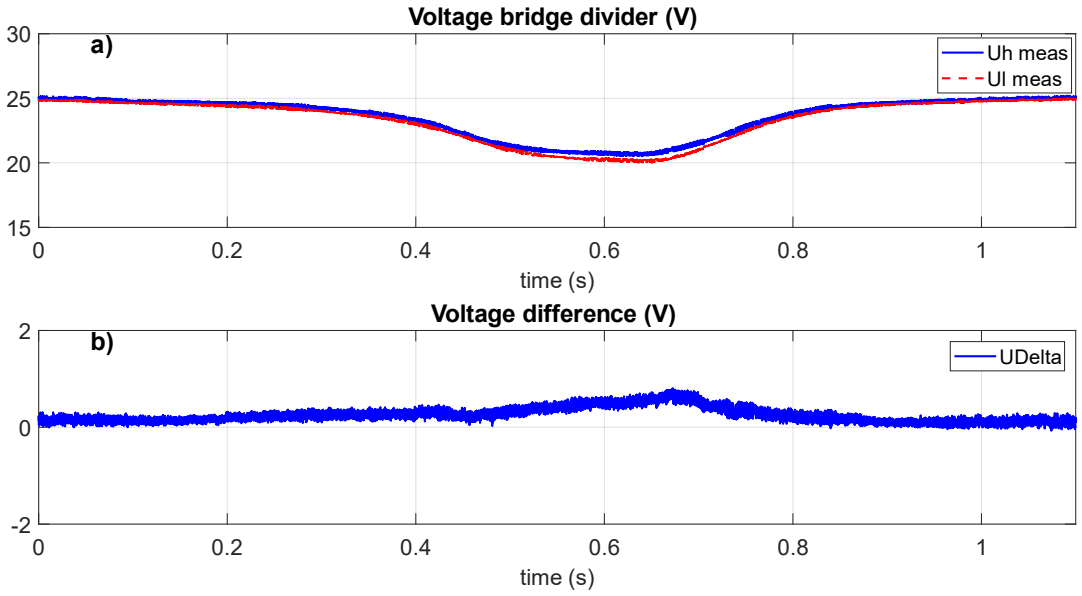


Figure 77 : Experimental results using hybrid control a) u_h and u_l voltage, b) voltage difference

The voltage u_{bus} of the charging storage capacitor changes with the current demand, when i_m ramps up, u_{bus} is discharging and when i_m is descending, u_{bus} is charging (Figure 78.a). At the end of the cycle u_{bus} is reaching 50V and is ready for another cycle. The developped control thus leads to use the energy in the capacitor while recovering its initial value at the end of a cycle.

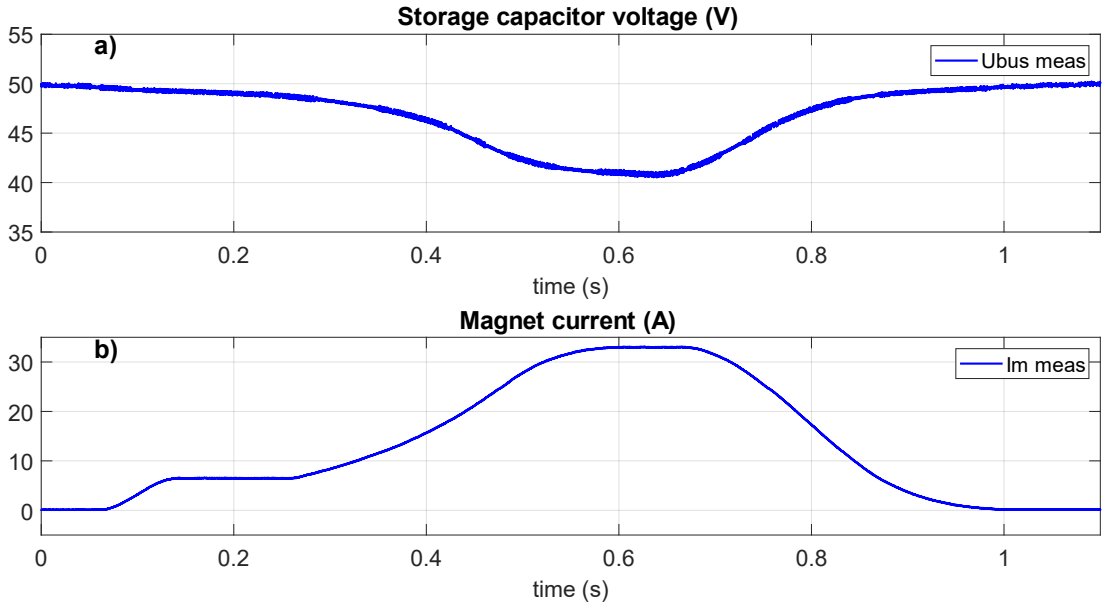


Figure 78: Experimental results using hybrid control a) u_{bus} voltage, b) current in the magnet.

A hybrid control has been proposed with RST controllers for external loops, and the inversion-based control for internal loops. The experimental results demonstrate that the inversion-based internal control leads to a real balance of the inductor currents, a relevant regulation of capacitor voltage of the bridge divider and the recovery of the initial values of the floating storage capacitors.

IV.1.d. Results of the inversion-based control

Compared to the previous control, the voltage and current balance are kept, but the external loops are change with PI controller and an equivalent PI controller for the external RST loop.

The maximal control structure (Figure 79), is what should have been theoretically implemented for mini-POPS-B. However, due to hardware restriction, the flatness control and the measurement of i_{cf2} were not done. The FGC3 has a RST controller hard coded and cannot be changed. To overcome this issue an equivalent PI controller is calculated. For i_{cf2}, it can be estimated from the voltage of the magnet u_f by using a function. The current i_f is not directly measured but is estimated by adding the 3 positive currents i_1, i_2 and i_3 measured form the converter legs (Figure 80).

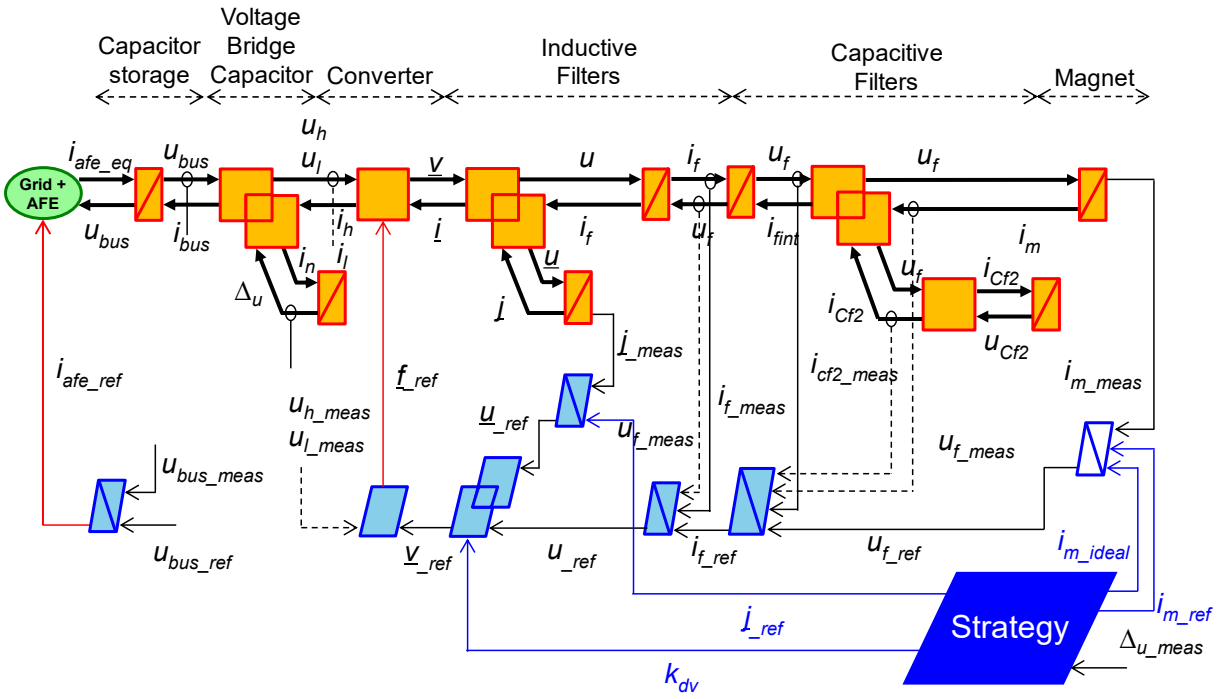


Figure 79: Initial inversion-based control of mini-POPS-B

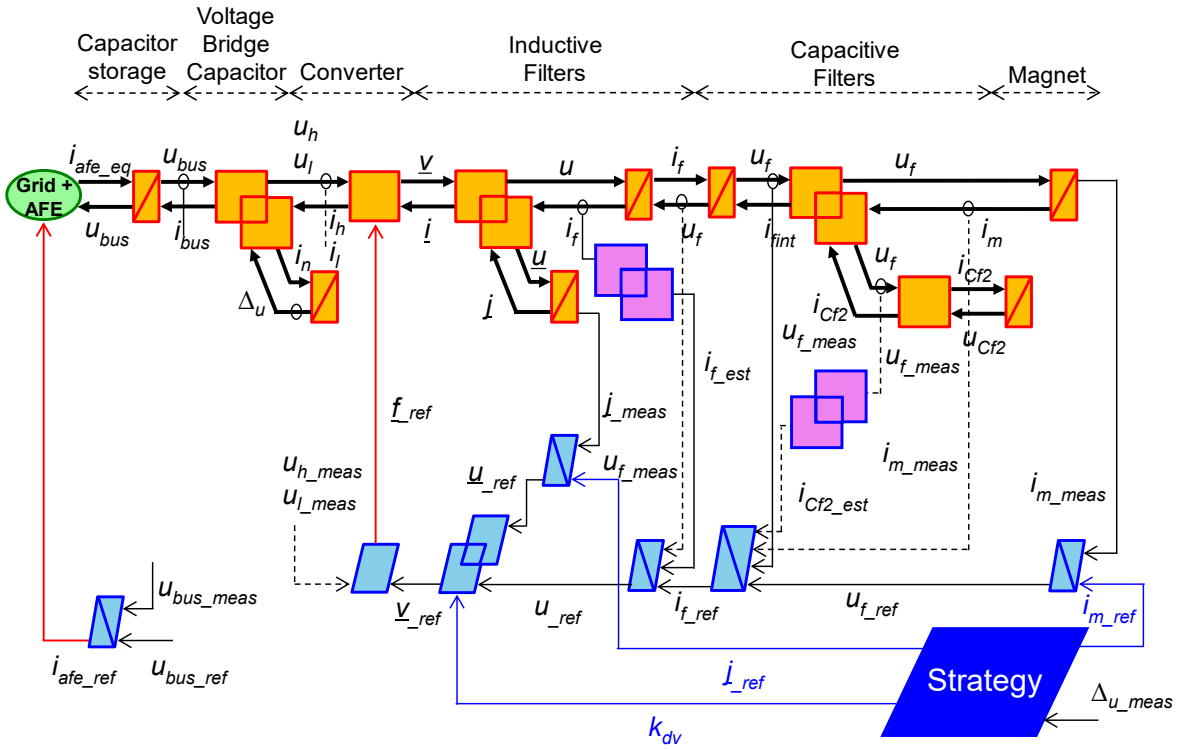


Figure 80: implemented inversion-based control of mini-POPS-B

The current i_m in the magnet follow the reference (Figure 81.a). The current error (Figure 81.b) almost satisfies the specification of maximum 100 ppm. The current measured is going slightly above the threshold during the high dynamic variation of the reference. This is noticeable at the beginning, the current overshoots by 0.03 A at the start of the 1st ramp. At the start of the 2nd plateau and by 0.02A. The last overshoot can be ignored since the cycle is finished, and the particle is not in the accelerator anymore. During the 1st flat top, the current stays slightly above the error margin and below it for the 2nd flat top. The current measured is quite noisy and the quantification increase the measurement error. Compared to the hybrid control with the initial RST controller as external loops (Figure 73), the current errors are of same magnitude due to the difference of the reduced-scale mini-POPS-B with POPS B as explained in the previous sub-section.

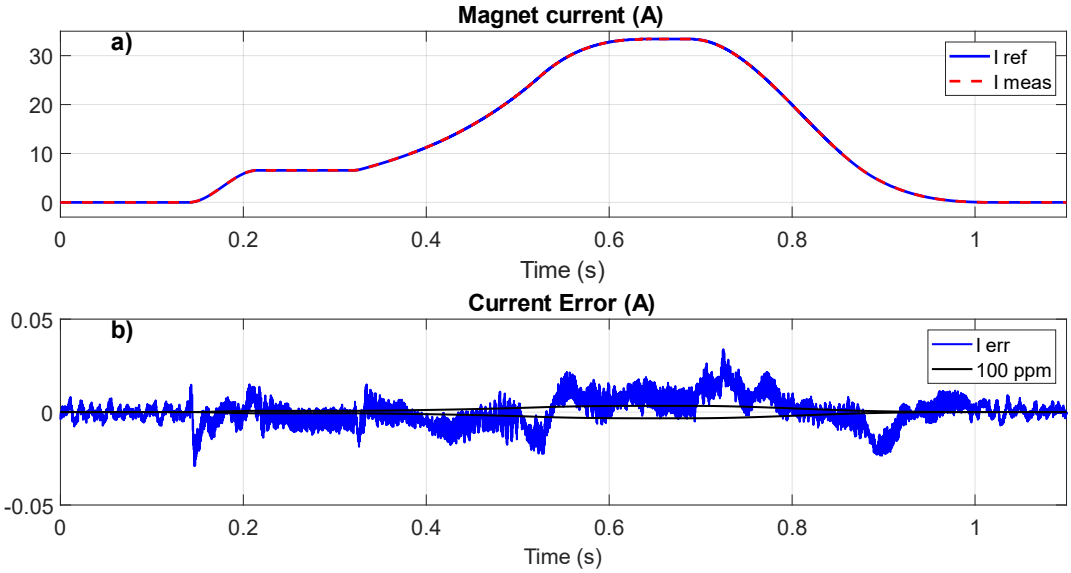


Figure 81: Experimental results of mini-POPS-B using inversion-based control a) current in the magnet with its reference, b) error of the current with an error of 100ppm.

Figure 82.a shows the current i_1 to i_6. The effect of the PWM is noticeable, all currents have a ripple of 333Hz, with a maximum amplitude of 2A during the ramping. The circulating currents $\underline{j}$ in the converter legs (Figure 82.b), are balanced as they are close to 0. During the high dynamics, there can be a difference of up to 2.5A. The results are similar to the previous part, it is normal since it is the same internal inversion-based control

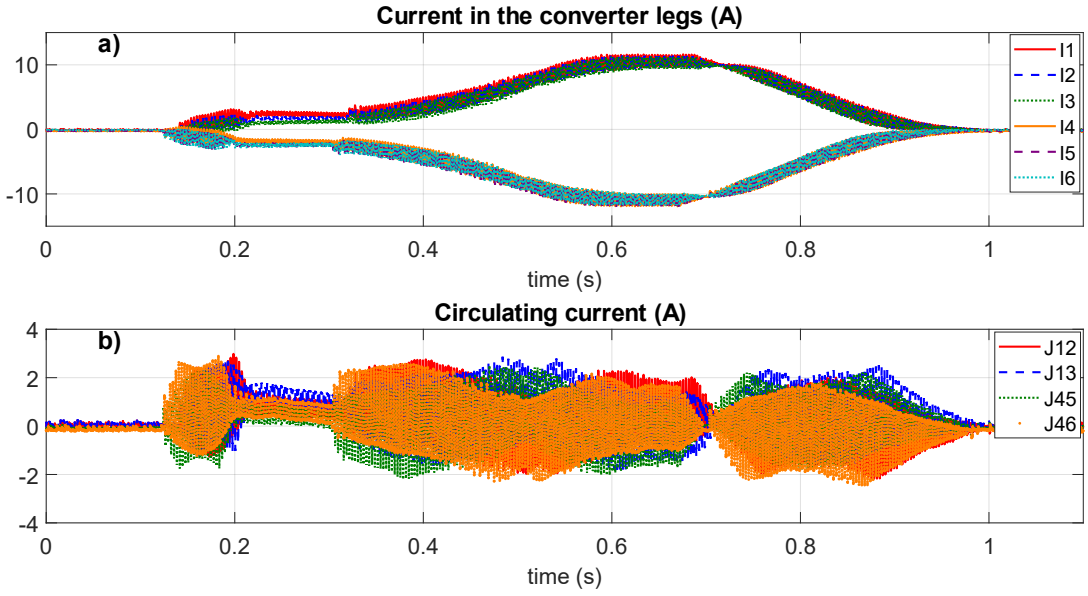


Figure 82: Experimental results using inversion-based control a) current in the converter legs, b) circulating currents j.

The voltages across C_h and C_l (Figure 83.a) and the balancing of the bridge (Figure 83.b) gives the same results as the previous section since the control is the same.

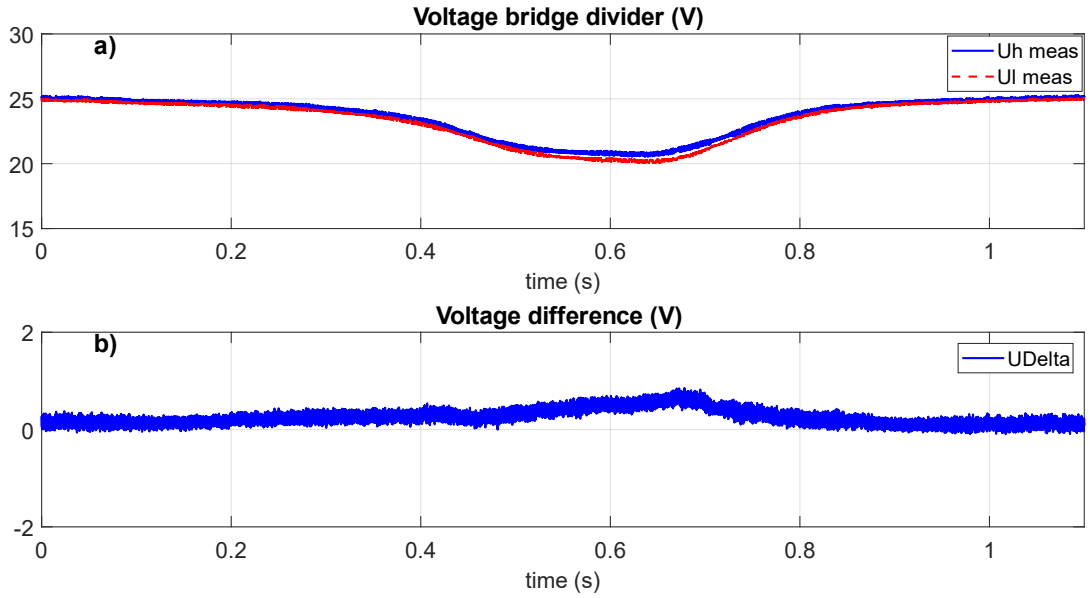


Figure 83: Experimental results using inversion-based control a) u_h and u_l voltage, b) voltage difference

The discharge of the storage capacitor (Figure 84), has the same discharge and charge shape as the previous section, it is normal since the control is the same internal control loops.

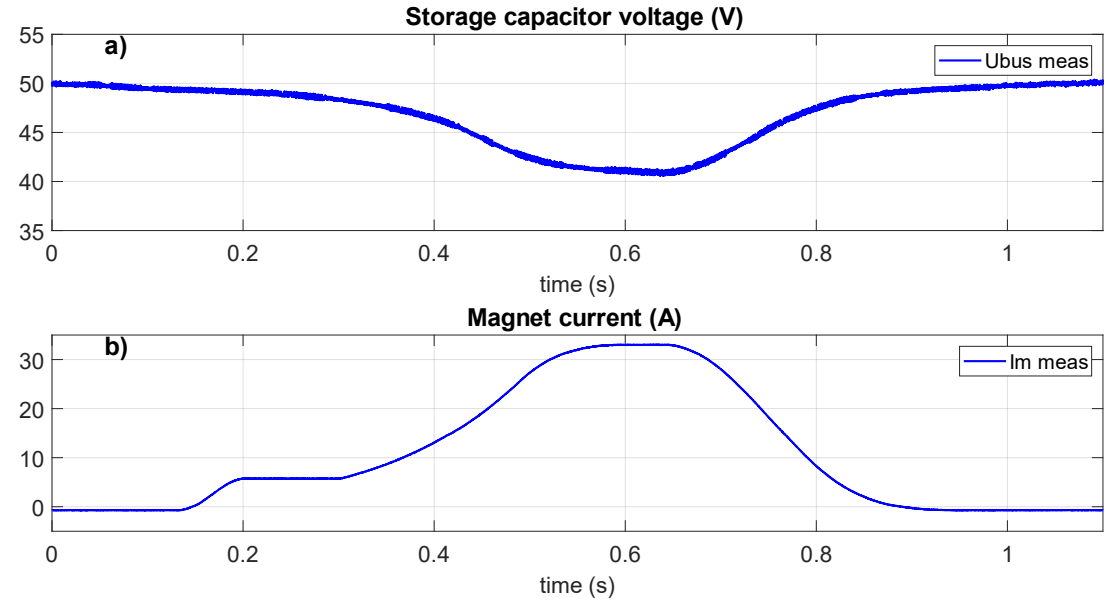


Figure 84 : Experimental results using inversion-based control a) u_{bus} voltage, b) current in the magnet.

Both the hybrid RST and inversion-based control strategies demonstrate relevant performance, achieving accurate current tracking close to the 100 ppm specifications despite minor overshoots during dynamic phases. The system remains stable overall, with well-balanced voltages and acceptable current

ripple, confirming the effectiveness of the implemented control approaches. These results validate the feasibility of the inversion-based architecture related to practical hardware constraints.

The experimental results show that the RST control provides slightly better performance than the inversion-based control, with a lower error during the flat-top phase. However, the flatness control has not been implemented. The inversion-based control, on the other hand, offers a more systematic controller synthesis. Simulation results indicate that when the inversion-based control is combined with the flatness control, the performance is improved and meets the specified requirements.

IV.2. Experimentation on mini-POPS

IV.2.a. Description of mini-POPS

The mini-POPS is a 1 to 100 scaled-down version of the POPS converter, developed in 2008 to assess the feasibility of the POPS power converter for use in the Proton Synchrotron particle accelerator. Mini-POPS is a converter composed of 2 unitary converter, one connected to the grid and the other with a floating capacitor. It keeps the same values of resistances, inductances and capacitances. The power is scaled by a factor 10000. The layout of mini-POPS is shown below (Figure 85).

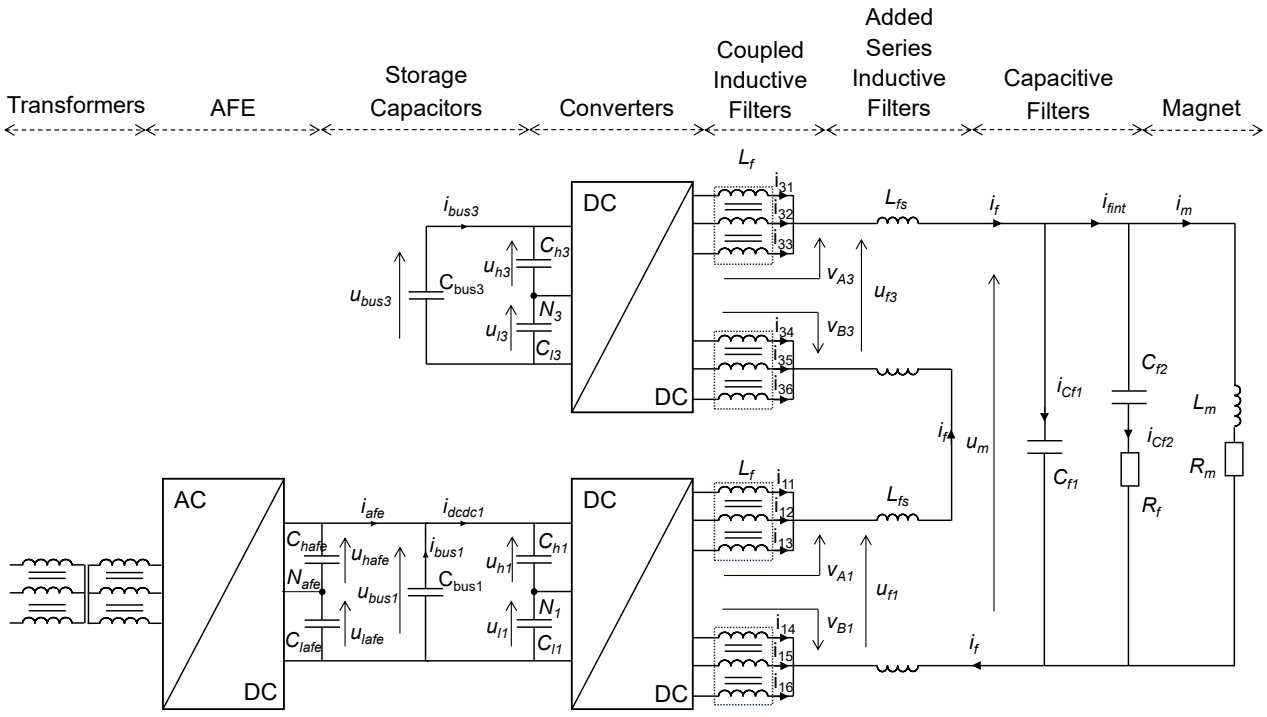


Figure 85: Layout of mini-POPS.

The mini-POPS uses the same AFE, DC/DC converters, inductors, capacitive filters and magnet as mini-POPS-B. Here, the floating capacitor is 2 times smaller than the charger, In POPS the storage capacitors have all the same value. The addition of a DC/DC converter allows it to go higher in power. This supplementary converter requires the addition of another DSP. The added DSP receives a voltage reference from the charger to control the floating converter. The DSPs are connected via a DAC (Digital

to Analog Channel) to receive the output voltage reference (Figure 86). The charger DSP also reads the floating capacitor voltage via Burndy cables, it is used during the precharge and in the running phase to ensure the floating capacitor is at 50V at the start and the end of a cycle.

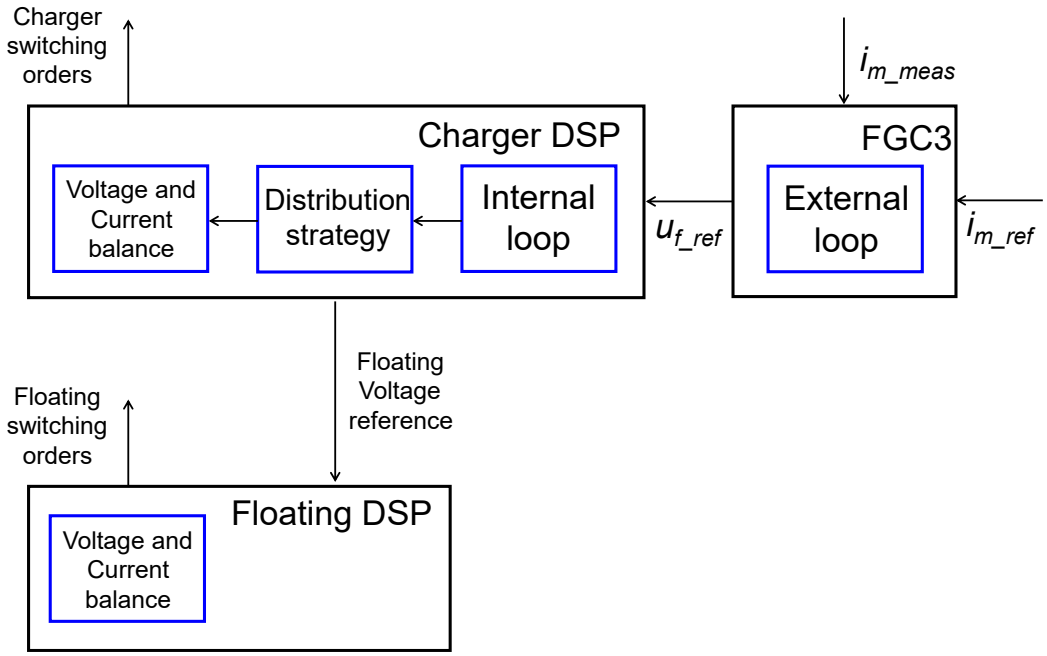


Figure 86: Simplified architecture of mini-POPS

The reference used is the same as previous but the amplitude is higher with a current peak of 45A (Figure 87). The regulation of the experimentation is done with the current and not the magnetic field.

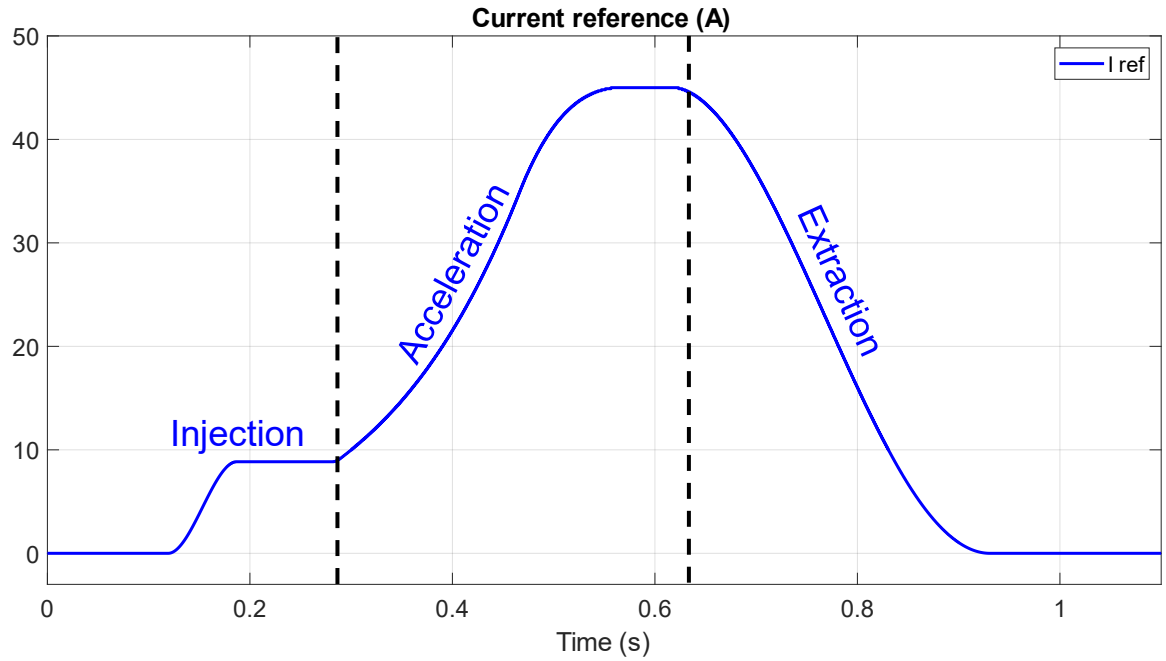


Figure 87: Current reference for mini-POPS

IV.2.b. Mini-POPS hybrid control

The hybrid RST control implemented in mini-POPS (Figure 88) is made up of:

- a RST controller for the current loop,

- a RST controller for the inner loop,

- a voltage reference distribution,

- a current regulation of the 2 converter legs using inversion-based approach,

- a voltage regulation of the 2 storage capacitor using inversion-based approach.

It thus combines the initial control (2 external loops) and the inversion-based control (voltage and current balance).

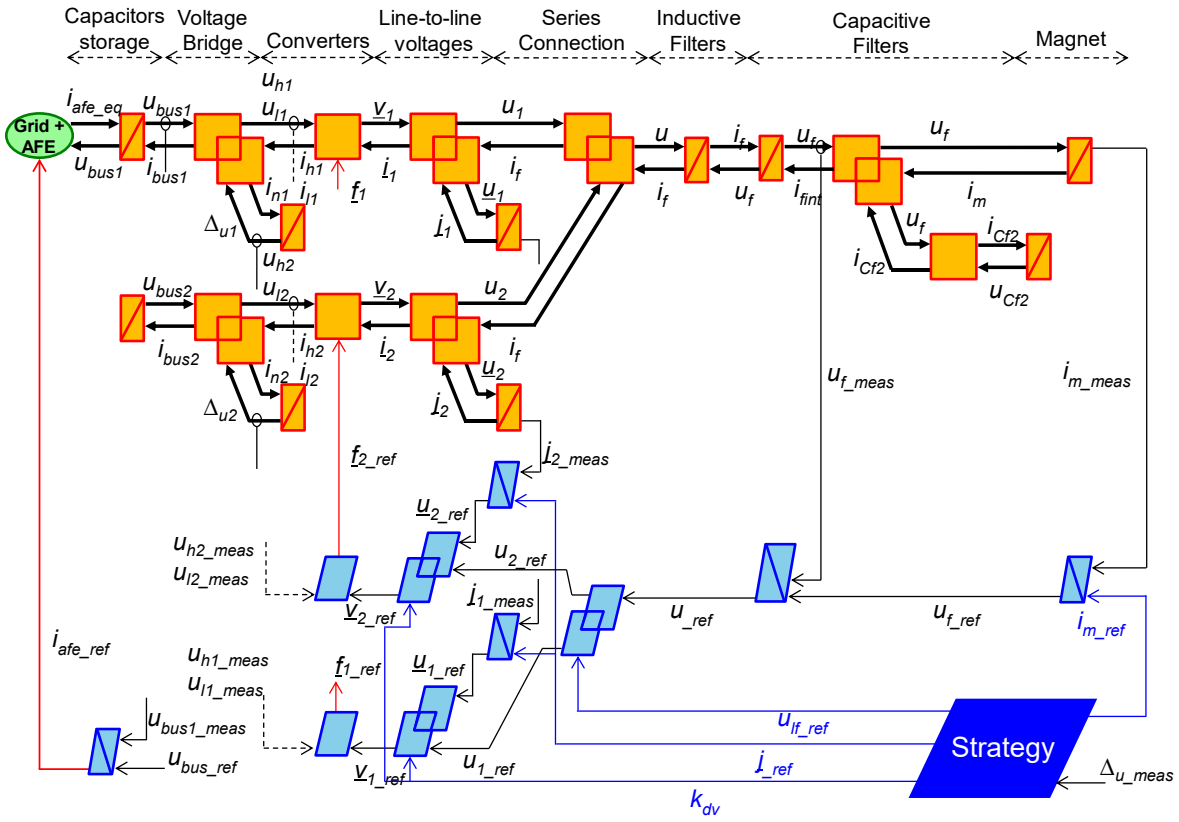


Figure 88: Hybrid control implemented in mini-POPS

The current i_m in the magnet follow the reference with a flat top of 45 A (Figure 89.a). The current error (Figure 89.b), satisfies the specification of maximum 100 ppm except at 0.45 s. The current measured is going slightly above the threshold during the high dynamic variation of the reference and the tracking of the current rising. This is noticeable at the beginning, the current overshoots by -0.05 A, then by 0.05 A at the start of the 1st ramp and at the end. At the start of the 2nd ramp there is a slight undershoot and overshoot by -0.02 A and 0.02 A. The major issue is during the 2nd ramp at 0.45 s when the current is rising and approaching 35 A. An error of -1.3 A appears. Simulations have shown that this error is due to a non-optimal distribution strategy. The charger capacitor is too solicited and cannot provide the required power, which leads lead to a saturation of the switching function. The scale down of the reduced power system therefore led to limitation where there are none on the full-scale system. This overshoot should be solved in future works. However, despite this issue, the controller catches up to the flap top and provides a flat top following the specifications. The last overshoot can be ignored since the cycle is finished. To solve the issue, increasing the capacitance of the floating and asking more energy from it could solve the issue.

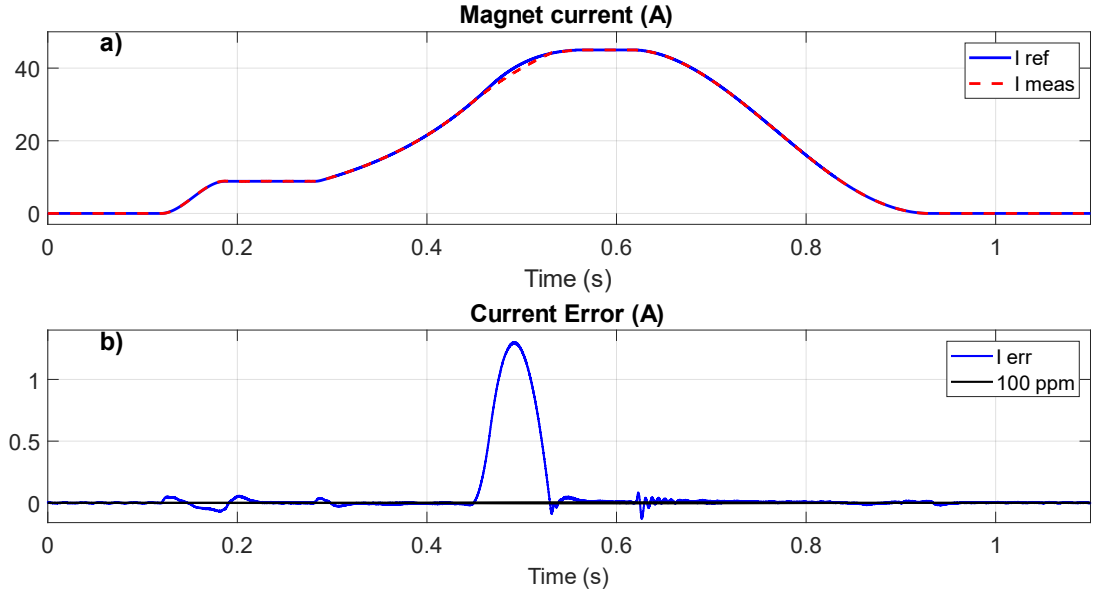


Figure 89: Experimental results of mini-POPS using hybrid control a) current in the magnet with its reference, b) error of the current with an error of 100ppm.

Figure 90.a shows the current in the charger legs i_{11} to i_{16}. The effect of the PWM is noticeable, all currents have a ripple of 333 Hz, with a maximal amplitude of 2 A during the ramping. The circulating currents $\underline{i}$ (Figure 90.b), are balanced, they are near 0 in steady state. The highest peaks are during the high dynamics, there can be a difference of up to 2.5 A. The current ripple is lower during the current descent since the floating converter is recharging and is taking most of the voltage.

For the floating converter (Figure 91), the same results are obtained with a relevant distribution of the 6 current and a minimisation of the circulating currents.

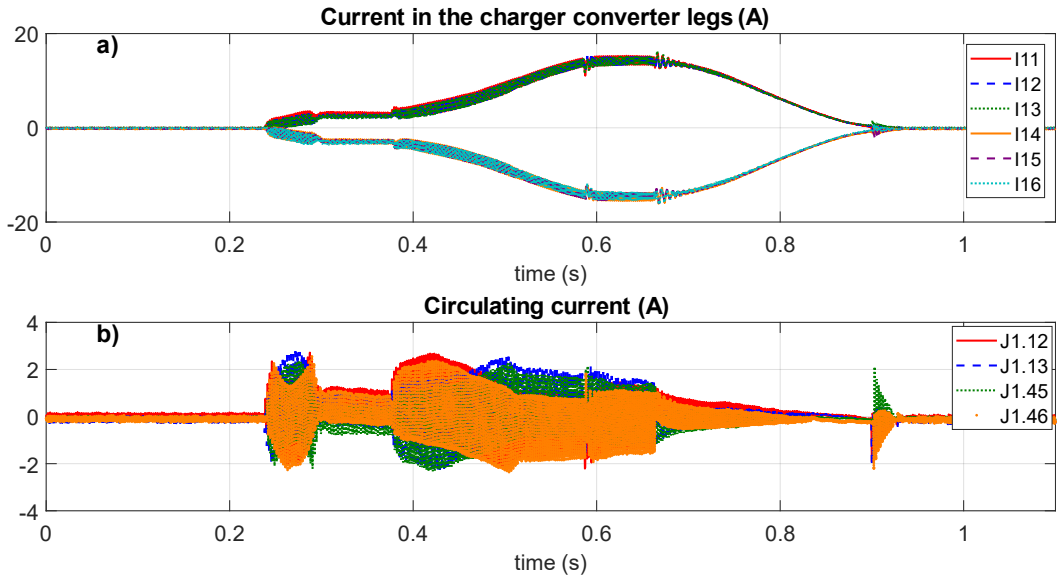


Figure 90: Experimental results using hybrid control a) current in the charger converter legs, b) circulating currents j.

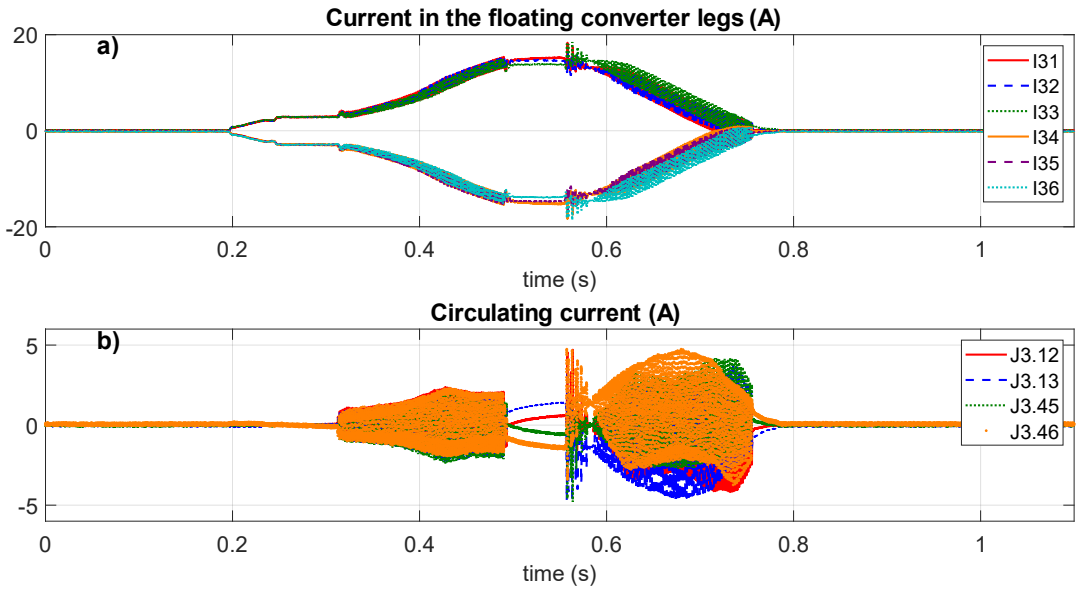


Figure 91: Experimental results using hybrid control a) current in the floating converter legs, b) circulating currents j.

Once again, the inversion-based control of the inner loop leads to the right performance as balanced currents are obtained. The extension from 1 module (mini-POPS-B) to 2 modules (mini-POPS) is easily achieved.

The voltages across the charger capacitors C_{h1} and C_{l1} are stable and do not diverge, they remain around the same value. A discharge is noticeable when the pulse begins, after which their voltage returns to 25 V at the end of the cycle (Figure 92.a).

The voltage starts balanced. A sight imbalance appears at the start of the cycle, but stays low (Figure 92.b). The maximal difference between the two voltages is 0.5 V(=2%) during the high dynamics, the voltage difference reaches 0 V at the end of a cycle.

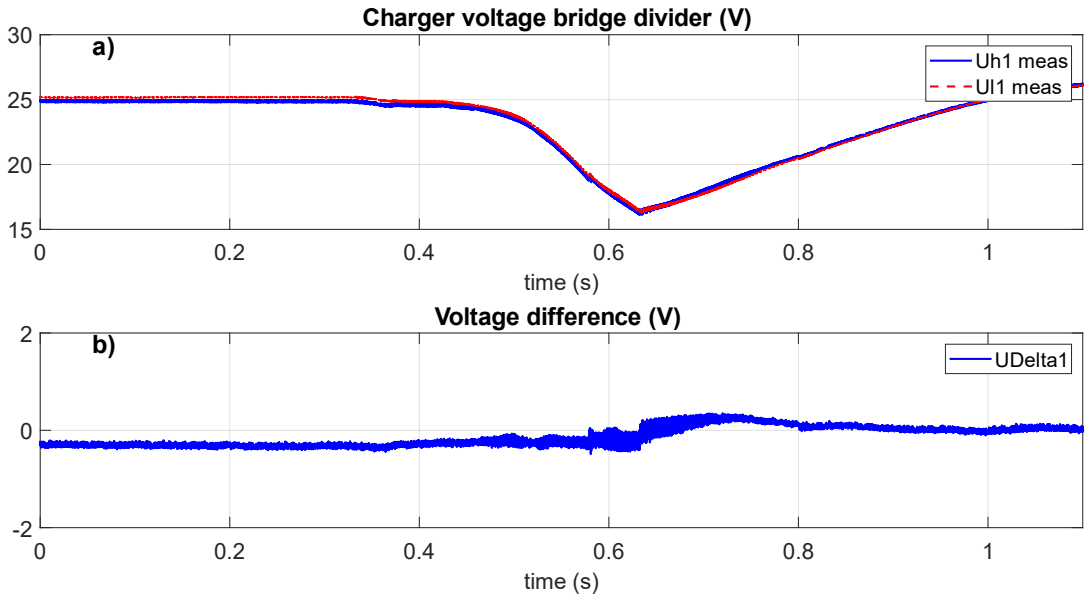


Figure 92: Experimental using hybrid control a) u_{h11} and u_{l11} voltage, b) charger voltage difference

The voltages across the floating capacitors C_{h3} and C_{l3} are stable and do not diverge, they remain around the same value. A discharge is noticeable when the pulse begins, after which their voltage returns to 25 V at the end of the cycle (Figure 93.a). The voltage starts balanced. A sight imbalance appears at the start of the cycle, but stays low (Figure 93.b). The maximal difference between the two voltages is -1 V (=4%) during the high dynamics, the voltage difference reaches 0V at the end of a cycle.

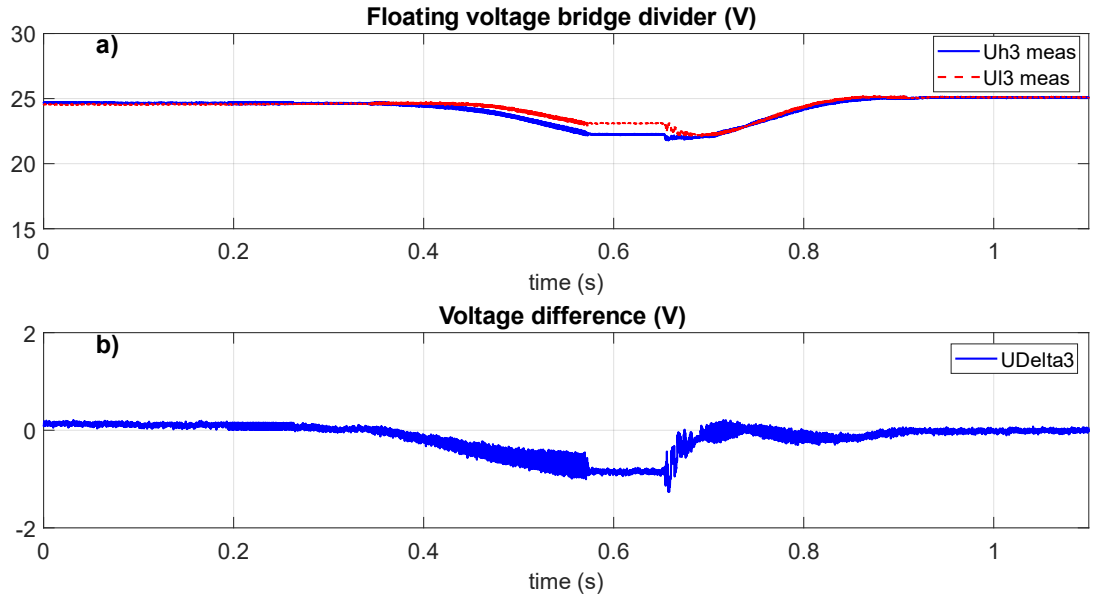


Figure 93: Experimental results using hybrid control a) u_{h13} and u_{l13} voltage, b) floating voltage difference

The voltages of the charging storage capacitor u_{bus1} and of the floating storage capacitor u_{bus3} changes with the current demand, when i_m ramps up, the voltages are discharging and when i_m is descending, u_{bus1} and u_{bus3} are charging (Figure 94.a). At the end of the cycle the 2 storage capacitors reach 50 V and are ready for another cycle.

Due to the system is high resistance and with the high capacitance value of C_1, u_{bus1} is getting the most discharge. Its voltage does not reach the threshold of 30 V, which follows the specifications.

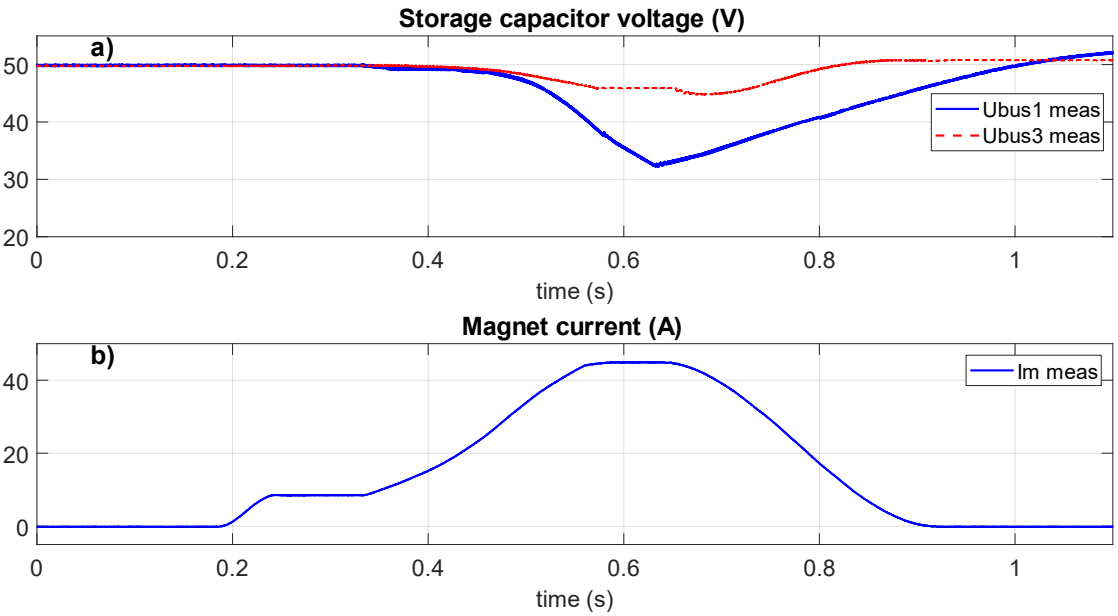


Figure 94: Experimental results using hybrid control a) voltage of the charger and the floating capacitor, b) current in the magnet.

The inversion-based control of the inner loops of the 2 modules also leads to the balance of the voltage and the low deviations.

IV.2.c. Inversion-based control results

In this section the complete inversion-based control is now applied (Figure 95), especially with the inversion-based control of the external loop.

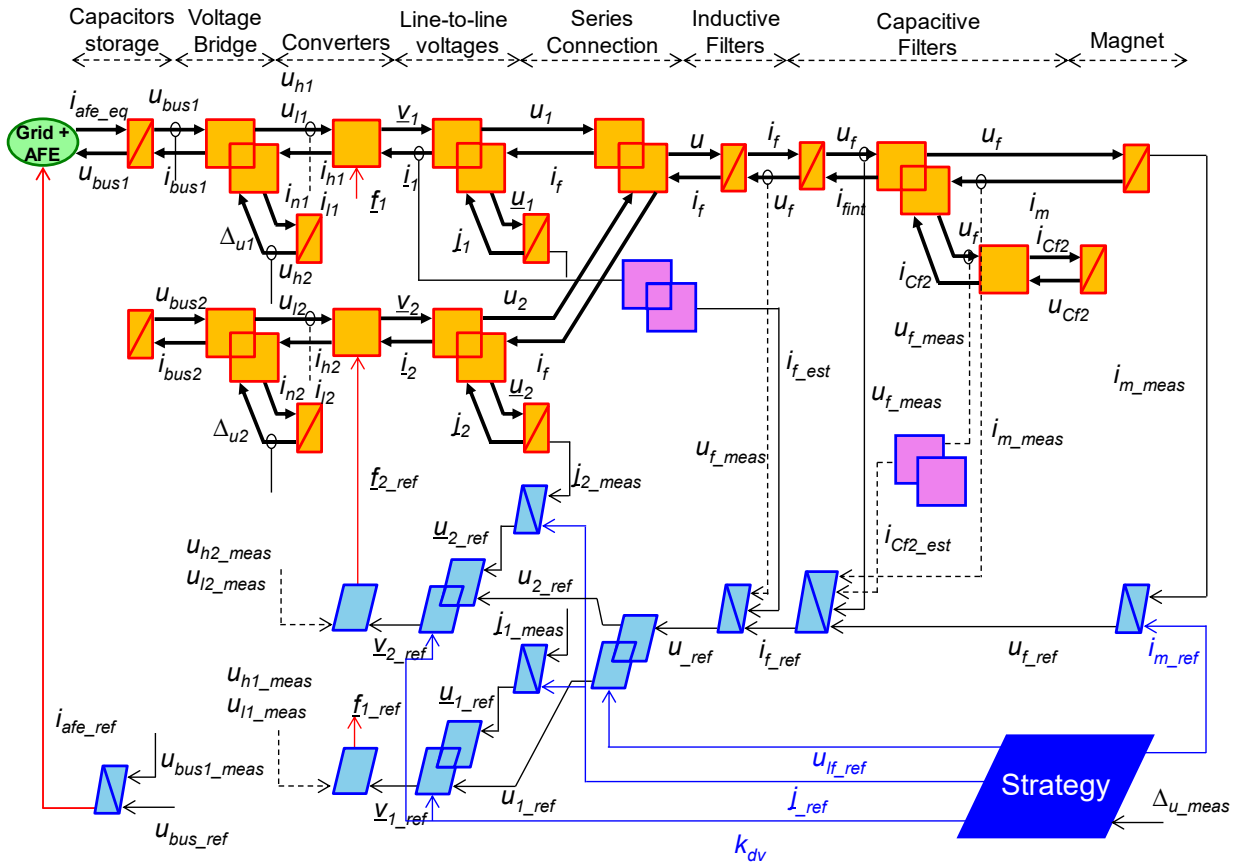


Figure 95: implemented inversion-based control of mini-POPS

The same results are obtained as those obtained with the hybrid RST control. The error at 0.45 s is not associated with the external loop.

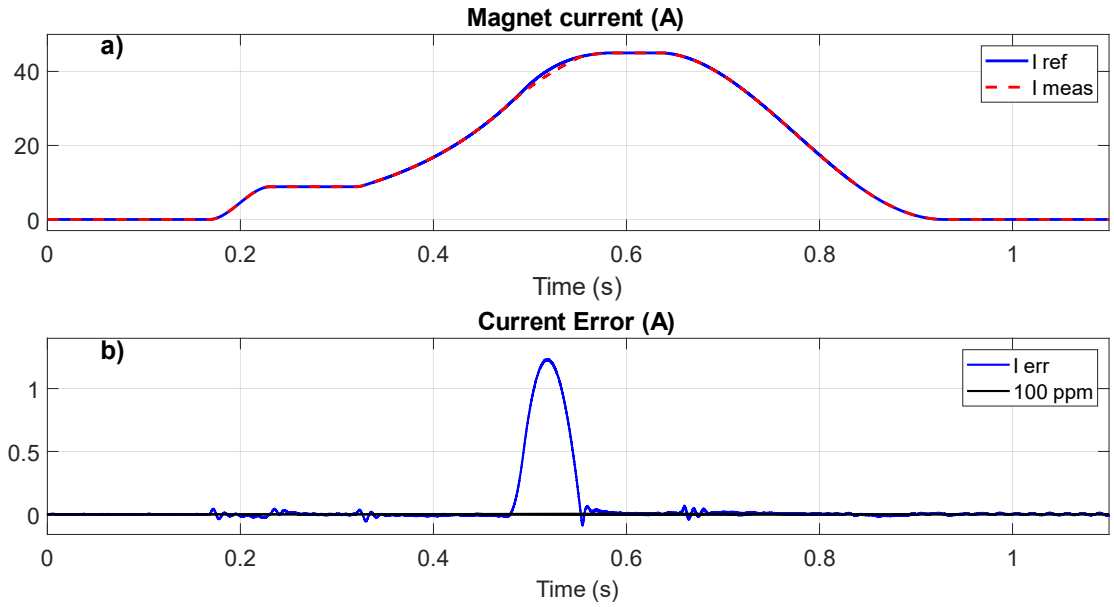


Figure 96: Experimental using inversion-based control a) current in the magnet with its reference, b) error of the current with an error of 100ppm.

For the currents of the charger (Figure 97), similar results are obtained.

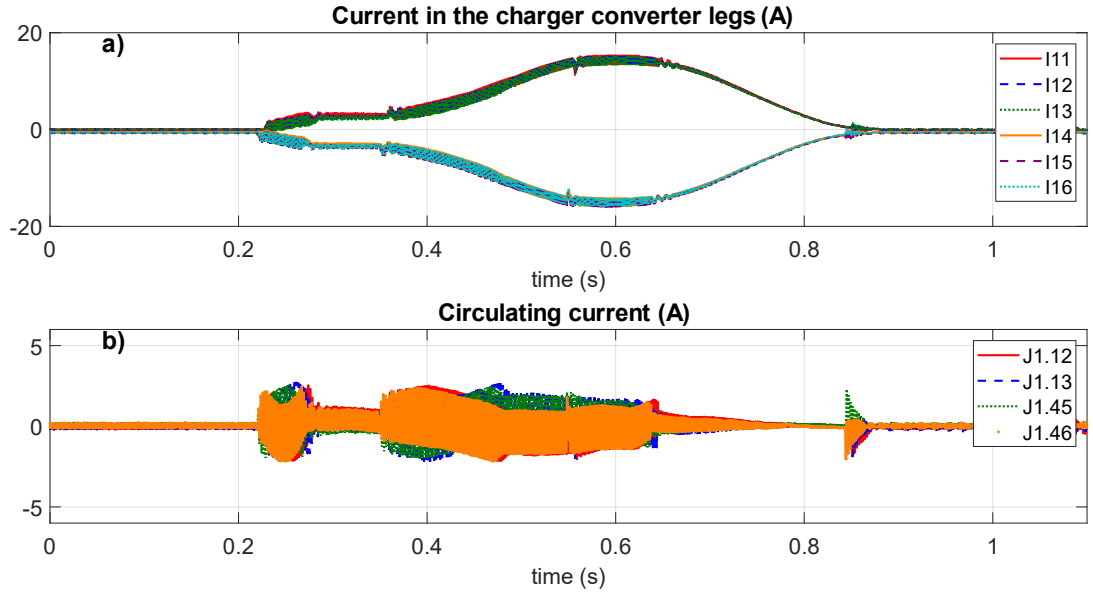


Figure 97: Experimental results inversion-based control a) current in the charger converter legs, b) circulating currents j.

The current of the floating i_{31} to i_{36} (Figure 98), have similar results, even if there is a slight error between the currents.

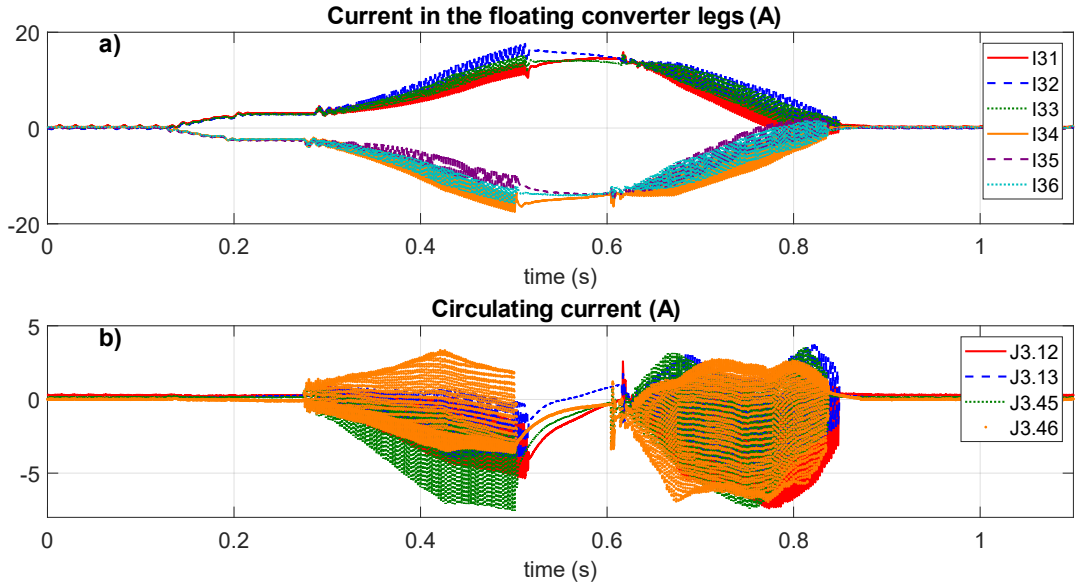


Figure 98: Experimental results using inversion-based control a) current in the floating converter legs, b) circulating currents j.

The voltages across C_{h1} and C_{l1} are (Figure 99) gives the same results as the previous section and are balanced.

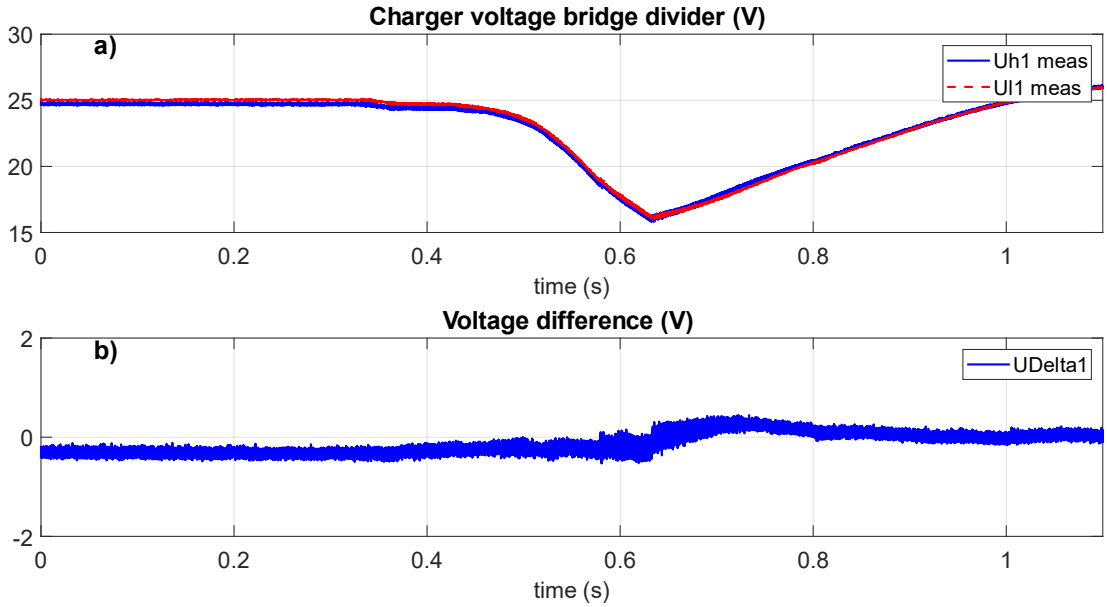


Figure 99: Experimental results using inversion-based control a) u_{h1} and u_{l1} voltage, b) charger voltage difference

The voltages across C_{h3} and C_{l3} (Figure 100) give the same results as the previous section and are balanced.

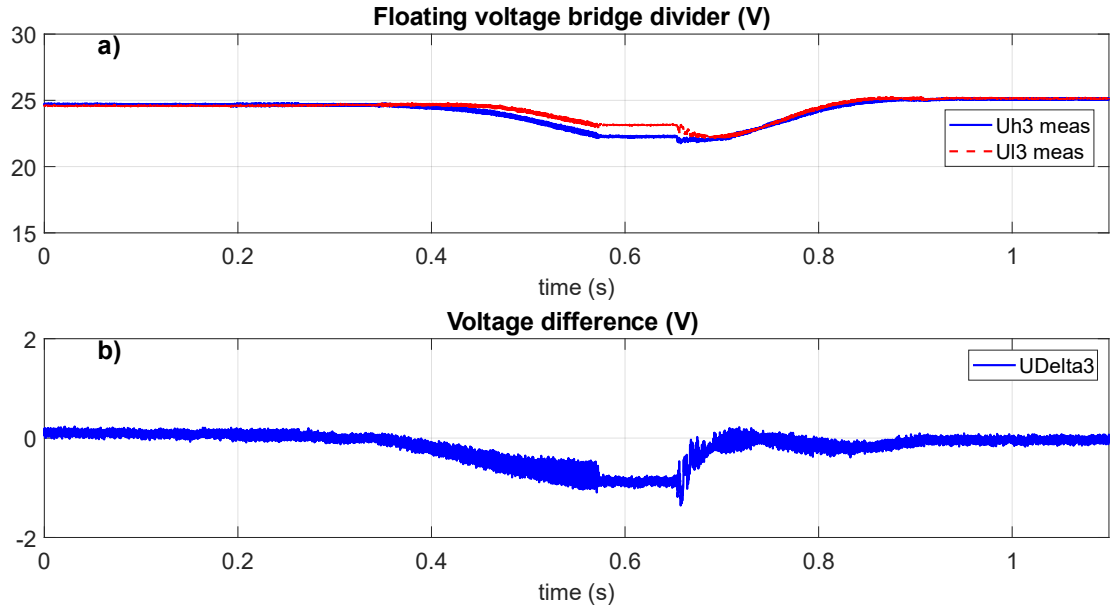


Figure 100: Experimental results using inversion-based control a) u_{h3} and u_{l1} voltage, b) floating voltage difference

The voltages of the charging storage capacitor u_{bus1} and of the floating storage capacitor u_{bus3} gives the same results as the previous section.

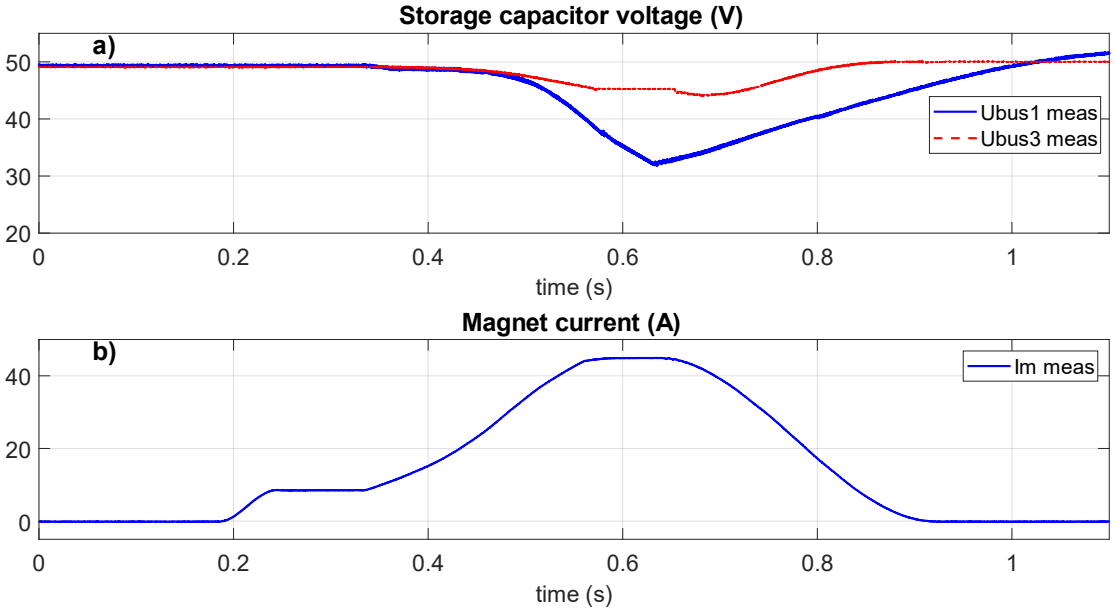


Figure 101: Experimental results using inversion-based control a) u_{bus} voltage, b) current in the magnet.

IV.2.d. Conclusion of the experimental results

The inversion-based control of the inner control loops gives us valuable performances by showing us balanced currents in the converter legs and a balanced voltage.

The hybrid control and the inversion-based control of the external loops gives us the similar results. The next step would be to implement the flatness control.

The hybrid results show that the RST control leads to results close to the required error margin. Some differences occur due to the difference of the reduced-scale set-up with the full-scale POPS. It falls when more variables are added and becomes much more complex and computing heavy. Meanwhile EMR allows to have a systemic description of the inside loops and variables to control which helps reduce potential disturbances between loops for complex systems.

The comparison of the results of both external control loops also highlights the strengths and limitations of each approach. The RST controller performs well in single loop configurations, offering high precision. However, as the number of variables increases, its complexity and computational demands increase too.

Experimental results obtained on mini-POPS composed of 2 unitary converters when POPS is composed of 6 unitary converters. But as demonstrated in Chapter III, EMR and inversion-based control offers a relevant flexibility to extend the results from the 2 converters to the complete system.

In contrast, EMR provides a more systemic representation of internal loops and controlled variables. This makes it better suited for complex systems, as it helps reduce interactions and disturbances between control loops. EMR is also modular and reduce development time when more modules are added. A key difference between the EMR approach and the one previously adopted for POPS lies in the control of current and voltage unbalance. The EMR methodology enables a more effective treatment of unbalance than the heuristic approach implemented in the existing controller.

Conclusion

This PhD addresses the control of one of the most demanding class of power electronic systems: pulsed power converters for particle accelerators. In the specific context of the Proton Synchrotron, the POPS system embodies a combination of high power, fast dynamics, strong internal coupling, and extremely stringent precision requirements. Ensuring accurate magnetic field tracking while managing internal energy exchanges and respecting operational constraints represents a complex control problem that goes beyond conventional industrial applications.

The work presented in this manuscript explored the use of the inversion-based control derived from Energetic Macroscopic Representation as an alternative to classical control strategies. The objective is not only to assess the feasibility of such an approach for POPS, but also to evaluate its potential benefits in terms of structure, flexibility, and performance, particularly in view of future accelerator requirements.

A first important contribution of this PhD lies in the detailed modelling of the POPS system using the EMR formalism for the model organisation. Starting from a unitary converter and progressively extending to the full architecture, the modelling approach made it possible to capture the energetic interactions between subsystems in a structured and physically meaningful way. Unlike purely mathematical models, the EMR emphasizes causality, energy flows, and the role of storage elements. This proved particularly valuable for a system such as POPS, where capacitive storage, inductive loads, and power converters are tightly coupled.

Based on this modelling framework, an inversion-based control structure is systematically derived. The resulting control organization reflects the physical structure of the system, with each control loop is associated with a clearly identified energetic objective. This contrasts with more traditional approaches, where control structures are often obtained through successive design steps that may obscure the link between the controller and the underlying physics. It can be noted that the extension from the unitary power converter to the complete POPS demonstrate the flexibility of the method. This property can be easily used for future extensions of POPS.

The proposed control strategy explicitly addresses several key objectives of the POPS system. First, it ensures ultra-accurate tracking of the magnet current, and therefore of the magnetic field, which remains the primary requirement for accelerator operations. Second, it manages the energy stored in the capacitor banks, ensuring that voltage levels remain within specified limits throughout the cycle. Third, it enforces internal balance constraints, such as the distribution of currents in interleaved inductances and the voltage balance of converter structures. By integrating these objectives within a unified control

framework, the inversion-based approach provides a coherent solution to a multi-variable and multi-constraint problem.

The performance of the proposed control is evaluated through extensive simulations. These simulations are conducted under demanding operating conditions, including high-current reference cycles and situations close to modulation limits. The results demonstrate that the inversion-based control is capable of achieving the required tracking precision (100 ppm) while maintaining stable internal behaviour. In particular, the control shows to effectively regulate capacitor voltages and suppress circulating currents, even in the presence of system non-linearities and coupling effects.

Beyond simulation, a significant part of this work is dedicated to experimental validation. The implementation of the control on reduced-scale platforms, mini-POPS-B and mini-POPS, provides valuable insight into practical aspects that cannot be fully captured in simulation. These include measurement noise, parameter uncertainties, digital implementation constraints, and real-time execution limits. The experimental results confirm the feasibility of the inversion-based control in real-time and highlight its robustness in realistic conditions. They also demonstrate that the control structure remains interpretable and tunable when implemented on actual hardware, which is a critical requirement in an operational environment such as CERN.

One of the notable advantages of the proposed approach is its flexibility. Because the control structure is directly derived from the system energetic organization, it can be adapted to different configurations or operating modes with limited redesign effort. This is particularly relevant in the context of future developments, where converter architectures are expected to evolve and where fault-tolerant operation becomes increasingly important. The inversion-based framework naturally supports the integration of additional control objectives, such as energy management strategies or fault-operation modes, without fundamentally altering the overall structure.

However, this work also highlights certain limitations and challenges associated with the inversion-based control. The derivation of the control structure relies on an accurate and sufficiently detailed models of the subsystems. While EMR provides a systematic way to organise such models, the modelling effort can become significant for large-scale systems like POPS. In addition, the implementation of the maximal control structure may lead to a high number of control loops, which must be carefully managed to ensure stability and practical feasibility. These aspects must be considered when evaluating the trade-offs between performance, complexity, and implementation effort. In the short term, the coefficients of the controllers in the experimental could be tuned more finely to have

better results. A strict comparison between the initial RST control and the inversion-based control could be done. The issue of the voltage distribution can also be worked on to remove the error due to saturation.

The EMR approach has shown strong potential as a basis for a controller that is more understandable and physically interpretable than the RST-based solution. A major advantage of this methodology is its natural ability to distribute the control effort among the different state variables through simpler control loops. Such a structure facilitates both the understanding of the controller and the manual fine tuning of its different parts.

Conversely, the RST control approach is based on a complex polynomial formulation involving a large number of coefficients. As a result, improving the controller performance generally requires dedicated mathematical tools and accurate system models, since the controller parameters cannot be adjusted directly by hand in an intuitive way.

In this context, the concepts introduced through the EMR-based analysis of the POPS system appear particularly relevant. This is especially true for the treatment of current and voltage unbalance and for the active measurement of the output filter current. These developments will be implemented and tested during the final review phase of the POPS controller, scheduled for the end of 2026 and the beginning of 2027.

From a broader perspective, this PhD contributes to the ongoing evolution of control methodologies for accelerator power converters. It demonstrates that inversion-based control, supported by EMR, is a viable and promising alternative to classical approaches in a highly demanding industrial context. By providing a structured link between modelling and control, this methodology facilitates the design of controllers that are both physically meaningful and adaptable to complex system requirements.

In the context of future accelerator projects, such as next-generation synchrotrons or large-scale infrastructures, the need for flexible, robust, and high-performance control architecture will continue to grow. Systems will become more complex, with increased integration of energy storage, tighter performance constraints, and stronger interactions between subsystems. In this perspective, approaches based on energetic modelling and systematic control synthesis are expected to play an increasingly important role.

Several directions for future works can be identified. One important extension concerns the integration of fault-tolerant control strategies within the inversion-based framework. While this work has primarily focused on nominal operations, the ability to maintain performance under component failures or degraded conditions is a key requirement for future systems. Another area of interest is the optimization

of the control structure to reduce implementation complexity while preserving performance. This may involve the simplification of the maximal control structure or the use of advanced control techniques in combination with EMR. Finally, the application of the proposed methodology to other types of accelerator power converters or energy systems could further validate its generality and usefulness.

In conclusion, this PhD has shown that the inversion-based control derived from Energetic Macroscopic Representation provides a coherent, flexible, and effective framework for the control of complex pulsed power systems such as POPS. Through modelling, simulation, and experimental validation, the work demonstrates that this approach can meet the stringent requirements of accelerator applications while offering improved interpretability and adaptability. These results contribute to the development of next-generation control strategies for high-performance power electronics in particle accelerators and beyond.

Annexes

Annexe A- Future Circular Collider

Future Circular Collider-ee (FCC) would function as a high-precision instrument, enabling accurate measurements of the properties of fundamental particles. The large datasets expected would improve the precision of key measurements by up to two orders of magnitude compared to previous experiments, allowing robust tests of the Standard Model and strong sensitivity to indirect effects of new physics (Benedikt 2025).

The hadron collider stage, FCC-hh, is designed to significantly extend the energy frontier, with proton–proton collisions with an energy of approximately 100 TeV. This increase in energy would expand the discovery reach for new particles well beyond that of the LHC and allow detailed studies of rare processes, including Higgs boson self-interactions, which are essential for probing the structure of the Higgs potential. FCC-hh would also provide sensitivity to a wide range of theoretical scenarios, such as heavy resonances, new strong dynamics, and dark matter candidates.

The realization of the FCC requires substantial advances in accelerator technology. For FCC-hh, the most critical technological challenge is the development of superconducting dipole magnets capable of generating magnetic fields of approximately 16 T. Such magnets are necessary to steer 50 TeV proton beams within the proposed tunnel circumference. The FCC studies identify Nb_3Sn-based superconductors as the baseline technology, while recognizing the need for further research, industrial development, and cost reduction before large-scale deployment.

In the case of FCC-ee, the dominant technical issues are related to synchrotron radiation, beam stability, and power efficiency. The accelerator design incorporates high-efficiency radiofrequency systems, advanced vacuum technologies, and sophisticated beam optics to achieve the required luminosity while maintaining manageable power consumption (Benedikt 2025). These considerations are central to ensuring the operational sustainability of the facility.

Detector concepts developed for the FCC must also meet demanding performance requirements. The expected physics program necessitates excellent resolution, precise momentum measurements, and advanced timing capabilities. While many detector technologies build upon experience from the LHC, the FCC environment requires further innovation to manage higher luminosities and, in the hadron collider phase, extreme radiation levels.

Environmental impact and sustainability are integral components of the FCC design studies. Detailed assessments have been conducted on power consumption, land use, and integration into the local environment. The FCC reports emphasize energy efficiency and explore possibilities for reusing waste

heat generated by accelerator operations, for example through connection to regional heating networks (Zimmermann 2025).

Beyond its scientific objectives, the FCC is expected to have a broad societal impact. Large accelerator projects historically contribute to technological advances in fields such as superconductivity, cryogenics, materials science, and data processing. The FCC is also envisaged as a long-term platform for international collaboration, education, and training, supporting the development of highly skilled personnel over several decades (Zimmermann 2025).

Another future project discussed at CERN is the muon collider has emerged as a promising option for the next generation of high-energy particle colliders, offering a unique combination of high energy reach and clean lepton–lepton collisions. Muons are elementary particles, similar to electrons but with a mass approximately 200 times larger. This large mass dramatically suppresses synchrotron radiation, which scales inversely with the fourth power of the particle mass. As a consequence, muons can be accelerated in circular rings to multi-TeV energies without the energy losses that limit electron–positron colliders, enabling compact facilities with energies comparable to those of future hadron colliders (Schulte 2020), (Delahaye 2019).

From a physics perspective, a muon collider provides a clean experimental environment with well-defined initial states, allowing precise measurements and straightforward theoretical interpretation. At energies from a few hundred GeV up to several TeV, such a machine would enable detailed studies of Standard Model processes and offer strong sensitivity to physics beyond the Standard Model. In particular, muon colliders are well suited for the exploration of heavy new particles and contact interactions at energy scales beyond the direct reach of electron–positron colliders (Schulte 2020), (Delahaye 2019).

One of the main strengths of a muon collider is its ability to act as a Higgs factory. Unlike electron–positron colliders, a muon collider can produce Higgs bosons directly when 2 particles collide, because the Higgs couples much more strongly to muons than to electrons. This direct production makes it possible to measure key Higgs properties such as its mass, total decay width, and interaction strengths with very high precision. These measurements are extremely challenging, or even unattainable, at other types of colliders. Furthermore, if operated at higher energies, the same machine could be used to study Higgs self-interactions and rare Higgs-related processes, helping to clarify the mechanism of electroweak symmetry breaking. (Schulte 2020), (Delahaye 2019).

The principal challenges of the muon collider concept stem from the finite lifetime of the muon, which is approximately 2.2 microseconds at rest. This short lifetime necessitates rapid production, cooling, acceleration, and collision of muon beams before significant decay occurs. Considerable progress has

been made in demonstrating the feasibility, although further development and system-level integration are required for a full-scale collider (Schulte 2020), (Delahaye 2019), (Schulte 2022).

Muon decay also produces a substantial flux of secondary particles, primarily electrons and neutrinos, which generate backgrounds in detectors and impose demanding requirements on shielding and machine–detector interface design. Detailed simulation studies indicate that these backgrounds can be mitigated allowing the physics goals of the collider to be achieved without compromising detector performance (Delahaye 2019), (Schulte 2022).

In the broader context of future collider strategies, the muon collider is generally regarded as a longer-term option that complements projects such as the Future Circular Collider. While its technological readiness is currently lower than that of electron–positron or hadron collider proposals, recent studies show steady progress toward resolving its key challenges. Continued research and development in muon sources, cooling technologies, and accelerator components will determine whether the muon collider can mature into a viable and competitive facility for exploring the high-energy frontier.

Annexe B-FGC4

The FGC4 uses a modular cassette architecture built around a Linux-capable System-on-Module (SoM) featuring an AMD/Xilinx Zynq UltraScale+ MPSoC. This platform combines multiple ARM Cortex-A53 cores and FPGA programmable logic (PL) to deliver deterministic real-time control with a system management and diagnostics, enabling regulation rates up to an order of magnitude higher than previous generations (Zielinski 2025), (Cejp 2023).

From a system perspective, FGC4's design emphasizes extensibility and reusability beyond CERN's internal ecosystem by supporting compatibility with widely adopted control frameworks like EPICS and TANGO (Zielinski 2025). The modular hardware comprising SoM, digital and analogue boards, and passive backplane connectivity allow flexible scaling from single-converter setups to multi-slot control systems, with dedicated networking and debugging interfaces for both technical networks and private real-time segments (Zielinski 2025). On the software side, FGC4 partitions tasks between a Linux front-end responsible for configuration, supervision, and integration with accelerator control systems, and bare-metal applications executing high-bandwidth regulation loops, often using established control libraries (CCLIBS) to encapsulate core converter control functions (Cejp 2023). This hybrid architecture ensures that real-time constraints are met without sacrificing configurability, maintainability, or compatibility with future developments in control software and hardware integration (Cejp 2023).

Annexe C-Parameters of POPS

Component	Value
Magnet inductance	0.954 H
Magnet resistance	0.2 Ω
Capacitive Filter C branch capacitance	160 μF
Capacitive Filter R-C branch capacitance	1.49 mF
Capacitive Filter R-C branch resistance	3.1 Ω
Inductive Filter common mode inductance	5 mH
Inductive Filter common mode resistance	1 mΩ
Inductive Filter differential mode inductance	2.8 mH
Inductive Filter differential mode resistance	1 mΩ
Inductive Filter mutual inductance	-1.6 mH
Capacitive bridge capacitance	17.4 mF
Capacitive storage capacitance	247 mF

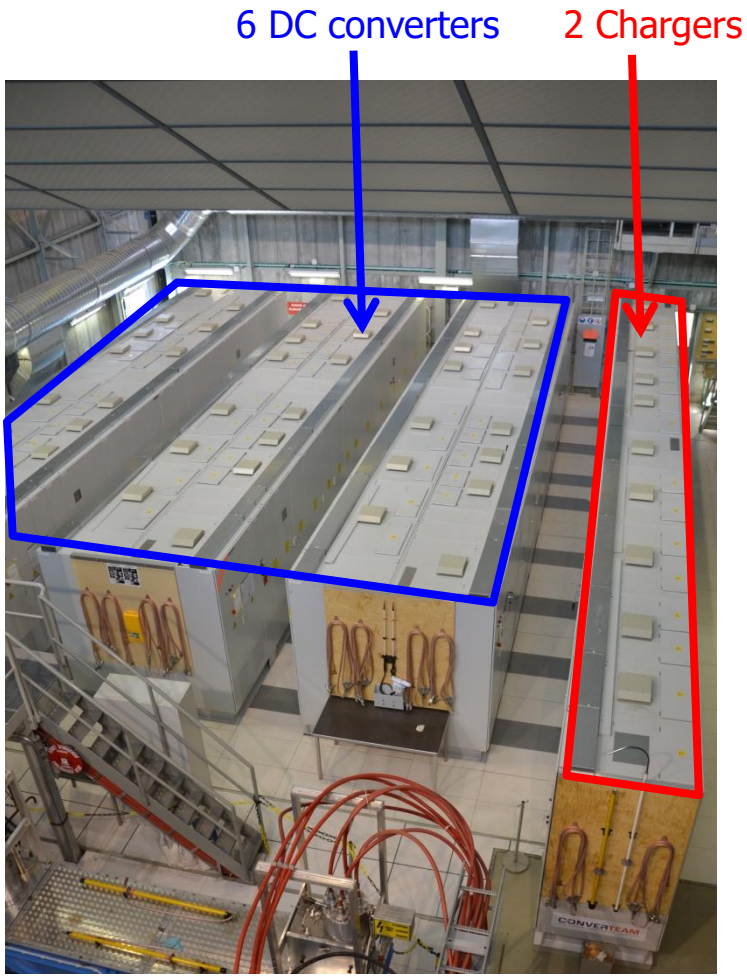
Annexe D-Additional pictures of POPS component

Outside and inside view of a shipping container housing the storage capacitors:





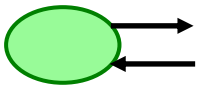
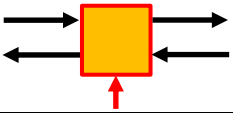
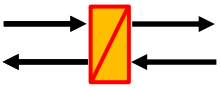
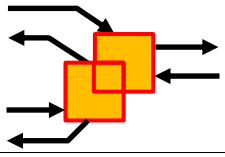
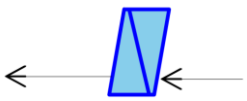
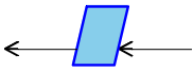
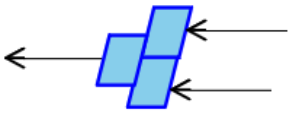
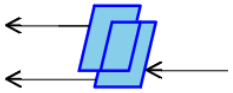
Picture of the converters of POPS inside the electrical room.



Annexe E-EMR pictograms

The Energetic Macroscopic Representation (EMR) was developed by the Laboratoire d'Électrotechnique et d'Électronique de Puissance of Lille (L2EP) in the 2000s. This formalism is used to represent complex system, while following a functional description (Bouscayrol 2012).

Table 3: pictogram of the EMR

Element	Symbols
Energy source	
Mono-physical converter	
Energy accumulation	
Mono-physical coupling	
Indirect inversion	
Direct Inversion	
Switching control element	
Coupling distribution element	
Mandatory sensor	
Avoidable sensor	

k_f is rewritten using the numbers of converters:

$$k_f = \frac{(N_{FA}+N_{FB})E_f}{[(N_{FA}+N_{FB})E_f+(N_{CA}+N_{CB})E_c]} \quad (171)$$

The total available energy in function of the number of converters is:

$$E_t = (N_{FA} + N_{FB})E_f + (N_{CA} + N_{CB})E_c \quad (172)$$

To use all the available energy, the following condition must be satisfied:

$$k_f v_l = (N_{FA} + N_{FB})v_f \quad (173)$$

$$(1 - k_f)v_l + v_r = (N_{CA} + N_{CB})v_c \quad (174)$$

Since $v_l = u_m - v_R$ the following relation are obtained:

$$v_{f_ref} = k_f \frac{(u_{m_ref}-v_r)}{(N_{FA}+N_{FB})} \quad (175)$$

$$v_{c_ref} = \frac{[(1-k_f)(u_{m_ref}-v_r)]}{(N_{CA}+N_{CB})} = \frac{[(1-k_f)u_{m_ref}+k_f v_r]}{(N_{CA}+N_{CB})} \quad (176)$$

Given that the voltage of the even side is the number of converters time their voltage reference:

$$u_{fA_ref} = N_{FA}v_{f_ref} + N_{CA}v_{f_ref} \quad (177)$$

And for the even side:

$$u_{fB_ref} = N_{FB}v_{f_ref} + N_{CB}v_{f_ref} \quad (178)$$

So:

$$u_{fA_ref} = N_{FA}v_{f_ref} + N_{CA}v_{c_ref} = N_{FA}k_f \frac{(u_{m_ref}-v_r)}{(N_{FA}+N_{FB})} + N_{CA} \frac{[(1-k_f)u_{m_ref}+k_f v_r]}{(N_{CA}+N_{CB})} \quad (179)$$

$$u_{fB_ref} = N_{FB}v_{f_ref} + N_{CB}v_{c_ref} = -N_{FB}k_f \frac{(u_{m_ref}-v_r)}{(N_{FA}+N_{FB})} - N_{CB} \frac{[(1-k_f)u_{m_ref}+k_f v_r]}{(N_{CA}+N_{CB})} \quad (180)$$

It can be demonstrated that the voltage reference for the odd side is:

$$u_{fA_ref} = k_{AUF}u_{m_ref} + k_{AVR}v_r \quad (181)$$

With $k_{AUF} = \frac{[N_{FA}N_{CB}k_f + N_{CA}(N_{FA}+N_{FB}) - N_{CA}N_{FB}k_f]}{(N_{CA}+N_{CB})(N_{FA}+N_{FB})}$

And $k_{AVR} = \frac{[-N_{FA}(N_{CB}+N_{CA}N_{FB})]k_f}{(N_{CA}+N_{CB})(N_{FA}+N_{FB})}$

And for the even side:

$$u_{fB_ref} = k_{BUF}u_{m_ref} + k_{BVR}v_r \quad (182)$$

With $k_{BUF} = \frac{[-N_{FB}(N_{CA}+N_{CB})k_f - N_{CB}(N_{FA}+N_{FB})(1-k_f)]}{(N_{CA}+N_{CB})(N_{FA}+N_{FB})}$

And $k_{BVR} = \frac{[N_{FB}(N_{CA}+N_{CB})k_f - N_{CB}(N_{FA}+N_{FB})k_f]}{(N_{CA}+N_{CB})(N_{FA}+N_{FB})}$

Given the previous strategy and the desire to make the floatings $N_{FA} + N_{FB}$ and the chargers $N_{CA} + N_{CB}$ operate identically, the following relation is obtained:

$$u_{AFi_ref} = v_{f_ref} = k_f \frac{(u_{m_ref} - v_r)}{(N_{FA}+N_{FB})} = FLu_{f_ref} - FLv_r \quad (183)$$

With $FL = \frac{k_f}{(N_{FA}+N_{FB})}$

$$u_{BFj_ref} = v_{f_ref} = -k_f \frac{(u_{m_ref} - v_r)}{(N_{FA}+N_{FB})} = -FLu_{f_{ref}} + FLv_r \quad (184)$$

$$u_{ACk_ref} = v_{C_ref} = \frac{[(1-k_f)u_{m_ref} + k_f v_r)]}{(N_{CA}+N_{CB})} = CHUu_{f_ref} + FLVv_r \quad (185)$$

With $CHU = \frac{(1-k_f)}{(N_{CA}+N_{CB})}$

And $FLV = \frac{k_f}{(N_{CA}+N_{CB})}$

$$u_{BClk_ref} = -v_{C_ref} = -\frac{[(1-k_f)u_{m_ref} + k_f v_r)]}{(N_{CA}+N_{CB})} = -CHUu_{f_ref} - FLVv_r \quad (186)$$

with $i \in [0, N_{FA}]$
with $j \in [0, N_{FB}]$
with $k \in [0, N_{CA}]$
with $l \in [0, N_{CB}]$

After performing the required computations, the following results are obtained:

The voltage for the odd side:

$$u_{fA_ref} = k_{AUF}u_{m_ref} + k_{AVR}v_r \quad (187)$$

And the voltage for N floating converter:

$$u_{AFi_ref} = FLu_{m_ref} - FLv_r \quad (188)$$

That can be rewritten with u_{fA_ref}:

$$u_{AFi_ref} = \frac{[u_{fA_ref} - (k_{AUF} + k_{AVR})v_r]FL}{k_{AUF}} \quad (189)$$

The voltage for the even side:

$$u_{fB_ref} = k_{BUF}u_{m_ref} + k_{BVR}v_r \quad (190)$$

And the voltage for N floating converter:

$$u_{BFj_ref} = -FLu_{m_ref} + FLv_r \quad (191)$$

That can be rewritten with u_{fB_ref}:

$$u_{BFj_ref} = \frac{[-u_{fB_ref} + (k_{BUF} + k_{BVR})v_r]FL}{k_{BUF}} \quad (192)$$

The voltage for the charger converter on the odd side:

$$u_{ACk_ref} = CHUu_{m_ref} + FLVv_r \quad (193)$$

That can be rewritten with u_{fA_ref}:

$$u_{ACk_ref} = \frac{[CHUu_{fA_ref} + (k_{AUF}.FLV - k_{AVR}.CHU)v_r]}{k_{AUF}} \quad (194)$$

The voltage for the charger converter on the even side:

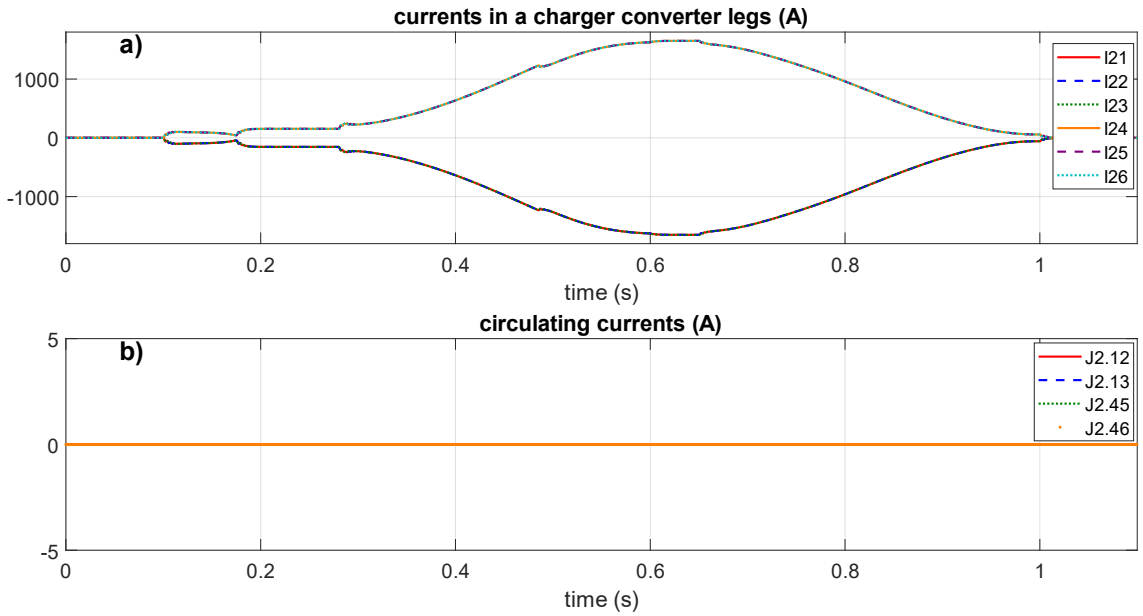
$$u_{BCl_ref} = -CHUu_{m_ref} - FLVv_r \quad (195)$$

That can be rewritten with u_{fB_ref}:

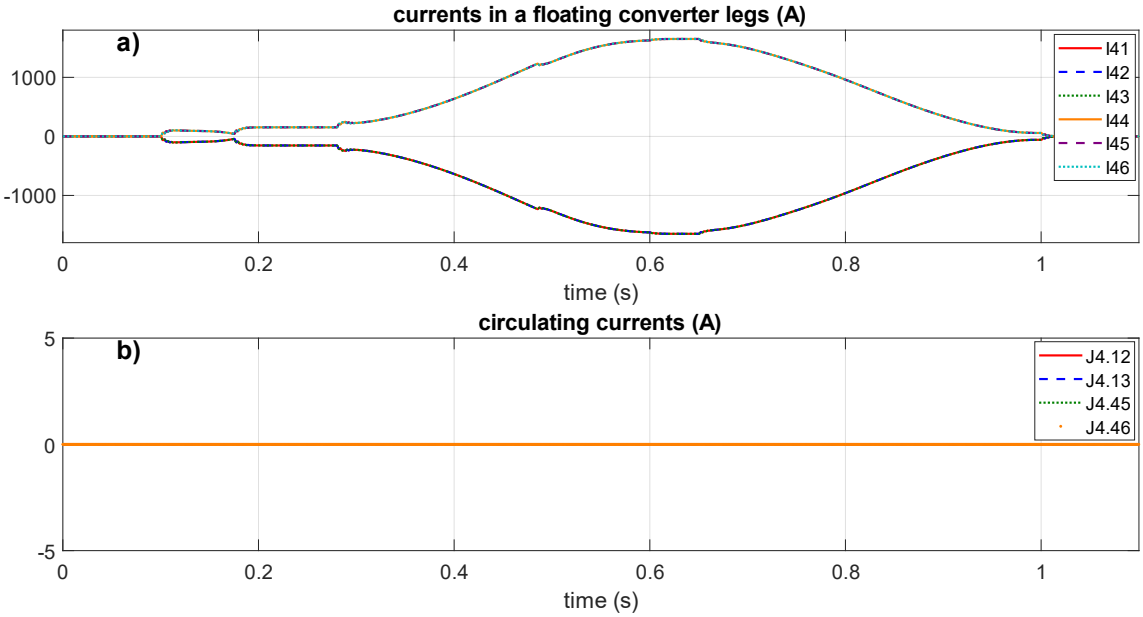
$$u_{BCl_ref} = \frac{(-CHU)u_{fB_ref} + (-k_{BUF}.FLV + k_{BVR}.CHU)v_r]FL}{k_{BUF}} \quad (196)$$

Annexe G-Average results of POPS.

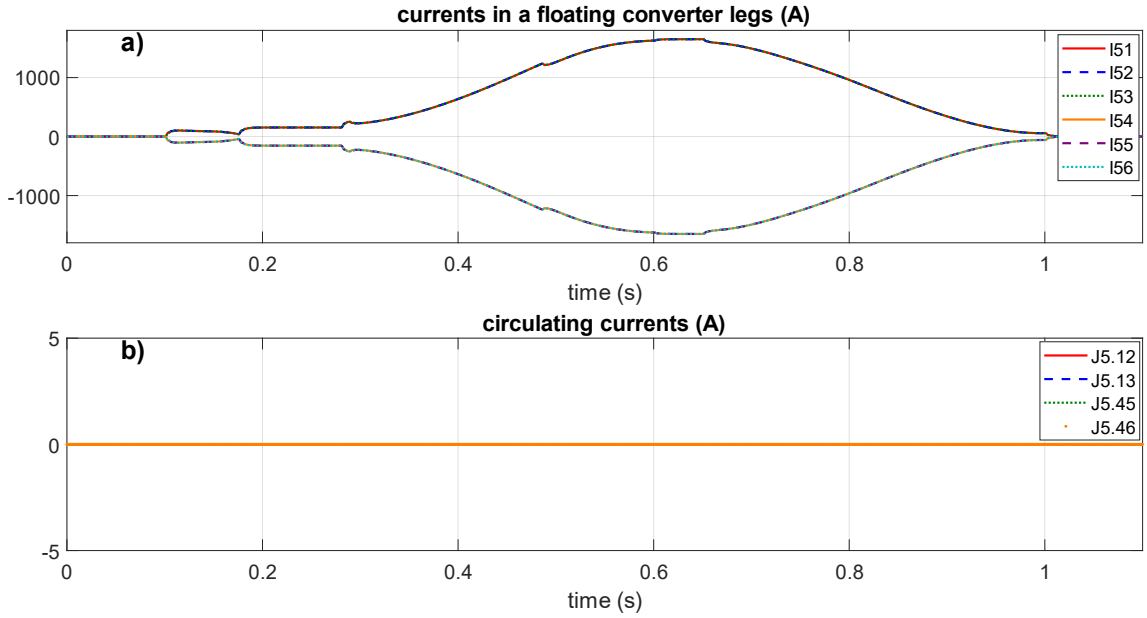
Average currents in charger or floating converter legs and circulating currents:



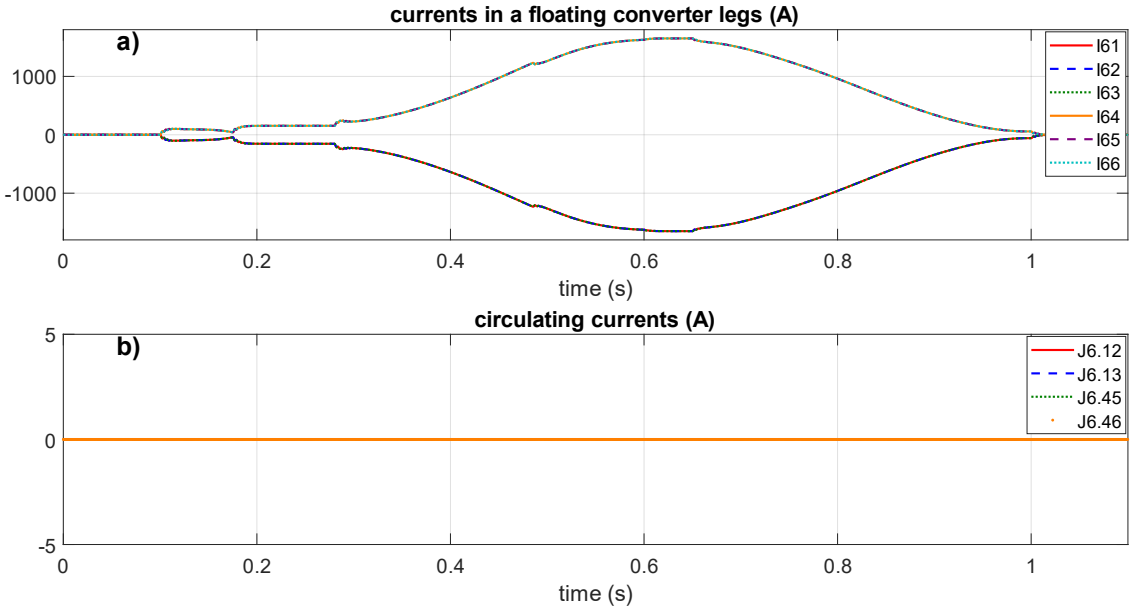
Average currents and circulating currents in the floating 4 legs



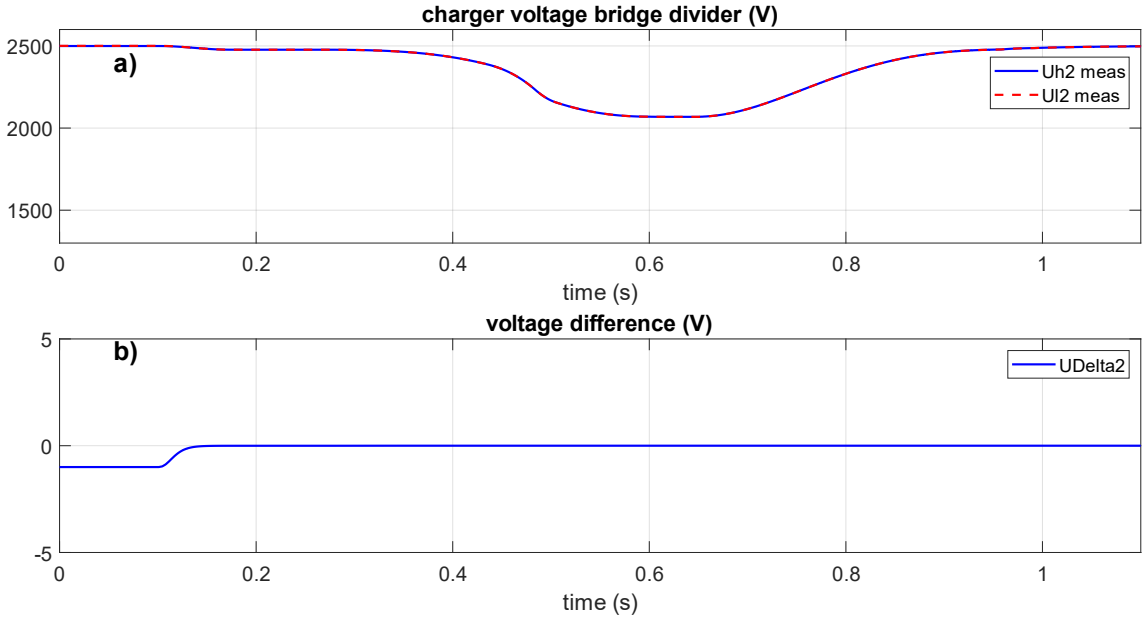
Average currents and circulating currents in the floating 5 legs



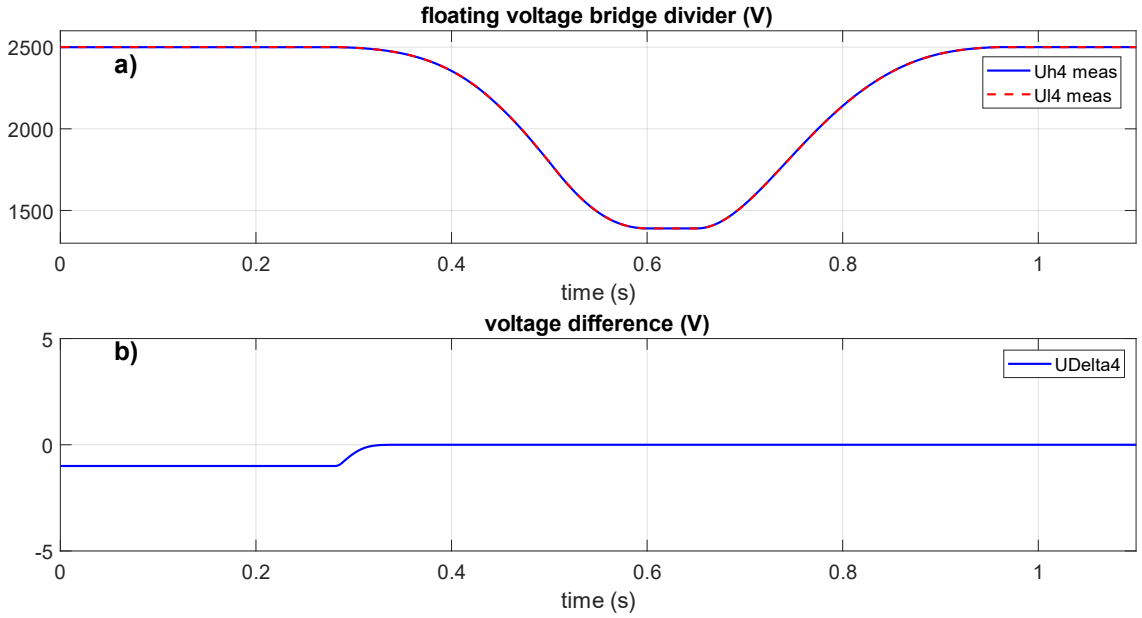
currents and circulating currents in the floating 6 legs



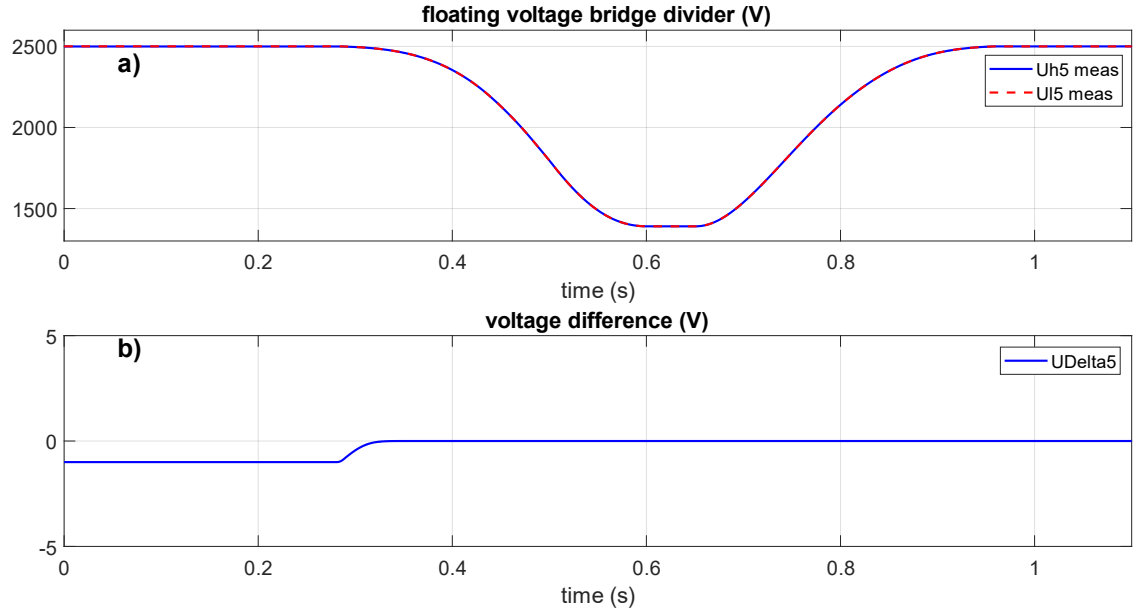
Average voltage bridge divider and voltage difference of u_{h2} and u_{l2}:



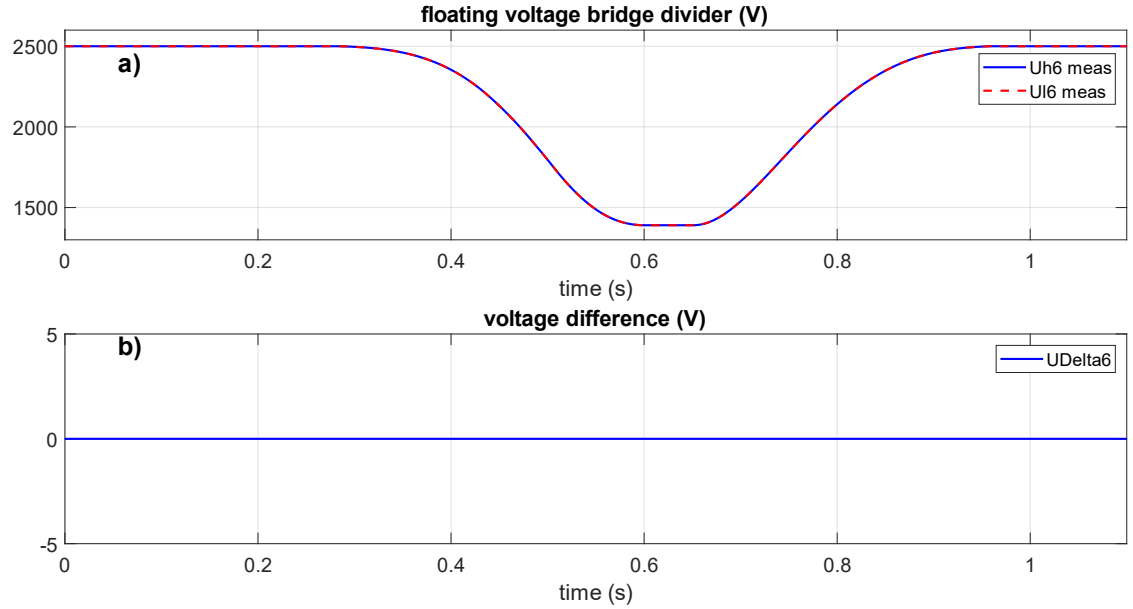
Average voltage bridge divider and voltage difference of u_{h4} and u_{l4}:



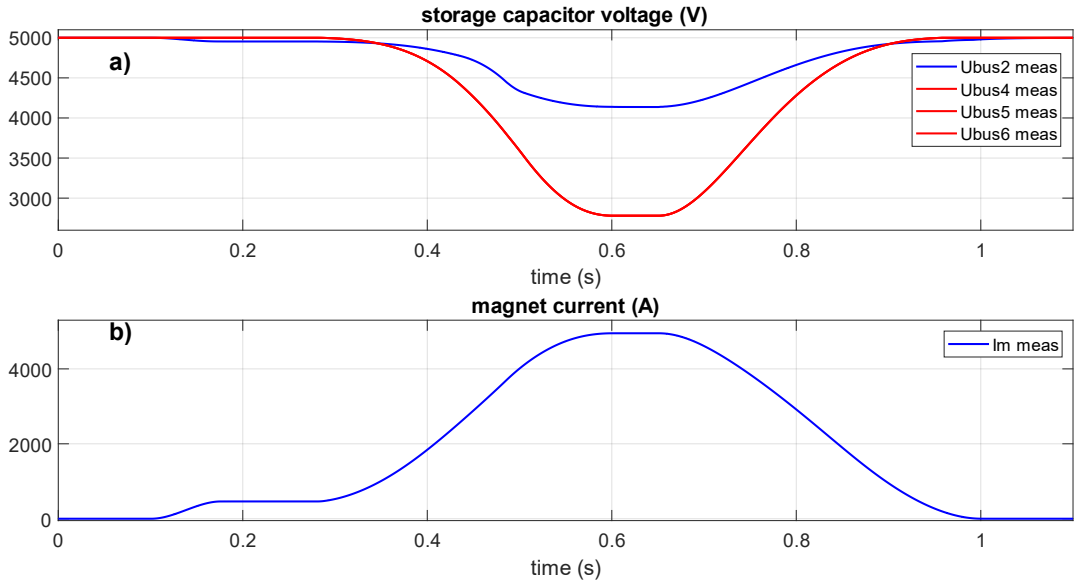
Average voltage bridge divider and voltage difference of u_{h5} and u_{l5}:



Average voltage bridge divider and voltage difference of u_{h6} and u_{l6}:

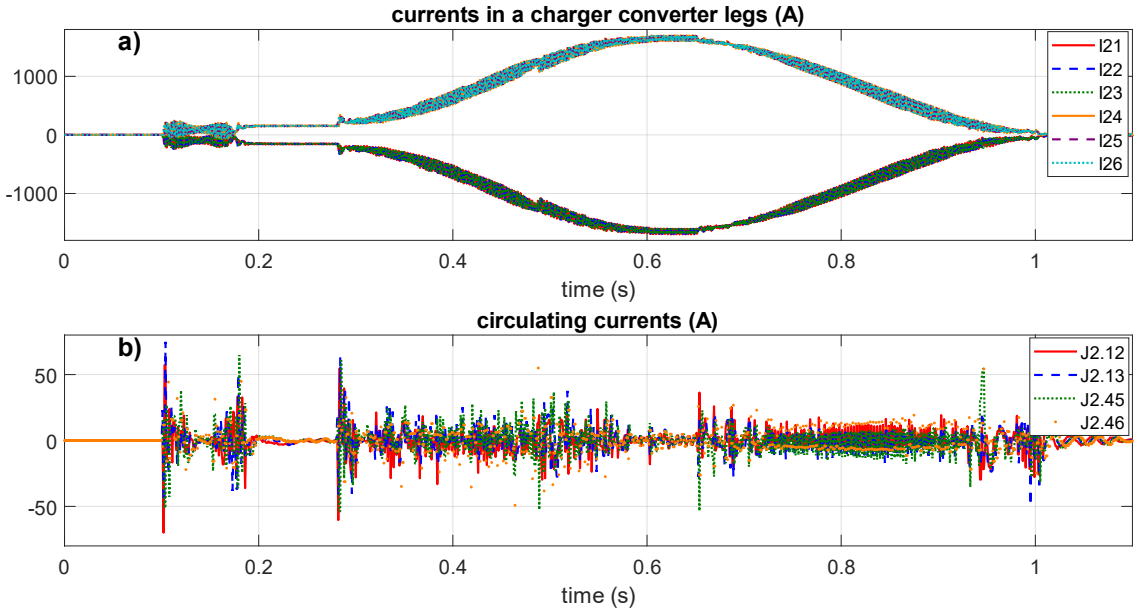


Average voltages of the storage capacitor C2, C4, C5 and C6 and the current i_m

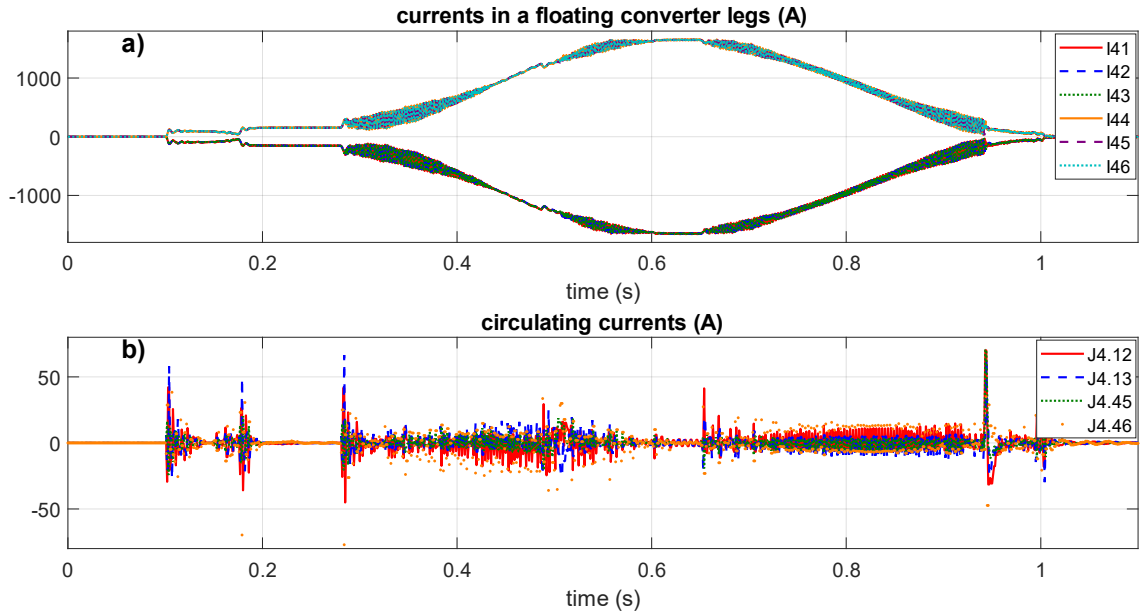


Annexe H-Discrete results of POPS.

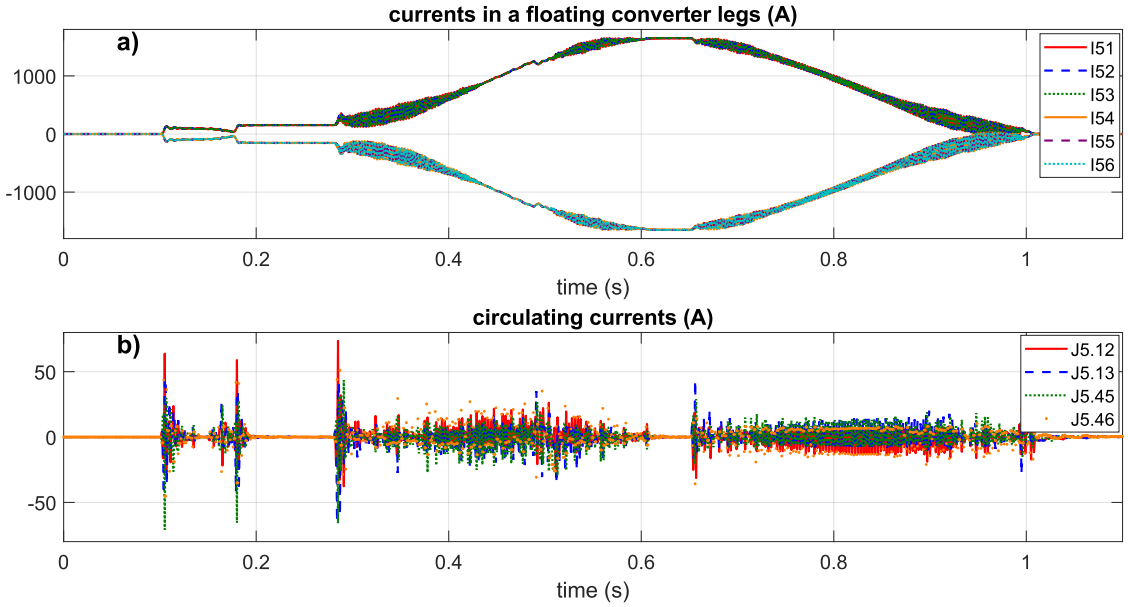
Discrete currents and circulating currents in the charger 2 legs:



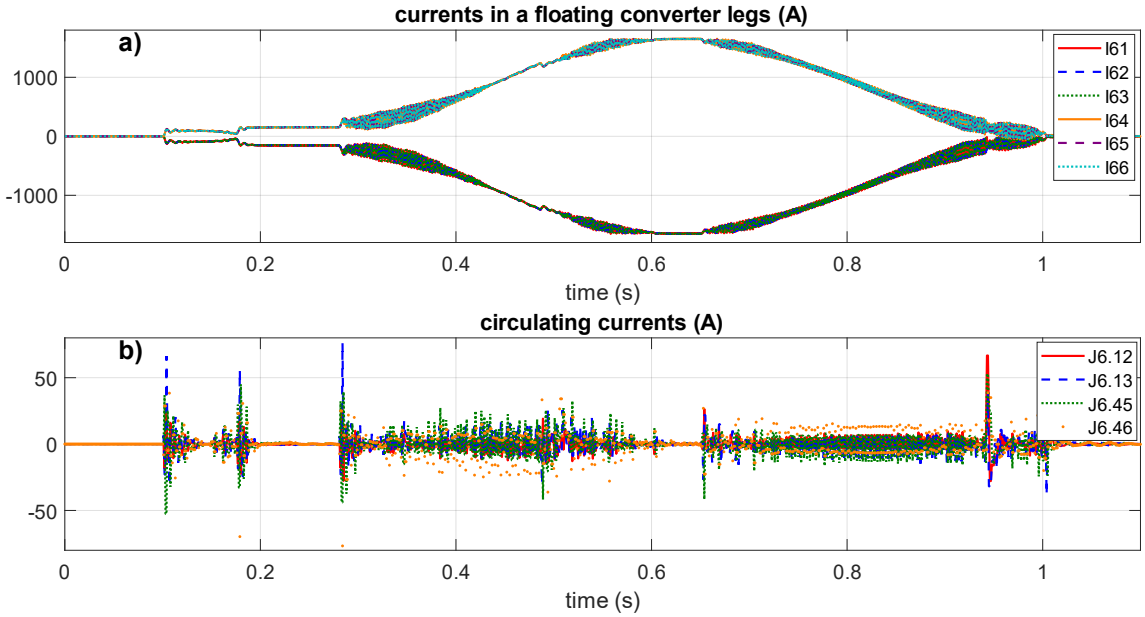
Discrete currents and circulating currents in the floating 4 legs:



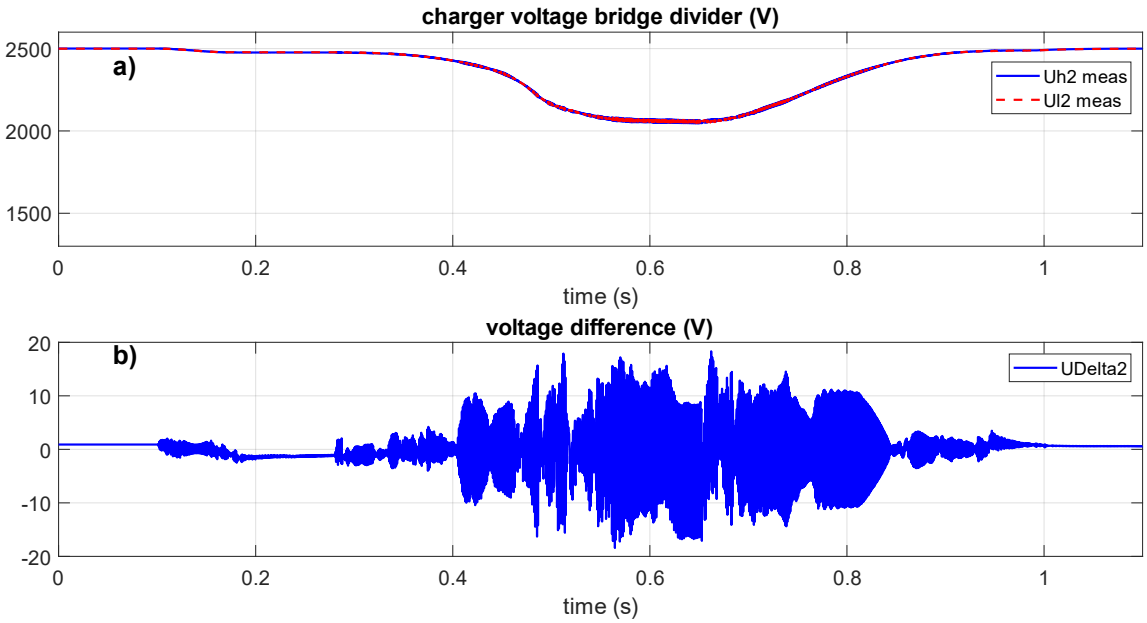
Discrete currents and circulating currents in the floating 5 legs:



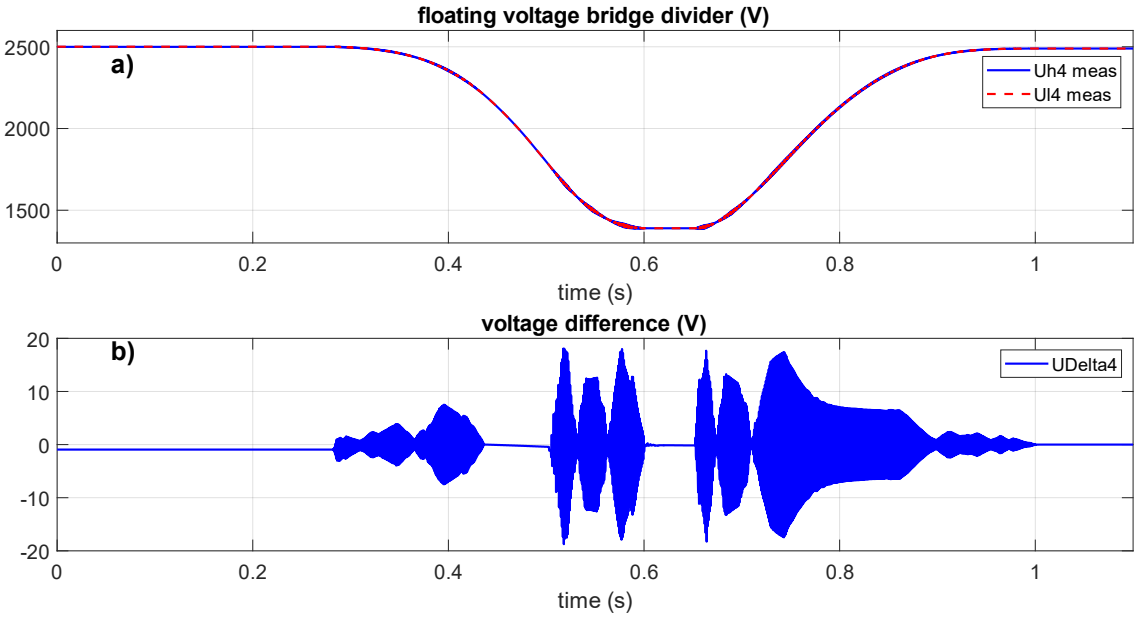
Discrete currents and circulating currents in the floating 6 legs:



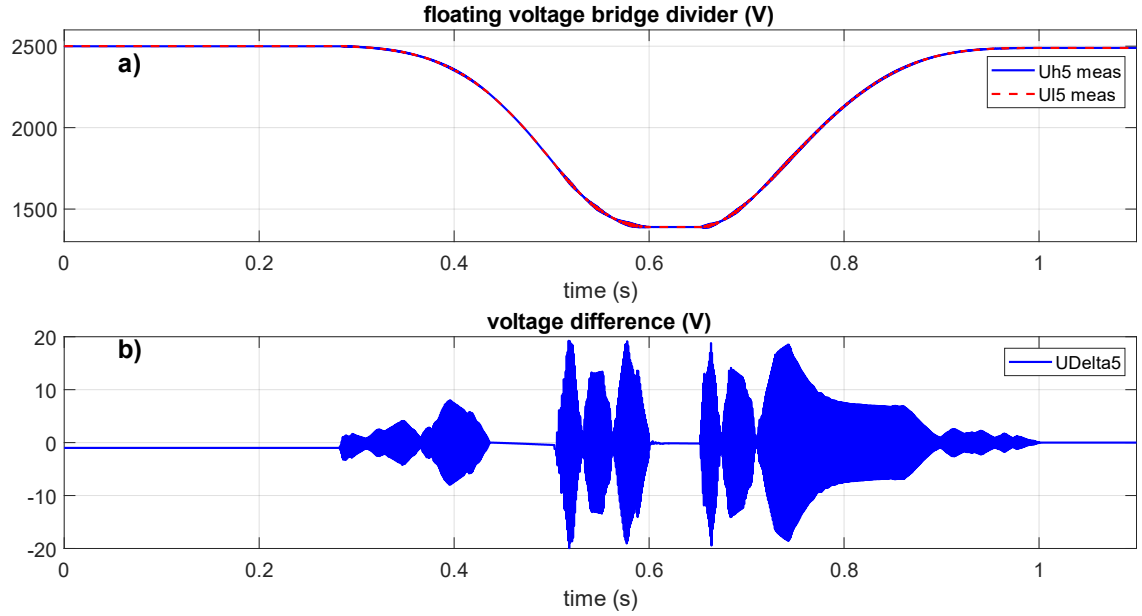
Discrete voltage bridge divider and voltage difference of u_{h2} and u_{l2}:



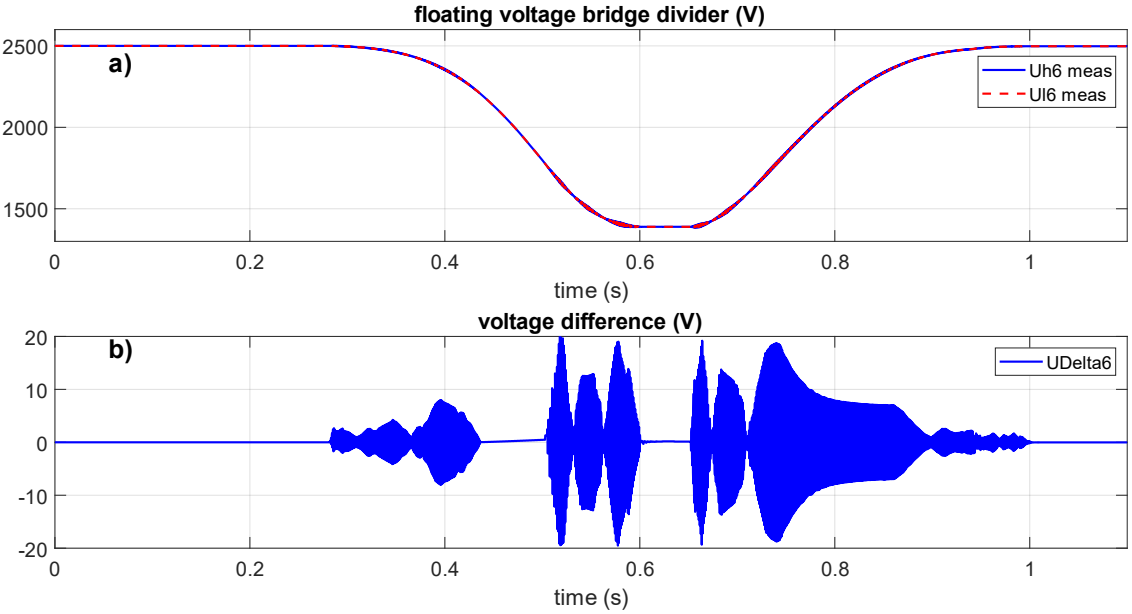
Discrete voltage bridge divider and voltage difference of u_{h4} and u_{l4}:



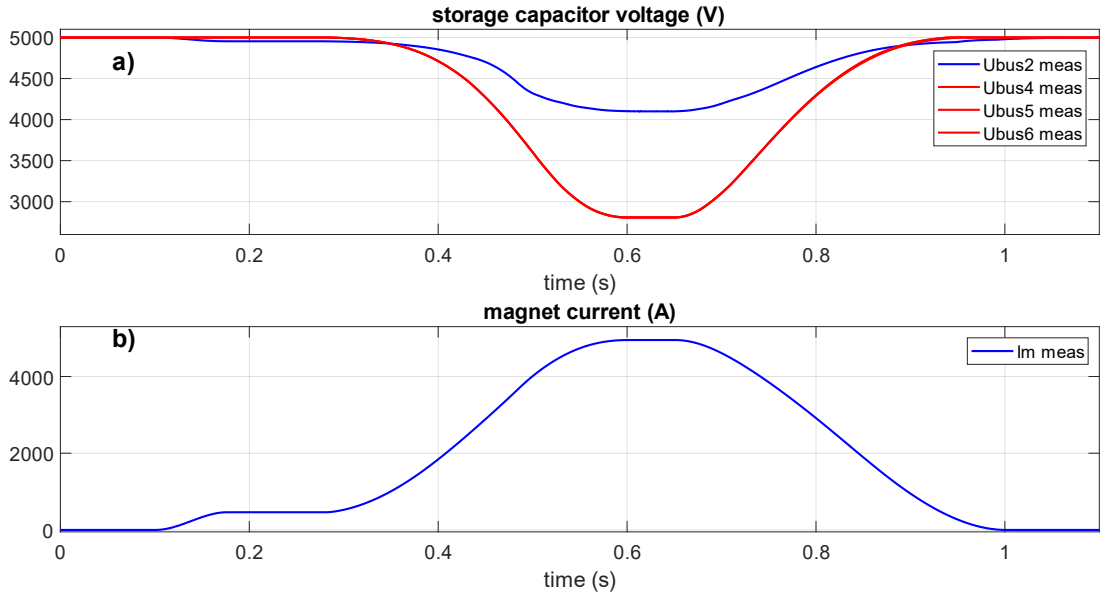
Discrete voltage bridge divider and voltage difference of u_{h5} and u_{l5}:



Discrete voltage bridge divider and voltage difference of u_{h6} and u_{l6}:



Discrete voltages of the storage capacitor C2, C4, C5 and C6 and the current i_m



References

(Allègre 2010) A. L. Allègre, A. Bouscayrol, P. Delarue, P. Barrade, E. Chattot, S. El Fassi, “Energy Storage System with supercapacitor for an innovative subway", IEEE transactions on Industrial Electronics, vol. 57, no. 12, pp. 4001-4012, December 2010

(Aroua 2023) A. Aroua, W. Lhomme, F. Verbelen, M. N. Ibrahim, A. Bouscayrol, P. Sergeant, K. Stockman, “Impact of scaling laws of permanent magnet synchronous machines on the accuracy of energy consumption computation of electric vehicles”, eTransportation, Vol. 18, October 2023, ref.100269

(Baziz 2025) A. Baziz, D. Xystras, G. Le Godec, P. Delarue, and A. Bouscayrol, “Inversion-based control simplifications for a cycling-mode power converter in particle accelerators,” in *Proc. The 26th European Conference on Power Electronics and Applications (EPE’25)*, Paris, France, Mar. 2025, paper hal-05082310v1, 2025. Available: https://utc.hal.science/hal-05082310v1/document.

(Benedikt 2025) M. Benedikt et al., “Future Circular Collider Feasibility Study Report: Volume 1 Physics, Experiments, Detectors,” CERN-FCC-PHYS-2025-0002, CERN, Geneva, 2025, doi: 10.17181/CERN.9DKX.TDH9.

(Boattini 2015) F. Boattini, J.-P. Burnet, and G. Skawinski, “POPS: the 60 MW power converter for the PS accelerator: Control strategy and performances,” presented at the 17th European Conference on Power Electronics and Applications (EPE’15), Geneva, Switzerland, Sep. 8–10, 2015, *CERN-ACC-2015-0098*, 10 pp., doi:10.1109/EPE.2015.7309267.

(Bordry 2020) F. Bordry, L. Bottura, A. Milanese, et al., “Accelerator Technology,” in *Particle Physics Reference Library*, Springer, Cham, 2020, pp. 97–120, doi:10.1007/978-3-030-34245-6_8.

(Boulon 2012) L. Boulon, K. Agbossou, D. Hissel, P. Sicard, A. Bouscayrol, M. C. Péra, “A macroscopic PEM fuel cell model including water phenomena for vehicle simulation", Renewable Energy, vol. 46, pp. 81-91, October 2012

(Bouscayrol 2000) A. Bouscayrol, B. Davat, B. de Fornel, B. François, J. P. Hautier, F. Meibody-Tabar, M. Pietrzak-David, "Multimachine Multiconverter System: application for electromechanical drives", European Physics Journal - Applied Physics, vol. 10, no. 2, pp. 131-147, May 2000

(Bouscayrol 2009) A. Bouscayrol, X. Guillaud, P. Delarue, B. Lemaire-Semail, “Energetic Macroscopic Representation and inversion-based control illustrated on a wind energy conversion system

using Hardware-in-the-loop simulation", IEEE transactions on Industrial Electronics, vol. 56, no. 12, pp. 4826-4835, December 2009

(Bouscayrol 2012) A. Bouscayrol, J. P. Hautier, B. Lemaire Semail, "Systemic design methodologies for electrical energy systems Analysis, Synthesis and Management", Chapter 3: Graphic formalisms for the control of multi-physical energetic system: COG and EMR, ISTE and Wiley, ISBN 978-1-84821-3888-3, 2012

(Brüning 2004) O. S. Brüning, P. Collier, P. Lebrun, S. Myers, R. Ostojic, J. Poole, and P. Proudlock, *LHC Design Report, Vol. 1: The LHC Main Ring*, Geneva, Switzerland: CERN, 2004, CERN Yellow Reports: Monographs. doi: 10.5170/CERN-2004-003-V-1.

(Burnet 2015) J.-P. Burnet, "Requirements for Power Converters," in *CAS-CERN Accelerator School: Power Converters*, R. Bailey, Ed., CERN Yellow Rep. CERN-2015-003, 2015, pp. 1–14. doi:10.5170/CERN-2015-003.1.

(Castaings 2016) A. Castaings, W. Lhomme, R. Trigui, A. Bouscayrol, "Comparison of energy management strategies of a battery/supercapacitors system for Electric Vehicle under limitations", Applied Energy, Vol. 163, February 2016, pp.190–200, DOI: 10.1016/j.apenergy.2015.11.020

(Cejp 2023) M. Cejp, D. Zielinski, and R. Murillo-Garcia, "Software architecture of FGC4, CERN's next-generation power converter control platform," in *Proc. 14th Int. Particle Accelerator Conf. (IPAC '23)*, Venice, Italy, May 2023, pp. WEPM080, doi: 10.18429/JACoW-IPAC2023-WEPM080.

(Cern Courrier) Cern courier website: https://cerncourier.com/a/tunnelling-to-the-future/, Accessed in 2025

(Coulinge 2022) É. Coulinge, High-Current Low-Voltage Power Supply for Superconducting Magnets, Ph.D. thesis, École Polytechnique Lausanne, Lausanne, Switzerland, 2020. doi: 10.5075/epfl-thesis-7835.

(Delahaye 2019) J. P. Delahaye, M. Diemoz, K. Long, B. Mansoulié, N. Pastrone, L. Rivkin, D. Schulte, A. Skrinsky, and A. Wulzer, "Muon Colliders," arXiv:1901.06150 [physics.acc-ph], Jan. 2019.

(Depature 2018) C. Depature, W. Lhomme, P. Sicard, A. Bouscayrol, L. Boulon, "Real-time Backstepping control for fuel cell vehicle using supercapacitors", IEEE transactions on Vehicular Technology, Vol. 67, no. 1, January 2018, pp. 306-314, DOI: 10.1109/TVT.2017.2728823

(Desreveaux 2019) A. Desreveaux, A. Bouscayrol, R. Trigui, E. Castex, J. Klein, "Impact of the Velocity Profile on Energy Consumption of Electric Vehicles", IEEE transactions on Vehicular

Technology, Vol. 68, no.8, December 2019, pp. 11420-11426, Print ISSN: 0018-9545, Online ISSN: 1939-9359, DOI: 10.1109/TVT.2019.2949215.

(EMR website) EMR website: http://www.emrwebsite.org/, Accessed in 2025

(Evans 2018) L. Evans, Eds., The Large Hadron Collider: a marvel of technology, 2nd ed. Lausanne, Switzerland: EPFL Press, 2018.

(Fadili 2025) S. Fadili, R. German, A. Bouscayrol, C. Mayet; P. Fianni, E. Noirtat, "Comparison of High-Energy Density and High-Power Density Batteries for an Electric Vehicle" Open Journal of Vehicular Technology, early access 2025, Vol. 6, pp. 1910-1919, DOI: 10.1109/OJVT.2025.3583070

(Fahrni 2007a) C. Fahrni, A. Rufer, F. Bordry, and J.-P. Burnet, "A multilevel power converter with integrated storage for particle accelerators," in *Proc. Power Conversion Conference (PCC'07)*, Nagoya, Japan, 2007, pp. 1480–1483.

(Fahrni 2007b) C. Fahrni, A. Rufer, F. Bordry, and J.-P. Burnet, "A novel 60 MW pulsed power system based on capacitive energy storage for particle accelerators," in *Proc. 2007 European Conference on Power Electronics and Applications (EPE'07)*, Aalborg, Denmark, Sept. 2007.

(Fahrni 2008) C. Fahrni, "Principe d'alimentation par convertisseurs multiniveaux à stockage intégré – application aux accélérateurs de particules," Ph.D. dissertation, École Polytechnique Fédérale de Lausanne, Lausanne, Switzerland, May 30, 2008, CERN-THESIS-2008-154. Available: https://repository.cern/records/47h67-m0e22.

(Gardner 1987) P.R. Gardner, A review of ion implantation applications to engineering materials, Materials & Design, Volume 8, Issue 4, 1987, ISSN 0261-3069, https://doi.org/10.1016/0261-3069(87)90136-1.(https://www.sciencedirect.com/science/article/pii/0261306987901361)

(Garnett 2015) R. W. Garnett, Phys. Procedia 66, 196 (2015). https://doi.org/10.1016/j.phpro.2015.05.026

(German 2024) R. German, T. Kalogianis, A. Bouscayrol, J. He, F. Tournez, M. Berecibar, C. Husar, M. Ciocan, S. Costa, A. Genic, B. Lemaire-Semail, "A flexible cloud-based HIL testing of batteries for various electrified vehicles," IEEE Transactions on Vehicular Technology, vol. 73, no. 4, pp. 4610-4620, April 2024, DOI: 10.1109/TVT.2023.3337655

(Godart 2022) G. Godart, "Comparison of inversion-based control and state feedback control for the SIRIUS FP2P2S power converters", Master's thesis, Univ. Lille, L2EP, Lille, France, 2022.

(Gschwendtner 2016) E. Gschwendtner, M. Wing, A. Aschikhin, C. Bautista Gonzalez, E. Baynham, S. Bettoni, et al., “AWAKE, The Advanced Proton Driven Plasma Wakefield Acceleration Experiment at CERN,” *Nucl. Instrum. Methods Phys. Res., Sect. A*, vol. 829, pp. 76–82, 2016, doi: 10.1016/j.nima.2016.02.026.

(Horrein 2017) L. Horrein, J.-M. Cravero, and A. Bouscayrol, “Hybrid capacitor discharge/switch-mode converter for pulsed applications: Topology and control design,” in *Proc. 19th European Conf. on Power Electronics and Applications (EPE’17 ECCE Europe)*, Warsaw, Poland, 2017.

(Horrein 2020) L. Horrein, J. -M. Cravero, P. Delarue, A. Bouscayrol, D. Aguglia and C. Ortega- Perez, "Dead-Time influence on fast switching pulsed power converters design - A high current application for accelerator's magnets," 2020 22nd European Conference on Power Electronics and Applications (EPE'20 ECCE Europe), 2020, pp. P.1-P.10, doi: 10.23919/EPE20ECCEEurope43536.2020.9215727.

(Josifović 2017) I. Josifović, M. C. Bastos, G. Le Godec, J. P. Burnet, I. Romera, M. Zerlauth, and M. Werner, “A 600 kW power supply for particle accelerators insensitive to electrical network perturbations,” in Proc. 19th European Conference on Power Electronics and Applications (EPE’17 ECCE Europe), Warsaw, Poland, Sep. 2017, pp. 8099278, doi: 10.23919/EPE17ECCEEurope.2017.8099278.

(King 2015) Q. King, “Controls and interfaces,” in *CAS-CERN Accelerator School: Power Converters*, R. Bailey, Ed., CERN Yellow Reports: School Proceedings, CERN-2015-003, Geneva, Switzerland, 2016, pp. 379–394, doi:10.5170/CERN-2015-003.379.

(Lauria 2022) A. Lauria, P. Arpaia, M. Buzio, A. Gilardi, M. Parvis, M. Pentella, L. Sabbatini, E. Simoni, and A. Vannozzi, “Rotating-coil measurement system for small-bore-diameter magnet characterization,” *Sensors*, vol. 22, no. 21, Art. no. 8359, Oct. 31, 2022, doi: 10.3390/s22218359.

(Lee 2011) S. Y. Lee, Accelerator Physics, 3rd ed. Singapore: World Scientific, 2011. doi: 10.1142/8335.

(Letrouvé 2013) T. Letrouvé, W. Lhomme, A. Bouscayrol, N. Dollinger, “Control validation of Peugeot 3∞8 Hybrid4 vehicle using a reduced-scale power HIL simulation", Journal of Electrical Engineering and Technology, Vol. 8, no. 5, September 2013, pp. 1227-1233

(Lévine 2009) Jean Lévine. Analysis and Control of Nonlinear Systems A Flatness-based Approach. Springer Berlin Heidelberg, pp.320, 2009, ⟨10.1007/978-3-642-00839-9⟩. ⟨hal-00482917⟩

(Lhomme 2017) W. Lhomme, A. Bouscayrol, S.A. Syed, S. Roy, F. Gailly, O. Pape, “Energy Savings of a Hybrid Truck using a Ravigneaux Gear Train", IEEE transactions on Vehicular Technology, vol. 66, no.10, October 2017, pp. 8682 – 8692, DOI: 10.1109/TVT.2017.2710378

(Li 2020) W. Li, J. Han, L. Zhou, C. Deng and M. Yan, "A Novel SVPWM Method for NPC three-level interleaved H-bridge inverter," 2020 IEEE Energy Conversion Congress and Exposition (ECCE), Detroit, MI, USA, 2020, pp. 2606-2611, doi:10.1109/ECCE44975.2020.9236112

(Li 2021) K. Li, A. Bouscayrol, C. Cui, Y. Cheng, “A Hybrid Modular Cascade Machines System for Electric Vehicles using Induction Machine and Permanent Magnet Synchronous Machine", IEEE transactions on Vehicular Technology, Vol.70, no.1, pp 273-281, January 2021

(Li 2025) K. Li, W. Lhomme, A. Bouscayrol, B. Lemaire-Semail, K. Stockman, C. Brocart,"Energy savings of a four-drive electric bus with two cascaded smart integrated drives on each axle," IEEE Transactions on Transportation Electrification, vol. 11, no. 1, pp. 4145-4156, February 2025

(Mayet 2014) C. Mayet, L. Horrein, A. Bouscayrol, P. Delarue, J. N. Verhille, E. Chatot, B. Lemaire-Semail, “Comparison of different models and simulation approaches for the energetic study of a subway", IEEE transactions on Vehicular Technology, Vol. 63, no. 2, February 2014, pp. 556-565, DOI: 10.1109/TVT.2013.2280727

(Medvedko 1998) A. S. Medvedko, “Review of the power supplies for electromagnet of the storage rings and synchrotrons,” in *Proc. 17th Int. Conf. High-Energy Accelerators*, Dubna, Russian Federation, Sep. 7–12, 1998, pp. 294–299, 1998. Available: https://inspirehep.net/files/f29b1c5fbf25162f2da82b7ff141e6ed.

(Mentink 2023) M. Mentink, K.-i. Sasaki, B. Curé, N. Deelen, A. Dudarev, M. Abe, M. Iio, Y. Makida, T. Okamura, T. Ogitsu, N. Sumi, A. Yamamoto, M. Yoshida, and H. Iinuma, “Superconducting detector magnets for high energy physics,” J. Instrum., vol. 18, no. 06, Art. T06013, Jun. 2023, doi: 10.1088/1748-0221/18/06/T06013.

(Ndiaye 2024) A. Ndiaye, R. German, A. Bouscayrol, M. Gaetani-Liseo, P. Venet, E. Castex, "Impact of the User Charging Practice on the Battery Aging in an Electric Vehicle," IEEE Transactions on Vehicular Technology, vol. 73, no. 4, pp. pp. 4578-4588, April 2024, DOI; 10.1109/TVT.2024.3356116

(Nguyen 2019) B.H. Nguyen, R. German, J. Trovao, A. Bouscayrol, “Real-time energy management of battery/supercapacitor electric vehicles Based on an adaptation of Pontryagin’s minimum principle”, IEEE transactions on Vehicular Technology, vol. 68, no. 1, January 2019, pp. 203-212, P DOI: 10.1109/TVT.2018.2881057

(Ortega 2020) C. Ortega Perez, “Comparison of EMR-based control and RST-based control for fast pulsed power converters,” Master’s thesis, Univ. Lille, L2EP, Lille, France, 2020.

(O'Beriel 2025) R. O'Beriel, P. Delarue, C. Mayet, A. Bouscayrol,C. Brocart, "Analysis of the timetable impact on energy consumption of a subway line" IEEE transactions on Vehicular Technology, Vol. 74, No. 2, pp. 2549-2558, February 2025

(Page 2019) S. T. Page, C. Ghabrous Larrea, Q. King, B. Todd, S. Uznanski, and D. J. Zielinski, "FGC3.2: A New Generation of Embedded Controls Computer for Power Converters at CERN," in *Proc. 17th Int. Conf. on Accelerator and Large Experimental Physics Control Systems (ICALEPCS'19)*, New York, NY, USA, Oct. 2019, pp. 468–472, doi:10.18429/JACoW-ICALEPCS2019-MOPHA106.

(Panaino 2025) C. M. V. Panaino, S. Piccinini, M. G. Andreassi, G. Bandini, A. Borghini, M. Borgia, A. Di Naro, L. U. Labate, E. Maggiulli, M. G. A. Portaluri, L. A. Gizzi, and et al., "Very High-Energy Electron Therapy Toward Clinical Implementation: A Review Study," *Cancers*, vol. 17, no. 2, Art. 181, 2025, doi:10.3390/cancers17020181.

(Peng 2019) T. Peng, H. Tao, C. Yang, Z. Chen, C. Yang, W. Gui, H. R. Karimi, "A Uniform Modeling Method Based on Open-Circuit Faults Analysis for NPC- Three-Level Converter," in IEEE Transactions on Circuits and Systems II: Express Briefs, vol. 66, no. 3, pp. 457-461, March 2019, doi: 10.1109/TCSII.2018.2856862.

(Péron 2009) R. Péron, V. Guennegues, J.-L. Pouliquen, B. Gollentz, F. Bordry, and J.-P. Burnet, "Performances analysis of main components used in 60 MW pulsed supply for particle accelerator," CERN-ATS-2010-023, presented at the 13th European Conference on Power Electronics and Applications (EPE'09), Barcelona, Spain, Sep. 8–10, 2009, 11 pp. Available: https://cds.cern.ch/record/1254296.

(Ramsey 2022) D. Ramsey, A. Bouscayrol, L. Boulon, "Flexible Simulation of an Electric Vehicle to Estimate the Impact of Thermal Comfort on the Energy Consumption", IEEE transactions on Transportation Electrification, Vol. 8, no.2, pp. 2288-2298, June 2022

(Schulte 2020) D. Schulte, J.-P. Delahaye, M. Diemoz, K. R. Long, B. Mansoulié, N. Pastrone, L. Rivkin, A. M. Skrinsky, and A. Wulzer, "Muon Collider. A Path to the Future?," in *Proc. European Physical Society Conference on High Energy Physics (EPS-HEP2019)*, Ghent, Belgium, Jul. 10–17 2019, vol. 364, Art. no. 004, 2020, doi: 10.22323/1.364.0004.

(Schulte 2022) D. Schulte, "The Muon Collider," in *Proc. 13th Int. Particle Accelerator Conf. (IPAC'22)*, Bangkok, Thailand, Jun. 12–17, 2022, pp. 821–826, doi:10.18429/JACoW-IPAC2022-TUIZSP2.

(Scirè 2025) D. Scirè and G. Vitale, “Advanced control techniques for power converter and drives,” *Electronics*, vol. 14, no. 18, Art. no. 3710, Sep. 19, 2025, doi:10.3390/electronics14183710.

(Silari 2011) Silari M. Applications of particle accelerators in medicine. Radiat Prot Dosimetry. 2011 Jul;146(4):440-50. doi: 10.1093/rpd/ncr243. Epub 2011 Jun 14. PMID: 21676897.

(Spierer 2022) A. Spierer, P. Baudrenghien, J. Egli, G. Hagmann, P. Kuzmanovic, I. Stachon, M. Suminski, T. Wlostowski, “The CERN SPS Low Level RF: The Beam-Control”, in *Proc. 13th Int. Particle Accelerator Conf. (IPAC’22)*, Bangkok, Thailand, Jun. 12–17, 2022, pp.895-898, doi: 10.18429/JACoW-IPAC2022-TUPOST021.

(Tournez 2025) F. Tournez, W. Lhomme, A. Bouscayrol, R. German, B. Lemaire-Semail, A. Lièvre, M. Sanchez-Torrez, “Power Hardware and Driver-in-the-Loop for Battery Testing applied to Electrified Vehicles”, EPE’25, Paris (France), March 2025.

(Videt 2008) A. Videt, “Variateur de vitesse à impact électromagnétique réduit : onduleurs multiniveaux et nouvelles stratégies de modulation, “ Ph.D. dissertation, École Centrale de Lille, Lille, France, Dec. 2008.

(Wangler 2008) T. P. Wangler, *RF Linear Accelerators*, 2nd ed. Weinheim, Germany: Wiley-VCH, 2008. doi: 10.1002/9783527623426.

(Wiedemann 2015) H. Wiedemann, *Particle Accelerator Physics*, 4th ed. Cham, Switzerland: Springer Cham, 2015. doi: 10.1007/978-3-319-18317-6.

(Yu 2014) Yu. S. Pavlov, Proc. 24th Int. Conf. “Radiation Solid State Physics,” Ed. by G. G. Bondarenko (NII PMT, Moscow, 2014), p. 22.

(Zielinski 2025) D. Zielinski and R. Murillo-Garcia, “An overview of the FGC4 – CERN’s new power converter controller,” in *Proc. 20th Int. Conf. Accel. Large Exp. Phys. Control Syst. (ICALEPCS ’25)*, Chicago, IL, USA, Sep. 2025, pp. 1107–1111, doi: 10.18429/JACoW-ICALEPCS2025-WEPD035.

(Zimmermann 2025) F. Zimmermann and M. Benedikt, “Highlights from Future Circular Collider Feasibility Study and Path to Construction,” in *Proc. Int. Particle Accelerator Conf. (IPAC’25)*, Taipei, Taiwan, Jun. 1–6, 2025, paper FRZD3, 2025, doi: 10.18429/JACoW-IPAC2025-FRZD3.